

Fibre Distribution Characterization and Its Impact on Mechanical Properties of Ultra- High Performance Fibre Reinforced Concrete

Thesis submitted in accordance with the requirement of the

University of Liverpool

School of Engineering

for the degree of Doctor in Philosophy

By

Lufan Li

Supervisors: Dr. Jun Xia, Dr. Chee S. Chin, Dr. Stephen W. Jones

January 2019

This copy of the thesis has been supplied on condition that anyone who consults it is understood to recognize that its copyright rests with its author and that no quotation from the thesis and no information derived from it may be published without proper acknowledgment.

ABSTRACT

Ultra-high performance fibre reinforced concrete (UHPFRC) is the most innovative cement based engineering material. It is also a big leap for the performance of this engineering material. The mechanical properties of UHPFRC not only depend on the properties of concrete matrix and fibres, but also depend on the interaction between these two elements. Moreover, this reaction is highly influenced by the fibre volume content distribution and fibre orientation distribution.

Previous researchers had developed different methods to test the fibre distribution. However, apart from a general fibre efficiency reduction factor, there was no quantified relationship between the different fibre distribution and its corresponding mechanical performance. This research focuses on testing the fibre distribution and investigating their influences on the mechanical properties of UHPFRC.

This research adopted the C-shape ferromagnetic probe inductive test. The effective depth of the magnetic probe was determined, and then this method was applied for testing the specimens with different thicknesses to obtain fibre volume content and fibre orientation angle. Image analysis was carried out on a number of specimens to prove the accuracy of the magnetic probe inductive test. Mechanical tests including compressive tests, uniaxial tensile tests and bending tests were carried out after the fibre distribution tests.

The level of material performance enhancement is dependent on the fibre volume content and orientation angle. For tensile performance, the low dosage of fibres has little enhancement on the peak tensile/bending strength. Linear relationships can be found between the peak uniaxial tensile strength and fibre distribution with higher fibre dosages. This relationship was then further proved using the OpenSees programme.

From the industrial point of view, over-dosing with fibres increases the construction cost. Furthermore, it may cause non-uniform fibre distribution and early concrete cracking. In order to improve the tensile behaviour of UHPFRC, adjusting the fibre orientation angle rather than simply increasing fibre volume content can be considered.

DEDICATION

I dedicate this work to my beloved

Father & Mother,

who

have always been a source of inspiration and power

to undertake this study

and face the eventualities in my life

with confidence and enthusiasm.

ACKNOWLEDGEMENTS

I would like to express my deepest gratitude to my supervisors

Dr. Jun Xia, Dr. Chee S. Chin and Dr. Stephen W. Jones

for their constant guidance and support in the completion of this research.

A sincere vote of thanks goes to technicians *Mr. Suming Luo, Mr. Xiaoting Wang, Mr. Peizhong Chen, Mr. Yunquan Chen, and Mrs. Qiaolian Li* for their instructions and help in my lab work.

As the first alumni from the civil engineering department in XJTU, I greatly appreciate all staff members for their irreplaceable effort, and I feel so honoured to witness the development of our department.

I am indebted to *Prof. Martine Browne*, for his wisdom and passion for research that inspire me all the time.

I would also like to acknowledge my colleague *Dr. Xinyi Wang* and *Ms. Bhooma Nepal* for their critical and illuminating advice, which have influenced my research and life.

Last I owe my dearest friends, for their loving considerations and confidence in me for all these years.

TABLE OF CONTENTS

ABSTRACT	i
DEDICATION.....	iii
ACKNOWLEDGEMENTS	v
TABLE OF CONTENTS	vii
LIST OF FIGURES	xi
LIST OF TABLES	xix
TABLE OF ABBREVIATIONS	xxi
TABLE OF NOTATION	xxi
CHAPTER 1 INTRODUCTION.....	1
1.1 Background.....	1
1.1.1 From conventional concrete to UHPC	1
1.1.2 Addition of fibres.....	4
1.1.3 Advantages and applications of UHPFRC	7
1.2 Research Gap.....	8
1.3 Aims and Objectives	9
1.4 Thesis Structure.....	10
CHAPTER 2 LITERATURE REVIEW	11
2.1 General Mechanical Properties of UHPFRC	11
2.1.1 Behaviour in compression	11
2.1.2 Behaviour in tension	12
2.1.3 Different tensile constitutive laws	15
2.1.4 Deriving uniaxial tensile strength from other tests.....	17
2.2 How to Describe Fibre Orientation	19
2.2.1 Fibre orientation tensor	19
2.2.2 Fibre orientation factor.....	22

2.2.3	Fibre distribution coefficient.....	23
2.3	Factors Affecting Fibre Distributions	23
2.3.1	Aspect ratio and fibre volume fraction	23
2.3.2	Extensional flow and wall effect	25
2.3.3	External vibration	27
2.3.4	Mixing sequence	28
2.4	Methods in Testing Fibre Distribution	30
2.4.1	Manual visual counting method.....	30
2.4.2	Image analysis method	31
2.4.3	X-ray CT scanning method	32
2.4.4	AC-IS method	36
2.4.5	Magnetic core inductive test method.....	38
2.4.6	C-shape ferromagnetic probe inductive test method	39
2.4.7	Summary.....	41
CHAPTER 3	SPECIMEN PREPARATION	42
3.1	Self-developed UHPFRC Mix	42
3.2	UHPFRC Mix with Pre-mix Powders.....	44
3.3	Concrete Mixing	47
3.4	Concrete Casting	50
3.5	Workability Test	51
3.6	Concrete Curing	52
CHAPTER 4	FIBRE DISTRIBUTION TEST METHOD.....	53
4.1	Cylindrical Permanent Magnet Test Method.....	53
4.1.1	Theoretical derivation	53
4.1.2	Test setup	55
4.2	C-shape Magnetic Probe Inductive Test Method.....	58
4.2.1	Probe specification.....	58
4.2.2	Effective depth test	60

4.2.3	Inductive Test on UHPFRC beams.....	62
4.2.4	Inductive Test on UHPFRC slabs.....	64
4.3	Image Analysis Using Matlab.....	66
CHAPTER 5 MECHANICAL TESTS METHOD		68
5.1	Compressive Test.....	68
5.2	Uniaxial Tensile Test	69
5.3	Four-Point Bending Test on Thick Beams	71
5.4	Three-Point Bending Test on Thin Beams.....	73
CHAPTER 6 FIBRE DISTRIBUTION TEST RESULTS		75
6.1	Cylindrical Permanent Magnet Test Results.....	75
6.2	Inductive Test Results for Determining Effective Depth	76
6.3	Image Analysis Results	79
6.3.1	Layer analysis.....	79
6.3.2	Fibre segregation effect due to external vibration	83
6.4	Inductive Test Results for UHPFRC Slabs	84
6.4.1	Fibre volume content distribution results.....	84
6.4.2	Fibre orientation distribution results	88
6.4.3	Summary	93
CHAPTER 7 MECHANICAL TEST RESULTS		94
7.1	Compressive Test Results	94
7.2	Uniaxial Tensile Test Results.....	97
7.3	Four-Point Bending Test Results.....	101
7.3.1	Four-point bending test results for 75×75×450 mm beams	101
7.3.2	Four-point bending test results for 100×100×400 mm beams.....	103
7.3.3	Four-point bending test summary	105
7.4	Three-point Bending Test Results.....	106
CHAPTER 8 ANALYSES AND DISCUSSIONS		110
8.1	Theoretical Derivation on Working Mechanism of UHPFRC after Crack	110

8.1.1	Fibre activation stage.....	110
8.1.2	Fibre pull-out stage	112
8.2	Further Analysis on Three-point Bending Test.....	113
8.2.1	Peak uniaxial tensile strength of UHPC	113
8.2.2	Relationship between fibre distribution and peak flexural strength of UHPFRC.....	113
8.3	Multiscale FEM using Digimat and ANSYS	120
8.3.1	Fibre geometry generation using Digimat	120
8.3.2	Ansys Workbench analysis and results	122
8.4	OpenSees FEM Simulation Method.....	125
CHAPTER 9 CONCLUSIONS AND FUTURE WORKS		129
9.1	Conclusions	129
9.2	Future Works.....	130
REFERENCES		133
APPENDICES		a
Appendix 1	Total Specimen List	a
Appendix 2	Load-deflection curve for 50×200×H beams.....	c

LIST OF FIGURES

Figure 1-1	Densified particle packing theory [8].	2
Figure 1-2	Comparison of mix composition of conventional concrete (a) and UHPC (b) by weight.	3
Figure 1-3	Influence of fibre diameter on the matrix porosity [16].	5
Figure 1-4	Fibres used for conventional concrete (a), stainless (b) and brass coating (c) steel fibres for UHPFRC.	6
Figure 1-5	The first UHPC bridge - Sherbrooke Footbridge in Canada [7].	7
Figure 1-6	LEGO style texture UHPC cladding in France [14].	8
Figure 2-1	Stress-strain relationship for uniaxial compressive test of UHPC [7].	11
Figure 2-2	Stress-strain relationship for uniaxial compressive test of UHPC and UHPFRC [28].	12
Figure 2-3	UHPC matrix softening, fibre activation, and superposition of two curves [7].	13
Figure 2-4	Tensile behaviour of UHPFRC [32].	14
Figure 2-5	Typical stress-crack width behaviour of UHPC in a tensile test [7].	15
Figure 2-6	Tensile constitutive law of strain softening fibre-reinforced concrete [26].	16
Figure 2-7	Tensile constitutive law of low strain hardening fibre-reinforced concrete [26].	16
Figure 2-8	Tensile constitutive law of high strain hardening fibre-reinforced concrete [26].	17
Figure 2-9	Relationship between component thickness and flexural tensile strength [38].	18
Figure 2-10	Orientation angles of a single fibre.	19
Figure 2-11	Top, front, side, and overall view of 1D aligned fibre orientation diagram.	21
Figure 2-12	Top, front, side, and overall view of 2D random fibre orientation diagram.	22
Figure 2-13	Top, front, side, and overall view of 3D random fibre orientation diagram.	22
Figure 2-14	Ways to prevent fibre balling [48].	25
Figure 2-15	Rotation of fibres when moving from the centre to the edges [53].	26
Figure 2-16	Areas affected by wall effect [59].	26

Figure 2-17	Effect of different vibration directions on fibre alignment [61].	27
Figure 2-18	Standard (left) and adjusted (right) mixing sequences.	29
Figure 2-19	Relationship between fibre distribution coefficient and tensile strain capacity [67].	29
Figure 2-20	A 50×50 mm cross section area of 1% vol. UHPFRC sample.	30
Figure 2-21	Image analysis procedures [32].	31
Figure 2-22	Cross section of fibres cut by a plane [73].	31
Figure 2-23	3D view of fibre and definition of an ellipse [72].	32
Figure 2-24	Working procedures of X-ray CT scanning method [76].	33
Figure 2-25	An original CT image of steel fibre reinforced sample [69].	34
Figure 2-26	Procedure of obtaining second-order orientation tensor from CT image (take 2D projection as an example) [60].	35
Figure 2-27	Experimental setup of AC-IS test [52].	36
Figure 2-28	Example of Nyquist curves for plain and SFRC [52].	37
Figure 2-29	Electromagnetic coil used in the magnetic core inductive test.	38
Figure 2-30	Magnetic probe and experiment setup in Nunes' research [88].	39
Figure 2-31	Variation of μ_{r,θ_i} , $\mu_{r,(90^\circ-\theta_i)}$, and $\mu_{r,\text{mean}}$ with the angle θ_i . [88].	39
Figure 2-32	Variation of orientation indicator with θ_i for different fibre contents [88].	40
Figure 3-1	All raw materials used in self-developed UHPFRC.	42
Figure 3-2	Brass coating steel fibres used for UHPFRC.	43
Figure 3-3	Pre-mix powder provided by company.	45
Figure 3-4	All raw materials used in pre-mix UHPFRC.	45
Figure 3-5	Concrete mixer (a) (b) and funnel (c) used in concrete casting.	47
Figure 3-6	Concrete balls during mixing.	48
Figure 3-7	Concrete moulds used in the research.	49
Figure 3-8	Cast slabs (a) and beams (b).	50
Figure 3-9	Slump test for fresh UHPFRC.	51
Figure 3-10	Fresh concrete covered with plastic film.	52
Figure 3-11	Water (a) and steam (b) curing tank.	52
Figure 4-1	Initial cylindrical permanent magnet test setup.	55
Figure 4-2	Cylindrical permanent magnet and FSR used in the experiment.	56

Figure 4-3	UHPFRC slabs used in cylindrical permanent magnet test.....	56
Figure 4-4	Final cylindrical permanent magnet test setup.	57
Figure 4-5	Appearance and detailed dimensions of ferrite core.....	58
Figure 4-6	Magnetic probe (a) and copper wire (b).	58
Figure 4-7	C-shape magnetic probe inductive test setup.	59
Figure 4-8	Agilent HP4284A (a) and Tonghui TH2830 (b) LCR meter.	59
Figure 4-9	Acrylic slabs used in the experiment (a) and experiment set up (b). ..	61
Figure 4-10	Horizontal testing on 75×75×450 mm UHPFRC beams (unit: mm).....	62
Figure 4-11	Horizontal (a) and vertical (b) testing method on UHPFRC beams (unit: mm).....	63
Figure 4-12	500×500×H UHPFRC slab used for inductive test.....	64
Figure 4-13	Testing area divisions of UHPFRC slab (unit: mm).	65
Figure 4-14	Horizontal (a) and vertical (b) testing directions.	65
Figure 4-15	Cutting positions on UHPFRC beams.	66
Figure 4-16	Image processing procedures.	67
Figure 5-1	Compressive test setup.	68
Figure 5-2	Uniaxial tensile test setup.....	70
Figure 5-3	DNS-300 UTM (a) and connection between steel mould and UTM (b).	70
Figure 5-4	Four-point bending test setup on 100×100×400 mm beams.	71
Figure 5-5	Schematic graph of the bending test on self-developed UHPFRC beams (unit: mm).....	72
Figure 5-6	Schematic graph of the bending test on pre-mix UHPFRC beams (unit: mm).....	72
Figure 5-7	Concrete slabs cut by water blade.	73
Figure 5-8	Cutting division of concrete slab.....	73
Figure 5-9	Three-point bending test for UHPFRC beam.	74
Figure 5-10	Three-point bending test setup on a 200×50×20 mm UHPFRC beam.	74
Figure 6-1	Contour graph of fibre volume content of 0.5%, 1%, and 2% vol. UHPFRC slabs (unit: mV).	75
Figure 6-2	Average attenuation factor at different depth for each group.	78
Figure 6-3	Comparison between experimental and theoretical attenuation factor at different depth.	79

Figure 6-4	Original (a) and enlarged (b) images taken from a 5% vol. UHPFRC cross section.	80
Figure 6-5	Number of fibres in different regions in layer analysis (unit: mm).	80
Figure 6-6	Relationship between relative magnetic permeability and number of fibres of 2% vol. UHPFRC within different regions.	81
Figure 6-7	Areas of number of fibres counted for 75×75 mm and 100×100 mm cross sections (unit: mm).	81
Figure 6-8	Relationship between relative magnetic permeability and number of fibres in 75×20 mm region.	82
Figure 6-9	Number of fibres counted in the top and bottom 20 mm region (unit: mm).	83
Figure 6-10	Three different groups of data calculated in the research (unit: mm). .	84
Figure 6-11	Relationship between fibre volume content and relative magnetic permeability.	86
Figure 6-12	Fibre volume content distribution of all slabs.	88
Figure 6-13	Relationship between fibre orientation angle and fibre orientation indicator.	89
Figure 6-14	Relationship between fibre orientation angle and fibre orientation indicator at different fibre volume content.	90
Figure 6-15	Fibre orientation angle distribution of all slabs.	91
Figure 6-16	Distribution of fibre orientation angle.	92
Figure 6-17	Probability density distribution of fibre orientation angle.	93
Figure 7-1	UHPC and 2% vol. UHPFRC specimens after compressive test.	94
Figure 7-2	Compressive strength of different groups of 100 mm cube specimens. .	95
Figure 7-3	Relationship between fibre content and compressive strength for Pre-mix 100 mm cubes.	96
Figure 7-4	2% vol. UHPFRC dog bone specimens after uniaxial tensile test.	97
Figure 7-5	Stress-strain curves and load-displacement curves for all specimens. ...	99
Figure 7-6	75×75×450 mm 2% and 3% vol. beams after four-point bending test. .	101
Figure 7-7	Load-deflection curves for 2% and 3% vol. UHPFRC beams.	102
Figure 7-8	Load-deflection curves for 1%, 2%, and 5% vol. UHPFRC beams.	104
Figure 7-9	50×200×20 mm beams after three-point bending test.	106
Figure 7-10	Relationship between beam thickness and average peak flexural strength.	107

Figure 7-11	Load-deflection curves for 15 and 20 mm thick UHPC and UHPFRC beams.	109
Figure 8-1	Effective embedment length of fibres inside concrete matrix in uniaxial tensile test in fibre activation stage.	111
Figure 8-2	Effective embedment length of fibres inside concrete matrix in uniaxial tensile test in fibre pull-out stage.....	112
Figure 8-3	Load-deflection curves for 1% vol. 200×50×15 mm UHPFRC beams..	116
Figure 8-4	Relationship between $V_f \cdot \cos(\varphi)$ and peak flexural strength for 1% vol. UHPFRC beams.....	117
Figure 8-5	Load-deflection curves for 2% vol. 200×50×20 mm UHPFRC beams..	118
Figure 8-6	Relationship between $V_f \cdot \cos(\varphi)$ and peak flexural strength for 2% vol. UHPFRC beams.....	118
Figure 8-7	Relationship between $V_f \cdot \cos(\varphi)$ and peak flexural strength for 2.5% vol. UHPFRC beams.....	119
Figure 8-8	Define phase type of concrete and fibre in Digimat.....	120
Figure 8-9	Define fibre volume content and fibre orientation distribution.....	121
Figure 8-10	Define RVE options.....	121
Figure 8-11	25 mm 1% vol. UHPFRC cube with 3D random distribution.	122
Figure 8-12	Mesh condition of concrete and fibre.	122
Figure 8-13	General and detailed UHPFRC mesh view.	123
Figure 8-14	Deformation along loading axis (Y-axis) (unit: mm).....	123
Figure 8-15	Equivalent stress of concrete matrix under different displacement (unit: MPa).....	124
Figure 8-16	Input stress-strain diagram in OpenSees programme.	125
Figure 8-17	Correlation between experimental and simulated peak flexural strength (unit: MPa).	127
Figure 8-18	Comparison of stress-deflection curve of 2%-20-s1 experimental and OpenSees simulated results.....	128

LIST OF TABLES

Table 3-1	Control mix proportion for self-developed UHPFRC.....	43
Table 3-2	Mixing procedure and time for self-developed UHPFRC.....	44
Table 3-3	Control mix proportion for pre-mix UHPFRC (provided by company).	46
Table 3-4	Mixing procedure and time for pre-mix UHPFRC.	46
Table 3-5	Specimen list and casting purpose for different types of specimens.	49
Table 4-1	Inductance data of basic objects (unit: mH).	60
Table 4-2	UHPFRC beams used for effective depth test.....	60
Table 4-3	Acrylic slab combination for effective depth test (unit: mm).	61
Table 6-1	Signal voltage obtained from experiment.	76
Table 6-2	Average relative magnetic permeabilities obtained for each group.	77
Table 6-3	Average attenuation factors calculated for each group.....	78
Table 6-4	Differences between vibrated and non-vibrated 2% and 3% vol. UHPFRC beams.	83
Table 6-5	Mean, STD, and COF of relative magnetic permeabilities of all slabs.	85
Table 6-6	Mean and STD of fibre volume content of all slabs.	87
Table 6-7	Mean, STD, and COF of fibre orientation angles of all slabs.	92
Table 7-1	Compressive strength of different groups of 100 mm cube specimens. .	95
Table 7-2	Young's modulus for all the specimens (unit: GPa).....	97
Table 7-3	Crack and peak uniaxial tensile strength for all the specimens (unit: MPa).....	100
Table 7-4	Average peak flexural strength, corresponding mid-span deflection and RMP for SD group.	103
Table 7-5	Average peak flexural strength, corresponding mid-span deflection, and RMP for Pre-mix group.....	104
Table 7-6	First crack flexural strength and peak flexural strength for Pre-mix specimens (unit: MPa).....	107
Table 8-1	Experimental peak flexural strength and calculated peak uniaxial tensile strength of UHPC (unit: MPa).....	113
Table 8-2	First crack, peak flexural strength and fibre distribution of Pre-mix specimens.....	114

Table 8-3 Linear material properties used in multiscale modelling.123

TABLE OF ABBREVIATIONS

AF	Attenuation Factor
AR	Aspect Ratio
BISO	Bilinear Isotropic Hardening
CMOD	Crack Mouth Opening Displacement
COV	Coefficient of Variation
FEM	Finite Element Method
FRC	Fibre Reinforced Concrete
FSR	Force Sensing Resistor
NFRC	Normal Fibre Reinforced Concrete
ODF	Orientation Distribution Function
OpenSees	Open System for Earthquake Engineering Simulation
OT	Orientation Tensor
PP	Polypropylene
PVA	Polyvinyl Alcohol
RMP	Relative Magnetic Permeability
RVE	Representative Volume Element
SD Mix	Self-developed Mix
SFRC	Steel Fibre Reinforced Concrete
STD	Standard Deviation
UHPC	Ultra-High Performance Concrete
UHPFRC	Ultra-High Performance Fibre Reinforced Concrete
UTM	Universal Testing Machine
X-ray CT	X-ray Computed Tomography

TABLE OF NOTATION

α	Fibre orientation factor
α_f	Factor for difference fibre types
β	Fibre orientation coefficient
ε	Strain in stress-strain relationship
ε_{el}	Elastic strain limit in uniaxial tensile test
ε_{lim}	Ultimate strain in uniaxial tensile test
η_y	Fibre orientation along gravity axis
θ	Out-of-plane angle in orientation coordinate
θ_i	Fibre orientation angle used in Nune's research
λ	Fibre orientation angle coefficient
μ_0	Relative magnetic permeability when placing the probe directly on the specimen
μ_{ave}	Average relative magnetic permeability
μ_{cal}	Relative magnetic permeability after correction
μ_f	Relative magnetic permeability of steel fibre
μ_t	Relative magnetic permeability at thickness t
μ_{test}	Relative magnetic permeability tested (without correction)
μ_{θ_i}	Relevant magnetic permeability at angle θ_i
$\mu_{(90^\circ-\theta_i)}$	Relevant magnetic permeability at angle $(90^\circ-\theta_i)$
μ_{mean}	Average relative magnetic permeability
μ_x	Relative magnetic permeability measured in horizontal direction
μ_y	Relative magnetic permeability measured in vertical direction
μ_v	Magnetic permeability of vacuum
ρ_Δ	Orientation indicator
σ	Mean in probability density function of fibre orientation angle
σ_{cf}	Fibre efficiency factor
τ	Static frictional strength
τ_0	Sliding frictional strength

φ	In-plane angle in orientation coordinate, also fibre orientation angle
ω	Crack width
ω_0	Crack with limit before fibre pull out
ΔL	Variation of inductance
ΔL_T	Sum of variance of inductance
a	Major axis of the ellipse cross section in image analysis
a_{ij}	Element in orientation tensor
b	Minor axis of the ellipse cross section in image analysis
c	Fibre efficiency coefficient
d_1, d_2	Diameters of cylinder specimen in compressive test
d	Average diameter of cylinder specimen in compressive test
d_f	Fibre diameter
f_c	Compressive strength
$f_{c,cu}$	Compressive strength of cubical specimen
$f_{c,cy}$	Compressive strength of cylindrical specimen
$f_{ct,fl,el}$	Extreme fibre stress upon formation of flexural crack or elastic limit
f_f	Flexural strength
f_{sl}	Sliding frictional force
$f_{sl,eff}$	Effective sliding frictional force
$f_{sl,n}$	Total effective sliding frictional force
f_{st}	Static frictional force
$f_{st,eff}$	Effective static frictional force
$f_{st,n}$	Total effective static frictional force
f_t	Uniaxial tensile strength
f_{t0}	First crack tensile strength of concrete matrix
l_c	Characteristic length
l_f	Fibre length
n	Number of images in fibre distribution coefficient calculation
n_f	Number of fibres crossing a unit surface

t	Distance between magnetic probe and specimen in effective depth testing
$x_{average}$	Average number of fibres in all images in fibre distribution coefficient calculation
x_i	Total number of fibres in the i_{th} image in fibre distribution coefficient calculation
A	Cross section area of specimen in compressive and uniaxial tensile test
A_f	Cross section area of steel fibre
A_t	Cross section area of specimen in uniaxial tensile test
B	Width of the beam cross section
B_m	Magnetic flux density
F_c	Load in compressive test
F_f	Load in flexural test
F_m	Magnetic force
F_n	Weighting function in orientation tensor
F_t	Load in uniaxial tensile test
H	Height of the beam cross section
K	fibre efficiency factor
K_m	Adjusting factor for cylindrical permanent magnet test
L	Span in three-point bending test
L_0	Inductance measured directly on the specimen
L_{air}	Inductance measured in air
L_s	Distance between support and the nearby loading point
$L_{\theta i}$	Inductance at angle θi
$L_{(90^\circ-\theta i)}$	Inductance at angle $(90^\circ-\theta i)$
M	External bending moment
S	Reaction area between the magnetic field and steel fibres
V_f	Designed fibre volume content
V_s	Volume of testing area in cylindrical permanent magnet test
W	Elastic section modulus

CHAPTER 1 INTRODUCTION

In this chapter, the history and development of ultra-high performance fibre reinforced concrete is introduced. The application of UHPFRC in the modern construction industry is also included, highlighting the advantages and disadvantages in using this material. UHPFRC is not thoroughly investigated if the influence of fibre distribution is not studied. Based on previous literature, the aim of finding the relationship between fibre distribution and mechanical properties will be presented.

1.1 Background

1.1.1 From conventional concrete to UHPC

When talking about the history of structures in the construction field, we can start from the Stonehenge 5,000 years ago [1] when man placed two stones vertically and one flat stone on top, to the high-rise steel and reinforced concrete buildings we can see now in daily life. From around 1824, when Joseph Aspdin [2] developed Portland cement, concrete has been the most significant construction material and its consumption is still growing all over the world. Throughout history, many materials had been used for construction purposes, for example, stone, masonry, and timber. Each material has its own spotlight, but when considering all the factors such as appearance, strength, durability, construction efficiency, concrete is considered to be more economical and practical.

Conventional concrete contains cement, coarse aggregates, fine aggregates, and water. Common compressive strengths of concrete used in industry range from 30 MPa to 60 MPa. According to the design code for the ‘Design of Concrete Structures’ [3], the strength grade for a pure concrete structure should be higher than C15, while a minimum C40 strength grade is required for a pre-stressed concrete structure. With the development of the construction industry, people were looking for a cementitious composite material with far higher strength, durability, and resistance to external environments than

traditional construction materials [4]. This superior performance concrete is called ‘Ultra-High Performance Concrete (UHPC)’. For structural elements, according to ACI Committee 239 [5], UHPC is a “concrete that has a minimum specified compressive strength of 150 MPa with specified durability, tensile ductility, and toughness requirements; fibres are generally included to achieve the specified requirements.” For non-structural applications like decoration, the compressive strength can be lower considering the workability and finishability.

Conventional concrete always requires vibration after mixing to release the air trapped in the concrete matrix since large air voids will reduce the strength of concrete. Around the 1980s, researchers found that by adding amounts of silica fume, the concrete strength can increase to 80-90 MPa. The design theory behind this is known as ‘Densified Particle Packing Theory’. The packing density is defined as the volume percentage of solids for each volume unit [6]. In UHPC, no coarse aggregate is used at all. Apart from fine sands, ultrafine particles (grain size $125\mu\text{m}$) like cement, quartz powder, and silica fume are used. As shown in Figure 1-1, during mixing, the voids between sand particles are filled by cement, then the gaps between cement are filled with smaller particles of quartz powder or fly ash. Even smaller voids are finally filled with silica fume. Researchers found that the packing density rose from 65% to more than 83% by adjusting the volume proportion of individual grains [7]. Briefly speaking, UHPC has a much denser microstructure where all granular constituents are tightly packed.

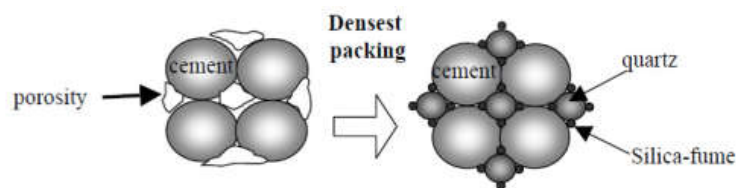


Figure 1-1 Densified particle packing theory [8].

Another reason leading to high strength is the very low water/cement ratio, which is only around 0.2 (compared to 0.45 for conventional concrete). Figure 1-2 shows a comparison of mix proportions of a designed C40 conventional concrete and C120 UHPC (for decoration purpose). A maximum limiting water/cement ratio of 0.24 is suggested to control the formation of capillary tunnels/pores [9]. This fact broadened researchers’

views because in the past it was considered that the water/binder ratio was the critical factor in determining the concrete strength.

Researchers always had difficulty finding a material with both high compressive strength and good workability. Only after the breakthrough of superplasticizers, was it possible to produce concrete with the required strength and workability [7]. With the help of superplasticizers, the workability is further improved, thus, air voids will be expelled during casting.

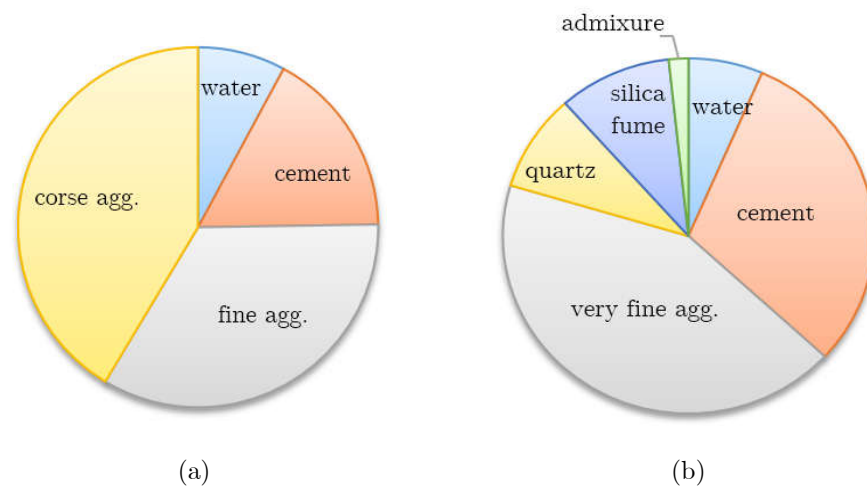


Figure 1-2 Comparison of mix composition of conventional concrete (a) and UHPC (b) by weight.

The curing of UHPC starts during mixing. Due to the low water/cement ratio, the concrete surface dries very quickly and can lead to an ‘elephant skin’ state. The ‘elephant skin’ will stop the de-aerating of concrete and reduce the workability of concrete. To solve this problem, fresh concrete members are always covered with a plastic sheeting immediately after casting. It is even better to spray an effective curing agent or water mist on the surface to form a film [7]. For lab research, unlike conventional concrete, which is usually cured in water for 28 days at room temperature treatment (at around 20°C), UHPC requires heat curing treatment at around 80-90°C because an elevated temperature can benefit the reaction between the silica fume and the calcium hydroxide in the cement and there is minimal hydration reaction after curing [10]. Therefore, the microstructure becomes denser which increases the compressive and tensile strengths. Furthermore, there is minimal shrinkage after curing, and this maintains the dimensions

of precast elements. Fresh concrete members are usually cured under plastic sheeting for 24 hrs and then hot curing for 48 hrs. There is no noticeable strength enhancement with a longer curing duration. After hot curing, the members should be cooled slowly and protected against drying out quickly to prevent micro-cracking.

1.1.2 Addition of fibres

Generally speaking, concrete is considered to be a brittle material. Historically, about 3500 years ago, brittle materials like sun-baked clay bricks were reinforced with horsehair, straw, and other vegetable fibres. This is the earliest form of fibre-reinforced material [11]. Dating back to the 1960s, the earliest study of FRC is with steel fibres [12] [13]. Adding fibres into conventional FRC can increase its toughness thereby preventing, or at least minimizing the crack resulting from temperature or relative humidity. This method can also be utilized in UHPC.

High-carbon metallic fibres like steel fibres are often added to increase strength. In addition, due to the denser matrix, UHPC has an outstanding resistance to chemical attack (e.g., chlorides), abrasion, and fire [8]. Synthetic fibres like alkali resistant (AR) Glass Fibres, AC50 acrylic fibres, and polyvinyl alcohol (PVA) fibres are mainly used for architectural purposes [14]. For example, PVA fibres are sometimes called ‘stealth fibres’ owing to their low visibility in the finished surface. They can also be used together with steel fibres in some low stressed structural components as secondary reinforcement because the modulus of elasticity and the tensile strength are approximately 30 GPa and 1000 MPa, respectively for PVA fibres [15]. In hot temperatures like a fibre accident, some synthetic fibres will melt and create capillary tunnels inside concrete matrix to protect UHPC from spalling.

When designing conventional FRC, the fibre length is recommended to be at least ten times the maximum aggregate diameter to keep a low porosity (or ‘packing density’) [16], which is illustrated in Figure 1-3.

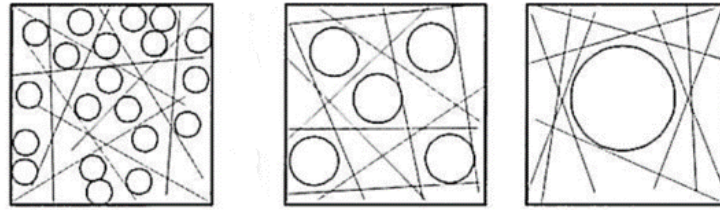


Figure 1-3 Influence of fibre diameter on the matrix porosity [16].

Unlike ‘macro-fibres’ used for conventional concrete (Figure 1-4a), fibres used for UHPC are much thinner and shorter, which can also be referred to as ‘micro-fibres’. A rough dimension comparison between macro and micro-fibres can be seen in Figure 1-4.

For conventional concrete, fibres act as a bridge after concrete cracks. This is more or less like a classic steel bar reinforcement, with steel bars distributed into individual fibres and they are only activated after macro-cracking occurs. In the past, researchers wondered whether to consider fibres in UHPFRC also as a reinforcement or as a part of the composite material itself. So they mixed both macro and micro-fibres with UHPC and proved that the micro-fibres inside UHPFRC were activated as soon as micro-cracking occurred while the macro-fibres were only activated when cracks became larger [17]. From the above, micro-fibres are preferred at a material level.

According to DIN EN 14889-1 [18], a diameter of max 0.2 mm and length of 9-17 mm made from high-strength steel with a tensile strength ≥ 2000 MPa have been proved to be the most suitable option for both mechanical and construction reasons. Also, a length/diameter ratio of at least 65 is recommended. By using these short and slender fibres, the high bond stress between fibres and concrete matrix can be transferred effectively.

Similar to the fibres added in conventional concrete, the steel fibres used in UHPC also have many different shapes and coatings. Although the UHPC matrix is considered to be densely packed and lacks capillary tunnels, some fibres are still subject to corrosion problems resulting from the micro-cracks. Stainless steel fibres (Figure 1-4b) are an advantageous option in this field. Hooked end shape fibres are very common in conventional FRC because the anchorage can increase the bonding effect. However, UHPC

is a much denser material compared to conventional concrete, in most cases, straight fibres is sufficient to fulfil the requirement (Figure 1-4c).

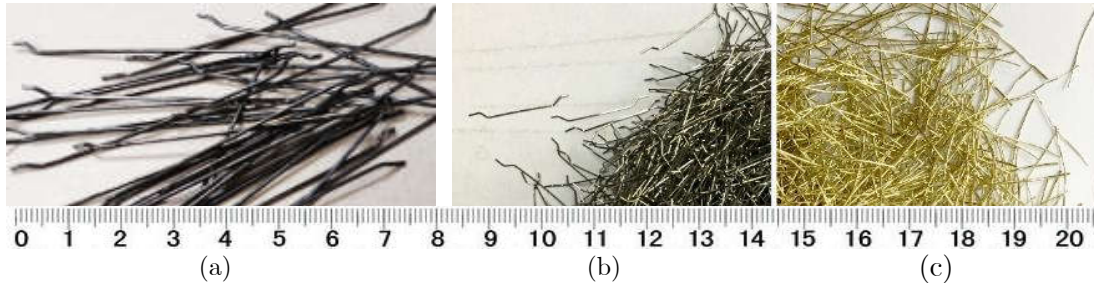


Figure 1-4 Fibres used for conventional concrete (a), stainless (b) and brass coating (c) steel fibres for UHPFRC.

Comparing the tensile strength, the contribution of compressive strength is not that obvious. The uniaxial tensile strength of UHPC is within the range 7-10 MPa. This strength can be doubled with the addition of fibres [8]. Moreover, the fibres can increase the heat and permeability resistance [19]. Rossi [20] explains that the cracking starts as a behaviour of the material itself which also named as ‘micro-crack’, then, it expands to the behaviour of the structure member which is called ‘macro-crack’. Therefore, fibres work efficiently not only for the micro-cracking at the early stage but also the macro-cracks on a structural scale.

Although the steel fibres were firstly investigated in the FRC field, it has some unavoidable disadvantages, for instance, the cost is relatively expensive, and they have severe health and safety issues during construction. Therefore, other types of fibres especially some synthetic (polymer) fibres have been developed to replace steel fibres. Polypropylene (PP) fibres have better resistance to alkali, a comparatively higher melting temperature and a lower cost. One application of PP fibre is in thin sheet components, where it can provide primary reinforcement. In this case, a high fibre volume content exceeding 5% is required. Another typical application is in high-performance concrete. It is used mainly for controlling cracks as secondary reinforcement. In the latter situation, fibre volume content is usually no more than 0.5% [21].

1.1.3 Advantages and applications of UHPFRC

The addition of different types and shapes of fibres can enhance the mechanical properties or practicalities in various ways. To sum up, UHPFRC has the following advantages compared to conventional concrete:

1. Higher compressive and tensile strength;
2. Higher impact resistance;
3. Higher resistance to chemical degradation (chloride and carbonation);
4. Higher abrasion and fire resistance [8];
5. Lower whole life cost including formwork, labour, maintenance, etc.;
6. Faster construction;
7. Better surface appearance.

Being a material on the leading edge of concrete innovation, UHPC can expand architectures' and structural engineers' creative ideas. Figure 1-5 shows the first UHPC bridge called Sherbrooke Footbridge in Canada built in 1997 [22] [23]. Precast trusses and a bridge deck were assembled with two UHPC filled pre-stressed beams.



Figure 1-5 The first UHPC bridge - Sherbrooke Footbridge in Canada [7].

UHPFRC was also widely used in airports (e.g. Haneda Airport in Tokyo), especially designed for heavy wheel loads [24]. Also, UHPFRC can be used in buildings, for example, columns, stairs, and roofs. The enhanced properties allow people to design members with a thin, complex shape, textures (Figure 1-6) or curvatures, which is difficult to achieve with conventional concrete mix due to the addition of coarse aggregates or macro-fibres.



Figure 1-6 LEGO style texture UHPC cladding in France [14].

1.2 Research Gap

Previous researchers had been paying much focus on increasing the matrix properties and investigating new types of fibres. Compared to these studies, fewer efforts were put into the distributions of fibres inside UHPFRC. Rather than being a construction material, UHPFRC is still widely accepted to be a decorative material for creating innovative architectural forms. It is understandable because applying UHPFRC as a construction material requires complete design guidelines, codes or specifications, which needs a detailed understanding of the material properties, structures, and behaviours under loads.

Usually, a homogeneous and isotropic distribution of fibres is assumed in UHPFRC structure design and research simulation modelling. However, a preferred aligned orientation of fibres performs better in controlling the cracks than isotropically distributed fibres in specific cases. For example, when designing the runway at Haneda Airport in Tokyo, engineers tried different procedures (e.g. different placing methods) to optimize the fibre orientation concerning the anticipated aircraft load [25]. Without design guidelines, they needed to test these procedures in the lab and then used as a prototype for actual production.

Although researchers' had developed many test method to detect the location and orientation inside concrete matrix, they did not provide any quantified relationship between fibre distribution and mechanical properties. Nowadays, there are design guidelines in France, Australia, and Japan (design guideline in China is still at the drafting

stage). Some guidelines, e.g. ‘Ultra-high performance fibre-reinforced concrete recommendations’ from AFGC [26] introduces a fibre efficiency factor (reduction factor) K as the difference in defining post-cracking law between the fibre orientation of the standard lab test specimens and real structure members. However, it does not give a more detailed calculation on how fibre orientation distribution affects UHPFRC performance.

However, it is hard to achieve a prescribed distribution because various factors strongly influence it. The fibre distributions covers both spatial and orientation distributions. The spatial distribution is used to describe the fibre volume content at different locations, while the orientation distribution describe the orientation angle of fibres at different locations. From a spatial distribution point of view, the ‘balling effect’ is the most common unexpected bad fibre distribution. From an orientation distribution point of view, the mechanical improvement of this composite material cannot be fully activated if the fibres are poorly distributed or even perpendicularly oriented to the load direction. Therefore, in both research and practice, determining the fibre spatial and orientation distribution in UHPFRC is necessary.

1.3 Aims and Objectives

Based on the existing knowledge and problems, this project is proposed and aims at finding the relationship between the fibre spatial/orientation distributions and the mechanical properties of UHPFRC.

Four objectives are proposed to be achieved in this research, which are:

1. Quantify the fibre distribution within UHPFRC;
2. Conduct mechanical test on the specimens with known fibre distributions;
3. Using finite element method to simulate the fibre distribution in UHPFRC, for both spatial and orientation distribution, and compare with experimental results.

1.4 Thesis Structure

This thesis is divided into nine chapters.

Chapter 1 introduces the development and applications of ultra-high performance fibre reinforced concrete, followed by the research gap, aims, and objectives of this research.

Chapter 2 is the literature review which summarizes the basic material properties of UHPFRC. The factors which affect the fibre distribution are listed. Different fibre distribution test methods are compared.

Chapter 3 states the concrete specimen preparation process. Detailed concrete mix design, mixing, casting procedure, and curing conditions are presented. The workability test is also described in this chapter.

Chapter 4 shows three fibre distribution test methods, which are: cylindrical permanent magnet test, C-shape ferromagnetic probe inductive test, and image analysis test. The experimental principle and experimental setup are explained.

Chapter 5 describes the mechanical test methods, including compressive tests, uniaxial tensile tests, four-point bending tests, and three-point bending tests, again, the testing machines and experimental setups are shown in detail.

Chapter 6 and 7 summarize the results obtained from Chapter 4 and 5. Some discussions and analysis are concluded based on the experiment results.

Chapter 8 takes a deeper investigation on the relationship between the fibre distribution test results and mechanical test results. Theoretical derivations are stated. Then, the correlations are proved by the OpenSees programme.

Chapter 9 concludes all the findings and results in this research. Also, some suggestions and recommendations are given for future work.

CHAPTER 2 LITERATURE REVIEW

UHPFRC can be extensively used in the construction industry only if the relationship between fibre distribution and its corresponding mechanical property can be well understood. This section will briefly introduce the factors that affect the distribution. Furthermore, six common methods in quantifying the fibre distribution will be discussed.

2.1 General Mechanical Properties of UHPFRC

2.1.1 Behaviour in compression

The modulus of elasticity of common UHPC material varies between 45-55 GPa. In a uniaxial compressive strength test, UHPC behaves in a highly linear manner until shortly before it reaches the peak compressive strength (around 0.7-0.8 f_c which can be seen in Figure 2-1). After reaching the peak compressive strength, it always has a sudden brittle failure. A loud explosive sound can be heard during the test. The test sample should have a slenderness ratio (height/diameter) of at least 2. From French guidelines [26], a 70 mm dia. × 140 mm high or 110 mm dia. × 220 mm high sample is recommended.

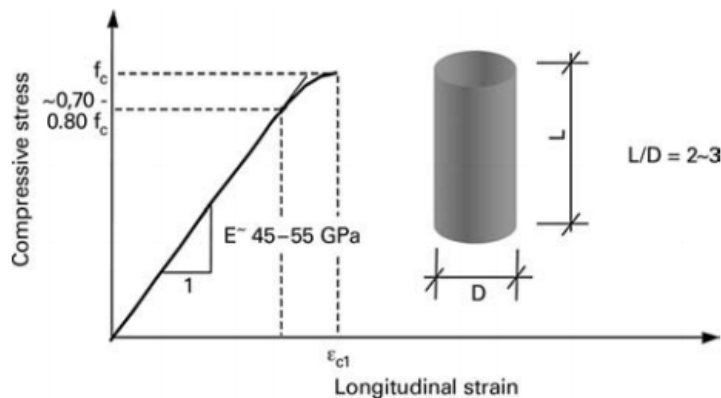


Figure 2-1 Stress-strain relationship for uniaxial compressive test of UHPC [7].

Usually, minor fibre addition does not have a significant effect on the ascending branch of the stress-strain curve, including both the modulus of elasticity and the peak compressive strength. There is about a 15% increase in uniaxial compressive strength

when 2.5% fibre is added by volume [27]. The positive impact is mainly for the post-cracking performance.

Unlike UHPC, UHPFRC has a ductile behaviour reaching the maximum load because fibres restrain the explosive effects of UHPC.

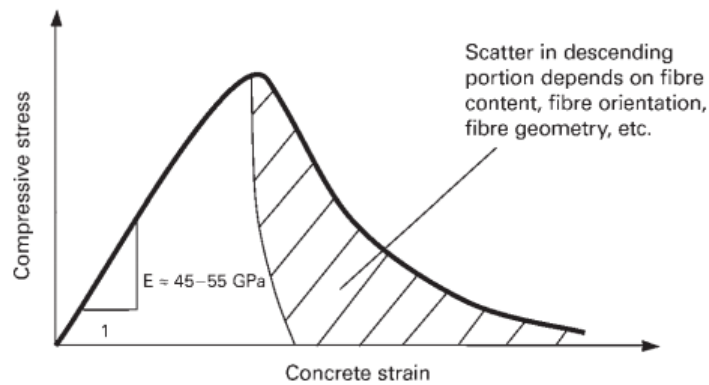


Figure 2-2 Stress-strain relationship for uniaxial compressive test of UHPC and UHPFRC [28].

According to Schmidt (Figure 2-2) [28], the ductility of UHPFRC after cracking highly depends on:

1. fibre volume content;
2. fibre orientation;
3. fibre geometry (length, diameter, and relative size compared to the maximum particle size);
4. fibre stiffness;
5. fibre - concrete bond (surface friction, fibre anchorage, etc.).

2.1.2 Behaviour in tension

Without the addition of fibres, UHPC is highly brittle after crack initiation and therefore almost impossible to measure a steady descending branch in the stress-strain diagram. The tensile strength for plain UHPC is usually between 7-11 MPa. According to Fehling *et al.* [27], and Tue [29], aggregate size does not have a significant effect on the uniaxial tensile strength. The difference mainly results from the quality and size of silica fume.

Compared to the uniaxial compressive test, fibre plays a more vital role in the uniaxial tensile test. The uniaxial tensile test is a direct way to access how fibres attribute to the overall performance of UHPFRC [30]. The behaviour of UHPFRC under tensile load usually contains three main stages: before the initial cracking of UHPC, the strain hardening performance, and the strain softening performance. Figure 2-3 reflects the relationship between strain ϵ , crack width ω and fibre efficiency σ_{cf} in a uniaxial tensile test.

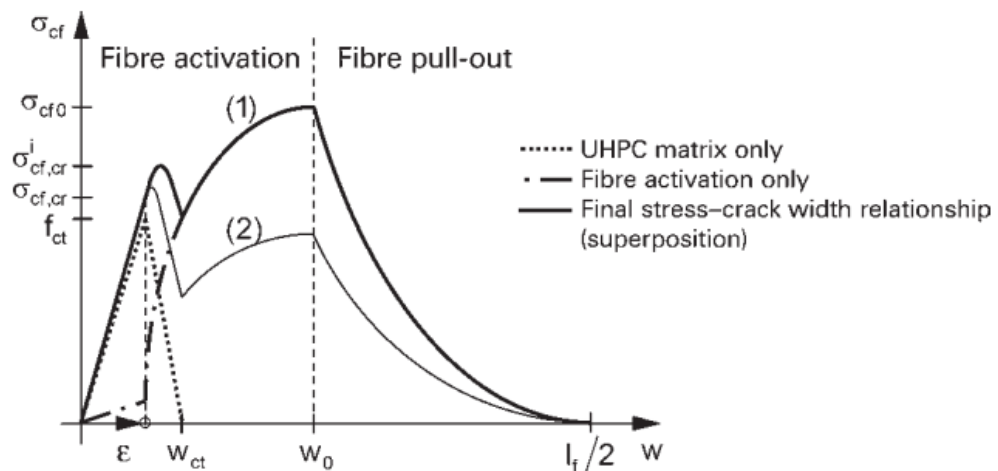


Figure 2-3 UHPC matrix softening, fibre activation, and superposition of two curves [7].

Stage 1: Before the initial cracking of UHPC;

In 2008, Leutbecher [31] studied the load-carrying mechanism of fibres of the uniaxial tensile test. Based on his findings, the fibres and UHPC can be considered as a complete composite material before cracking.

Stage 2: Strain hardening performance;

After UHPC cracks, UHPC is assumed to have a short linear descending portion and fibres are activated. After reaching a certain crack width ω_0 ($\omega_0 = 0.15$ mm in Leutbecher's research [28]), fibres start to be pulled out. The maximum uniaxial tensile load takes place when fibres are fully activated at just the time when they are starting to be pulled out. Strain hardening performance is not guaranteed in the uniaxial tensile test since it highly depends on the fibre distribution inside UHPC matrix. French guideline

define three types of tensile constitutive law by taking the fibre efficiency into account Detailed definition can be seen in the Section 2.1.3;

Stage 3: Strain softening performance;

When the fibres are started to be pulled-out, the load starts to decrease. For the fibres perpendicular to the crack plane, the maximum effective embedment length is equal to half of the fibre length l_f . Therefore, the ultimate limit crack width shown in

Figure 2-3 is l_f , since fibre will not have any effect after that point.

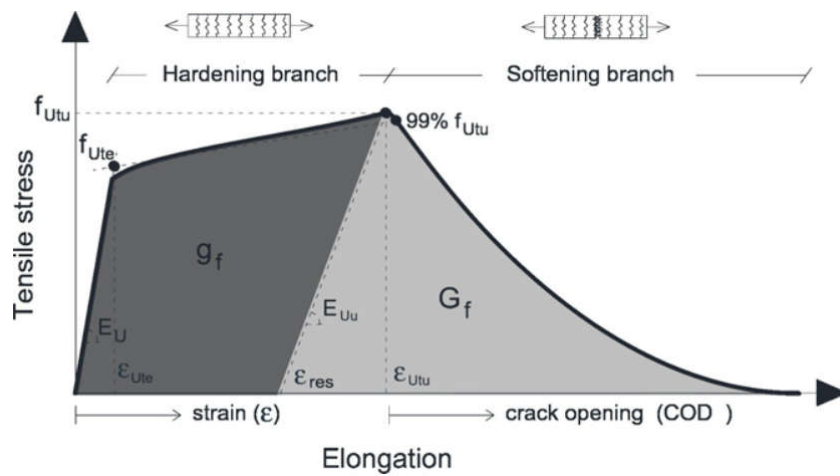


Figure 2-4 Tensile behaviour of UHPFRC [32].

Previous researchers have given two equations to calculate the crack width and fibre efficiency before (Equation 2-1) and after (Equation 2-2) reaching peak uniaxial tensile strength [31] [33] [34] [35].

$$\sigma_{cf} = \sigma_{cf0} \left(2 \sqrt{\frac{\omega}{\omega_0} - \frac{\omega}{\omega_0}} \right), \omega \leq \omega_0 \quad \text{Equation 2-1}$$

$$\sigma_{cf} = \sigma_{cf0} \left(1 - \frac{2\omega}{l_f} \right)^2, \omega > \omega_0 \quad \text{Equation 2-2}$$

The limitation of these two equation is that, they consider all the fibres to be perpendicular to the crack plane, which is not realistic in actual experiment. Although Leutbecher [31] stated that the orientation of fibres across a section between 0-60° had little influence on fibre efficiency since fibres are bent at the cracking surface. Many recent

researchers still hold different opinions since they found fibre orientation and fibre volume content both has a significant influence on the post-cracking performance (Figure 2-5) [7]. Apart from the descending branch, the orientation of fibres still affects the overall performance of the composite material in the ascending portion.

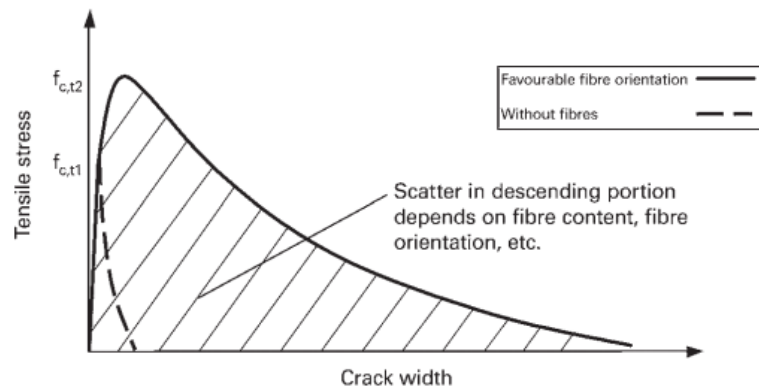


Figure 2-5 Typical stress-crack width behaviour of UHPC in a tensile test [7].

Yet, there are few experimental or simulated formulas that can correlate fibre orientation, spatial distribution to the critical material properties like first cracks strength, peak tensile/flexural strength. As a result, how the fibres are distributed and orientated affect mechanical performance, especially in tensile behaviour is highly significant.

2.1.3 Different tensile constitutive laws

According to French guidelines [26], the tensile constitutive law can be divided into three types. The corresponding stress-strain/crack width graph can be seen from Figure 2-6 to Figure 2-8.

1. Strain softening fibre-reinforced concrete;

This type of material is characterised by the phenomenon that peak strength is determined by the reaching of matrix strength.

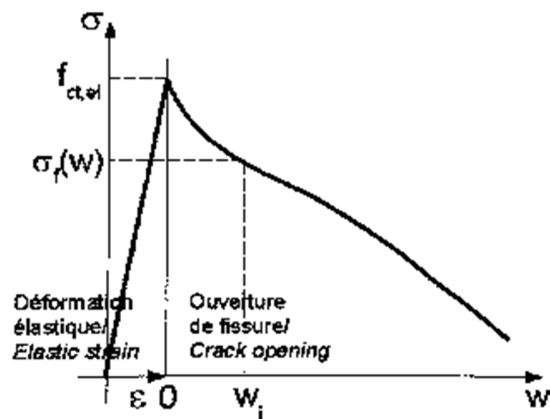


Figure 2-6 Tensile constitutive law of strain softening fibre-reinforced concrete [26].

2. Low strain hardening fibre-reinforced concrete;

This type corresponds to most of the UHPFRC on the market. Generally, the performance is strain hardening. However, considering the fibre alignment and dispersion, the constitutive law is strain softening.

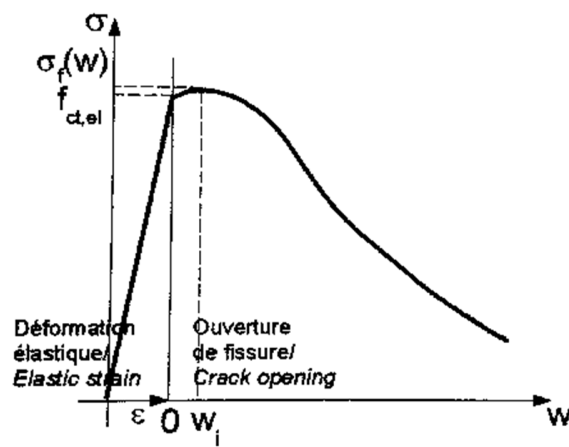


Figure 2-7 Tensile constitutive law of low strain hardening fibre-reinforced concrete [26].

3. High strain hardening fibre reinforced concrete.

This kind of concrete usually equips with very high fibre volume content. Even if the fibre alignment and dispersion are taken into consideration, the post-cracking strength is still higher than the first crack strength.

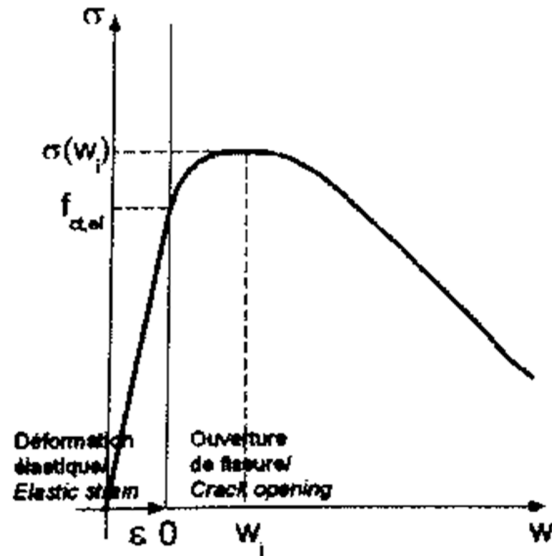


Figure 2-8 Tensile constitutive law of high strain hardening fibre-reinforced concrete [26].

2.1.4 Deriving uniaxial tensile strength from other tests

Performing uniaxial tensile tests on UHPFRC specimens is difficult. Fehling [7] suggested using Equation 2-3 from the EN1992 code [36] to convert compressive strength to uniaxial tensile strength.

$$f_t = 0.3f_c^{2/3} \quad \text{Equation 2-3}$$

According to EN1992, the maximum concrete strength is 90 MPa. He stated that this equation was justified for UHPC, and whether this correlation can be used for UHPFRC is still to be justified. The axial tensile strength calculated from this equation is mainly related to the tensile strength of the UHPC matrix. If the fibre content is high, the fibre efficiency has a higher influence than the UHPC matrix on the axial tensile strength. Therefore, the use of this equation is very limited.

Besides deriving the axial tensile strength from the compressive strength, it can also be derived from bending tests. French guidelines [26] suggest the use of a four-point bending test on un-notched specimens to determine the flexural tensile strength or a three-point bending test on notched specimens to determine the stress-crack width relationship. It

slightly modified the equation from the FIB Model Code 90 [37] and put forward the following Equation 2-4:

$$f_{ct} = f_{ct,fl,el} \cdot \frac{2 \cdot \left(\frac{h}{h_0}\right)^{0.7}}{1 + 2 \cdot \left(\frac{h}{h_0}\right)^{0.7}} \quad \text{Equation 2-4}$$

where

- h_0 100 mm;
- h height of the beam in mm;
- $f_{ct,fl,el}$ extreme fibre stress upon formation of the flexural crack or the elastic limit in MPa.

Compared to the previous method, the effect of fibre also plays a vital role in the bending tests. Therefore, this equation is more accurate even with a sufficient addition of fibre reinforcement.

With fibre reinforcement, a typical flexural strength of UHPFRC is within the range of 15-40 MPa. This figure varies with different specimen sizes because the flexural strength of smaller specimens are more likely to be determined by fibre orientation [7]. Previous researchers had summarized a general relationship between the component thickness and flexural strength, which can be seen in Figure 2-9 [38].

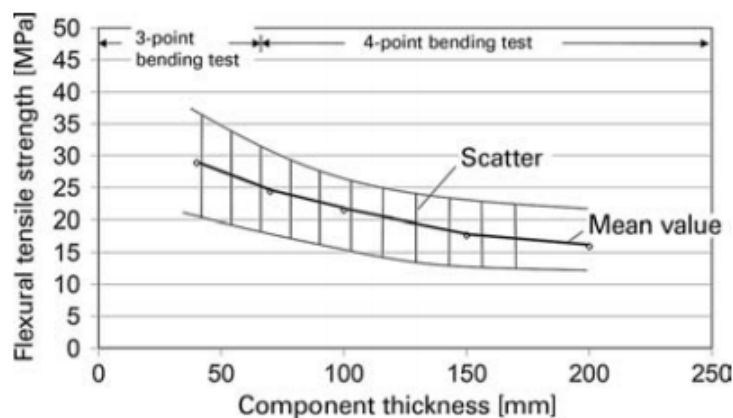


Figure 2-9 Relationship between component thickness and flexural tensile strength [38].

The relationship for these results can be calculated as:

$$f_f = 15 \cdot \left(\frac{200}{H}\right)^{0.45} \quad \text{Equation 2-5}$$

where

H thickness of component in mm;

f_t flexural tensile strength in MPa.

A scale effect factor is also provided in the French guidelines [26] for correction purposes, but the detailed correction factor based on different orientations and distributions is not provided.

2.2 How to Describe Fibre Orientation

2.2.1 Fibre orientation tensor

Orientation is an essential parameter of fibre phase characterization, and it is the main reason of the anisotropy of this composite material. The orientation of a single fibre can be determined in a spherical coordinate system by an in-plane angle φ and an out-of-plane angle θ (Figure 2-10).

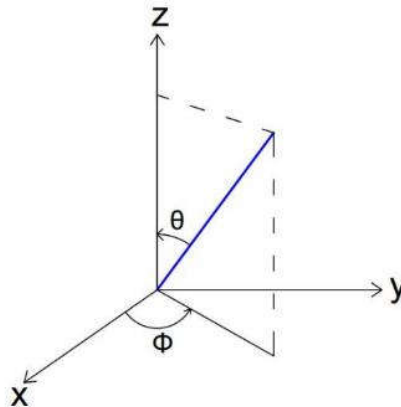


Figure 2-10 Orientation angles of a single fibre.

The probability of finding a fibre with a special orientation vector can be provided with this Orientation Distribution Function (ODF). However, the ODF cannot intuitively express the orientation conditions. Therefore, the orientation tensor is introduced, and

this is defined as the second order moment of the ODF [39]. The orientation tensor can be expressed as a 3×3 symmetric tensor [40] matrix OT shown in Equation 2-6.

$$\mathbf{OT} = \begin{bmatrix} a_{xx} & a_{xy} & a_{xz} \\ a_{yx} & a_{yy} & a_{yz} \\ a_{zx} & a_{zy} & a_{zz} \end{bmatrix} \quad \text{Equation 2-6}$$

$$a_{ij} = \frac{\sum_1^n (p_i p_j)}{n} \quad \text{Equation 2-7}$$

In this equation, a_{ij} represents each component of the orientation tensor, with i and j represent x, y or z direction in the coordinate system (e.g. a_{xx} , a_{xy} , a_{yz} , etc.). Also, in the weighting function, n is the number of fibres for calculating the orientation distribution tensor.

According to Figure 2-10, parameters p_x , p_y , and p_z can be defines as:

$$p_x = \sin(\theta)\cos(\phi) \quad \text{Equation 2-8}$$

$$p_y = \sin(\theta)\sin(\phi) \quad \text{Equation 2-9}$$

$$p_z = \cos(\theta) \quad \text{Equation 2-10}$$

The orientation tensor is symmetric. Therefore only six elements are needed to be defined. The diagonal elements a_{xx} , a_{yy} , and a_{zz} represent the intensity of fibre orientation in the x, y, and z-directions. The non-diagonal elements indicate the combination of the shift of main peaks in the probability density function graph, for example, intensities expressed by the diagonal terms, with a redistribution of angular intensities in the angular space. The corresponding element a_{ij} in the orientation tensor can be derived as:

$$a_{xx} = \frac{\sum_1^n (p_x p_x)}{n} = \frac{\sum_1^n (\sin^2(\theta)\cos^2(\phi))}{n} \quad \text{Equation 2-11}$$

$$a_{yy} = \frac{\sum_1^n (p_y p_y)}{n} = \frac{\sum_1^n (\sin^2(\theta)\sin^2(\phi))}{n} \quad \text{Equation 2-12}$$

$$a_{zz} = \frac{\sum_1^n (p_z p_z)}{n} = \frac{\sum_1^n (\cos^2(\phi))}{n} \quad \text{Equation 2-13}$$

$$a_{xy} = a_{yx} = \frac{\sum_1^n (p_x p_y)}{n} = \frac{\sum_1^n (\sin(\theta)\cos(\phi)\sin(\theta))}{n} \quad \text{Equation 2-14}$$

$$a_{yz} = a_{zy} = \frac{\sum_1^n(p_y p_z)}{n} = \frac{\sum_1^n(\sin(\theta)\cos(\phi)\sin(\theta))}{n} \quad \text{Equation 2-15}$$

$$a_{xz} = a_{zx} = \frac{\sum_1^n(p_x p_z)}{n} = \frac{\sum_1^n(\sin(\theta)\cos(\phi)\cos(\theta))}{n} \quad \text{Equation 2-16}$$

The fibre orientation tensor is widely used in polymer composite researches. It can be obtained by using simulation (e.g. SolidWorks) or calculating from every fibre orientation after doing the sample scanning (e.g. X-ray CT scanning). Defining the orientation tensor is a crucial step in generating a geometry with specified fibre orientation distribution like Digimat software.

There are some general rules for the fibre orientation tensor:

1. The value of the diagonal elements a_{ii} must be within the range 0 to 1;
2. The value of the off-diagonal elements a_{ij} must be within the range -0.5 to 0.5;
3. The sum of diagonal elements $a_{xx} + a_{yy} + a_{zz}$ must equal 1.

Here are some fibre orientation tensors for special distributions,

- 1D aligned (fixed) distribution;

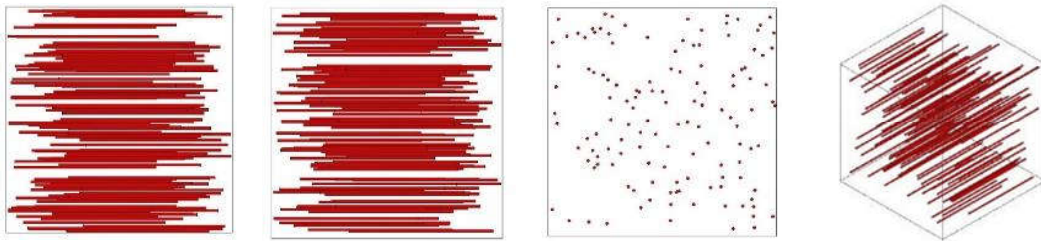


Figure 2-11 Top, front, side, and overall view of 1D aligned fibre orientation diagram.

$$\mathbf{OT}_{1D} = \begin{bmatrix} 1 & 0 & 0 \\ 0 & 0 & 0 \\ 0 & 0 & 0 \end{bmatrix} \quad \text{Equation 2-17}$$

- 2D random distribution;



Figure 2-12 Top, front, side, and overall view of 2D random fibre orientation diagram.

$$OT_{2D} = \begin{bmatrix} \frac{1}{2} & 0 & 0 \\ 0 & \frac{1}{2} & 0 \\ 0 & 0 & 0 \end{bmatrix} \quad \text{Equation 2-18}$$

- 3D random distribution;

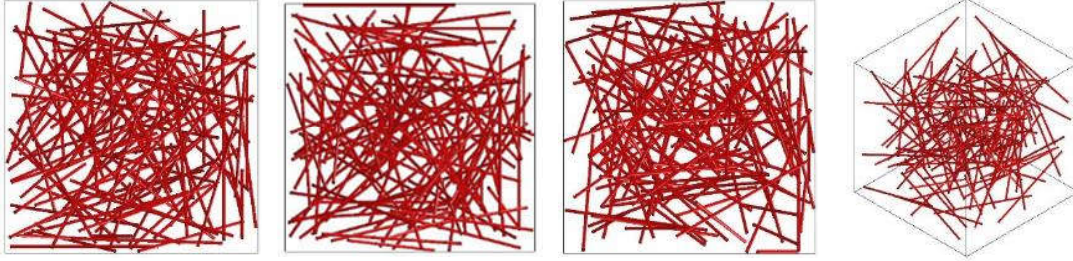


Figure 2-13 Top, front, side, and overall view of 3D random fibre orientation diagram.

$$OT_{3D} = \begin{bmatrix} \frac{1}{3} & 0 & 0 \\ 0 & \frac{1}{3} & 0 \\ 0 & 0 & \frac{1}{3} \end{bmatrix} \quad \text{Equation 2-19}$$

2.2.2 Fibre orientation factor

Other than the fibre orientation tensor, there is another simple way to describe the orientation, which is the ‘fibre orientation factor’. This is more suitable to describe the orientation state at a given cross section, and it can be calculated as [41] [42]:

$$n_f = \alpha \frac{V_f}{A_f} \quad \text{Equation 2-20}$$

where

- n_f number of fibres crossing a unit surface;
- V_f designed fibre volume content;
- A_f cross section area of fibres.

$\alpha=0$ means all fibres are parallel to the cross section while $\alpha=1$ means all fibres are normal to the cross section. One limitation is that it is under the assumption that the fibres do not have segregation. Thus, the spatial distribution is considered homogeneous.

2.2.3 Fibre distribution coefficient

In image analysis, another description of fibre orientation is always used as ‘fibre distribution coefficient’. It describes the spatial distribution of fibres by taking large number of images. It can be calculated as [43] [44]:

$$\beta = \exp\left(-\frac{\sqrt{\sum (x_i/x_{average} - 1)^2}}{n}\right) \quad \text{Equation 2-21}$$

where

- x_i total number of fibres in the i_{th} image;
- $x_{average}$ average number of fibres in all images;
- n total number of images.

According to the definition of fibre distribution coefficient, the higher the fibre distribution coefficient, the more uniform fibres are in the concrete.

2.3 Factors Affecting Fibre Distributions

2.3.1 Aspect ratio and fibre volume fraction

Aspect ratio is calculated by l_f/d_f , while l_f is fibre length and d_f is the fibre diameter. The total fibre-matrix bond increases when a higher aspect ratio or a higher volume fraction of fibre is added. Therefore, the performance of hardened concrete properties (i.e., flexural toughness, peak flexural strength) is improved [21].

Commonly, aspect ratio and fibre volume fraction do not have direct correlations with fibre orientation distribution. However, they might have a bad influence on the workability of fresh concrete and cause construction issues if the aspect ratio is too high

or a large amount of fibres are used. For example, for straight and smooth fibres, if the fibre volume fraction reaches 10%, it is almost impossible to satisfy both the requirement of good workability and uniform fibre distribution because they tend to ball or tangle in the mix [45] [46]. Large sized aggregates can also cause fibre balling during mixing and produce a poor fibre distribution [47].

It should be mentioned that some fibres tend to ball before they are added to the concrete mixture. If they are added in the mixer 'ball-free', they always remain discrete. On the other hand, if the fibres are already interlocked with each other before mixed, they will still keep that state during mixing [21]. The fibre balling effect can severely affect the overall mechanical properties of both conventional FRC and UHPFRC. When balling occurs, the fibres are not able to efficiently bridge the concrete after cracking, but they can also cause a weakness to the completeness of the concrete matrix. To avoid this phenomenon, people usually shake the fibre into the mixer through a screen or produce fibres in bundles of 20 or 30 glue together side by side (Figure 2-14a). Recently, companies have developed fibre dispenser machines (Figure 2-14b) to automatically separate fibres before mixing (Figure 2-14c/d). If some fibres are observed to be clumped or tangled, and there is no efficient way to separate them before mixing, it is highly recommended to replace them with other separated fibres.



(a)



(b)



Figure 2-14 Ways to prevent fibre balling [48].

2.3.2 Extensional flow and wall effect

Even if fibre distribution can be considered as uniform in a mixer, the following casting processes can cause a non-uniform distribution of fibres. The changing of particle orientation induced by shear stress highly depends on the rheological behaviour of the material, which was first explained by Jeffery [49] in 1922 by studying an ellipsoid immersed in a purely Newtonian fluid. Later, researchers applied his theory into a non Newtonian fluid like concrete, and proved that the flow of concrete would influence the fibre orientation [50] [51] [52].

In 2014, Blanco *et al.* [53] did a research on the fibre orientation factor in SFRC slabs. He cast several slabs and drilled cylinders out of the slabs, then measured the fibre orientation using magnetic core inductive tests (explained in Section 2.4.5). Blanco found that the fibres located around the slab centre had similar orientation conditions. The orientation changes when fibres gradually approached slab mould boundary. He claimed that the orientation differences were controlled by the stress of the flow. As can be seen in Figure 2-15, different flow velocities cause the rotation of fibres, consequently, fibres tend to align perpendicular to the direction of the flow. This phenomenon had been proved by many researchers from literature and it is even more obvious with the increase of spreading distance [54] [55] [56].

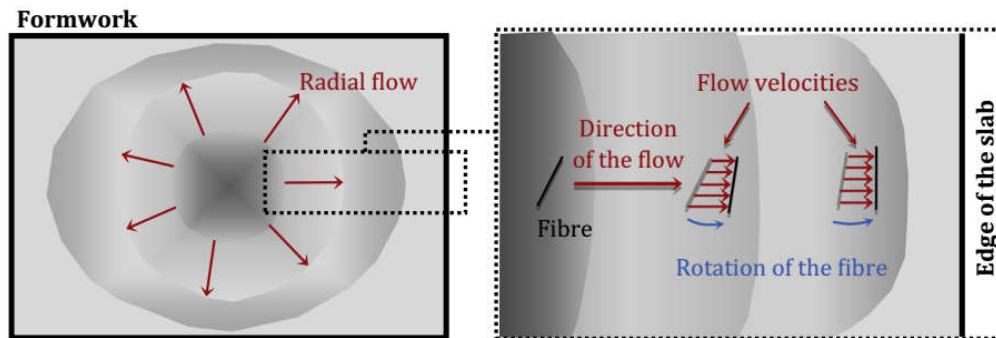


Figure 2-15 Rotation of fibres when moving from the centre to the edges [53].

In 2017, Meng and Khayat did a research by adjusting the rheological properties of suspending mortar and detect the steel fibre distribution [57]. She found the fibre dispersion coefficient increased and then decreased with plastic viscosity. Correspondingly, the peak flexural strength was achieved when the fibre dispersion reached peak value.

This describes the phenomenon that the macro-sopic properties of the fluid (density, viscosity, etc.) in the centre and around the formwork boundary are different. Not only for FRC, but also conventional plain concrete where the aggregates distribute differently near the boundary. In FRC, this effect also leads to a different fibre content/orientation distribution around the boundary of the specimen [21]. This effect is called the ‘wall effect’. It has been shown that the fibres tend to align parallel along the wall [42] [58]. Practically, it is impossible to find a fibre perpendicular to the boundary at a distance smaller than half the length of a fibre. Hence, the area that is affected by the wall effect is a distance of $l_f/2$ from each boundary (Figure 2-16). The influence of the wall decreases with the increasing distance from the formwork. The average orientation factor α (mentioned in Section 2.2.2) reduced from 0.6 to 0.5 in the zone affected by the wall effect to the bulk zone [59].

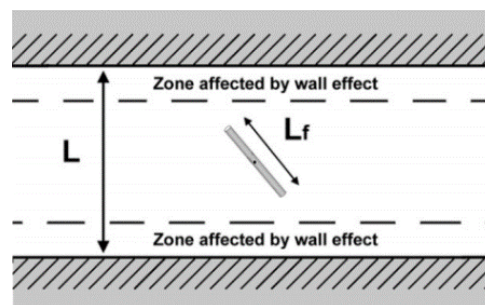


Figure 2-16 Areas affected by wall effect [59].

Not only the fibre length but also the geometry and property of the mould influence fibre orientation [42]. In 2014, research was conducted by Svec *et al* [60] investigating the influence of formwork on the orientation of steel fibres in self-compacting concrete. They cast six 1.2×1.2×0.15 m self-compacting fibre reinforced concrete slabs by pouring the concrete through a rubber pipe inlet near the corner of the mould. The moulds are made of ordinary plywood, glued-sand plywood, or glued-laminated plywood. The surface of these moulds had different roughnesses. The results showed fibres tend to align horizontally along the boundary. Moreover, the roughness of the boundary plays a significant role in affecting the fibre distribution since a rough surface may decrease the fluid shearing, so the fibre orientates more randomly [60]. In order to neglect this effect, it is suggested to cut/saw the samples from larger samples when preparing smaller specimens for quality control.

2.3.3 External vibration

For normal strength FRC, table or poker vibration are often used to expel air in fresh concrete during casting. The investigation of external vibration on fibre orientation can be traced back to 1972, when Edgington and Hannant [61] assumed that the flexural strength relies on the type of vibration and casting direction. Figure 2-17 shows the assumption of Edgington and Hannant. However, due to limited technology at that time, there was no direct evidence (e.g. X-ray CT scanning), so they could only prove this assumption by conducting mechanical tests.

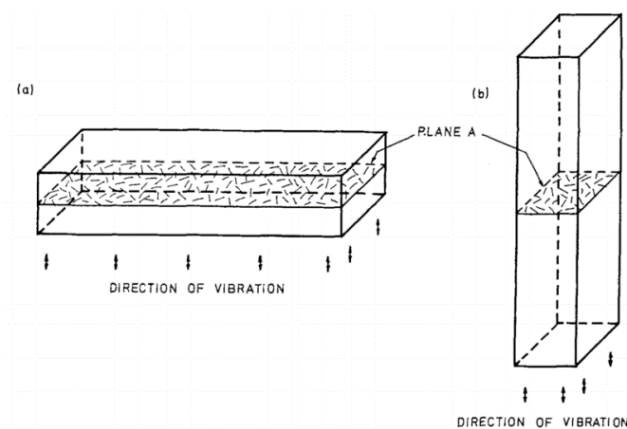


Figure 2-17 Effect of different vibration directions on fibre alignment [61].

Later, different methods were used to test the fibre orientation. In 2004, by using cutting and image analysis, Gettu *et al.* [62] showed that if the workability of normal strength concrete is not too high and internal vibration is only for 1-2 mins, fibre orientation is not influenced seriously, but over-vibration not only causes the fibre to align in a 2D plane but also results in fibre segregation. In 2012, Laranjeira *et al.* [63] stated that according to experimental results, the vibration influences the fibre orientation along the gravity axis (η_y). The longer FRC is vibrated, the more fibres tend to align in the normal to the gravity axis, thus decreasing η_y , with the tendency to a planar fibre orientation [64] [65]. For self-compacting concrete like UHPFRC, vibration is not needed and the flow of fresh concrete plays a more important role.

2.3.4 Mixing sequence

Since fibre distribution has a very close relationship with plastic viscosity, an adequate plastic viscosity often represents a better rheology property thus creates a more uniform fibre spatial distribution. Yang *et al.* [66] stated that water/binder ratio significantly influenced the fibre distribution in a fibre reinforced composite material. However, plastic viscosity cannot be increased easily just by adding more water and superplasticizer, because too much liquid will affect the hardened mechanical properties of the concrete.

In conventional mixing, all the powder materials are added at the same time, then water and superplasticizer are added to initiate the reaction. After the reaction has started, fibres are added. According to this idea, Zhou *et al.* [67] adjusted the mixing sequence by firstly adding part of the powder and liquid materials to produce a mixture. In Zhou's mix design, there was no aggregates but only powders (limestone and cement powders). The largest particles he used were river sands with diameters ranging from 0.25 mm to 0.5 mm. The amount of powders added had been investigated to produce the most suitable flowability for the distribution of fibres. Then, all fibres were added. Finally, all the rest of the materials were added. In this case, a higher plastic viscosity is reached at the beginning to allow the fibres to distribute more uniformly. Figure 2-18 shows the standard

and adjusted mixing sequence. Using this adjusted mixing sequence, the final mix proportion is consistent with standard mixing.

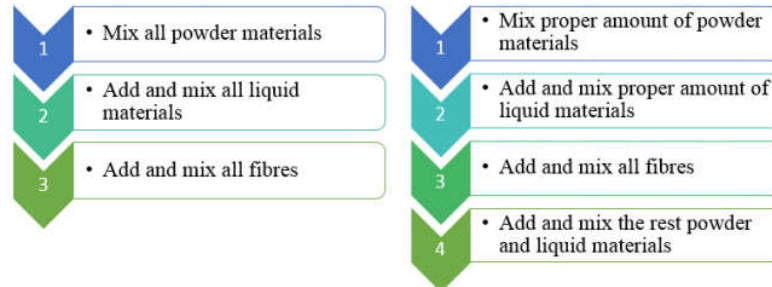


Figure 2-18 Standard (left) and adjusted (right) mixing sequences.

In this research, Zhou *et al.* used an optical microscope to observe and analyse the fibre distribution in the hardened state. Based on the results from the image analysis and observation, Zhou *et al.* stated that the fibre distribution coefficient (described in Section 2.2.3) increased after adjusting the mixing sequence [67]. Furthermore, by conducting materials tests on samples, it was proved that there was a solid correlation between fibre distribution coefficients and tensile strain capacities (Figure 2-19) [67].

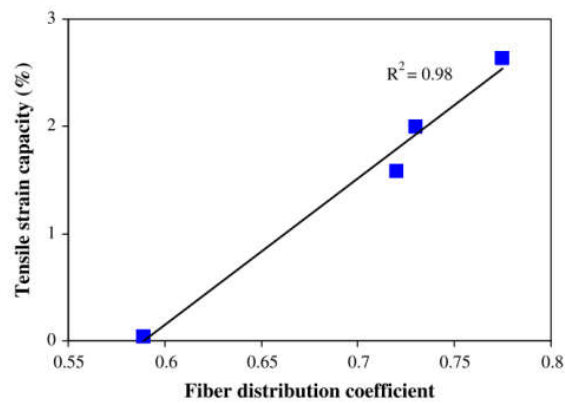


Figure 2-19 Relationship between fibre distribution coefficient and tensile strain capacity [67].

2.4 Methods in Testing Fibre Distribution

2.4.1 Manual visual counting method

Destructive tests include analyzing the cross section surface and statistically surveying fibre orientation and counting the number of fibres manually after crushing a concrete sample [62] [68]. This method is simple and straightforward. Theoretically, it can be used for all materials containing fibres.

However, this method is time-consuming. The accuracy of the results depends highly on the focus and patience of the researchers. It is mostly used for conventional fibre reinforced concrete with a low fibre dosage since the macro-fibres are longer and easier to identify.

Figure 2-20 gives a rough impression on the number of fibres across a 50×50 mm cracking face of a 1% vol. UHPFRC specimen. Calculating using Equation 2-20, the number of macro or micro-fibres crossing a 1% vol. 50×50 mm FRC section face are 88 and 509 (assuming fibre diameters of 0.6 mm and 0.25 mm with both perfectly aligned). The amount of micro-fibres for UHPFRC is very large even for a small dosage, therefore it is impossible to observe and count manually.



Figure 2-20 A 50×50 mm cross section area of 1% vol. UHPFRC sample.

2.4.2 Image analysis method

Image analysis is also a destructive but more scientific and reliable method compared to manual counting. It can be used for both determining fibre spatial distribution and orientation distribution [69] [60] [70] [71] [72]. Figure 2-21 shows the image analysis procedure used by Abrishambaf *et. al* [32].

- (a) Specimen is cut and the section surface is polished;
- (b) RGB photo is taken using a camera of optical microscope;
- (c) RGB photo is processed into a binary photo;
- (d) Cross sections of fibres can be indentified.



Figure 2-21 Image analysis procedures [32].

The orientation of fibre across a crack plane can be calculated from the ellipse mark in the picture. If the ‘ellipse mark’ appears to be a circle in the cutting plane, then it means fibre is perpendicular to the cutting direction. Otherwise, it shows an inclined fibre. The aspect ratio of the ellipse depends on the angle of inclination, or as a rectangle if it lies in the plane (Figure 2-22).

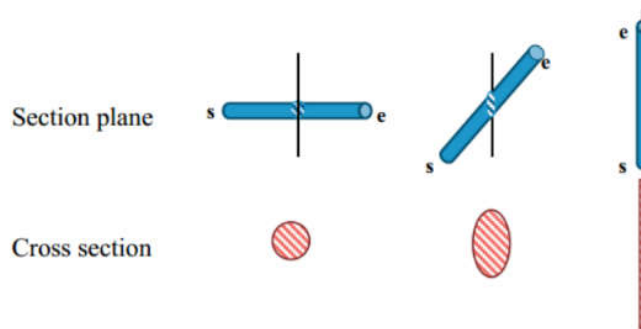


Figure 2-22 Cross section of fibres cut by a plane [73].

The out of plane angle θ can be calculated according to Figure 2-23.

$$\theta = \cos^{-1} \left(\frac{b}{a} \right) \quad \text{Equation 2-22}$$

where a and b stand for the major and the minor axis in the cross section. In this case, $\cos\theta=1$ implies that the fibre is perpendicular to cutting plane.

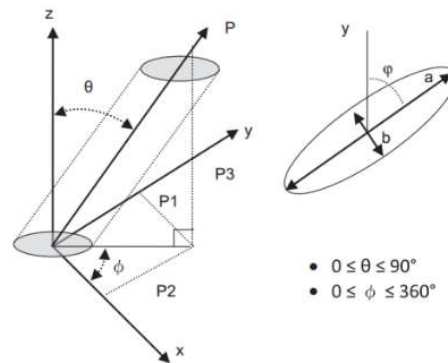


Figure 2-23 3D view of fibre and definition of an ellipse [72].

Spatial distribution is easier to determine. Instead of concentrating on the ellipse recognition on the sectional shape on the cut plane, only the total number of fibres needs to be counted [74]. Compared to all existing methods, this method is considered to be very economical and accurate (if an optical microscope with better resolution is available). However, this method also involves a higher workload since both the cutting and the further analysing process takes a considerable amount of time.

Furthermore, this method is more suitable for testing straight (smooth) fibre distributions. For example, if hooked-end fibre reinforced concrete is cut and analysed, the orientation of the hooked-end is hard to detect. Nowadays, straight and smooth fibres are rarely seen in conventional fibre reinforced concrete because they cannot provide enough bond with the concrete matrix, but it is still very common with UHPC. Therefore, it is still recommended to use this method as a stand-alone test to identify the fibre distributions or as a comparison test to access the accuracy of other non-destructive tests.

2.4.3 X-ray CT scanning method

The most straight-forward approach to precisely measure the orientation and location of every fibre builds on the X-ray Computed Tomography (CT) scanning technique. In 1979, Ashley [75] used X-rays to measure fibre content. Since then, the X-ray scanning method became more popular in obtaining the graphical image of fibres.

X-ray CT scanning usually includes three main stages (Figure 2-24) [76]:

1. A cone beam of X-rays are sent through the concrete specimen on a rotating support;
2. X-rays are collected as radiographs through a flat-panel scintillator detector for each stage rotation angle;
3. Post image analysis software is used to reconstruct 3D images of the interior structure of the sample.

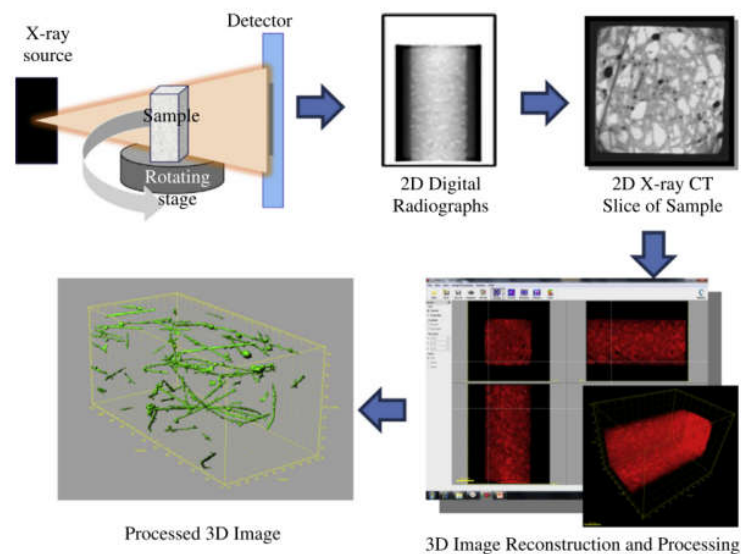


Figure 2-24 Working procedures of X-ray CT scanning method [76].

The selection of X-ray CT scanners usually depends on the dimensions and densities (compositions) of the material. The higher the material density, the higher the greyscale of CT images of the material [69]. For example, in steel fibre reinforced concrete, the density of steel fibre (around 7800 kg/m^3) is much higher than plain concrete (around 2400 kg/m^3), thus steel fibre has the highest greyscale and appears to be the brightest colour from the scanning graph. Hence, fibres can be filtered by setting a relatively higher threshold. Figure 2-25 shows a typical 2D CT image from a conventional steel fibre reinforced section. The white ellipse shape area are fibres, which is surrounded by grey aggregates, darker cement paste and black air voids.

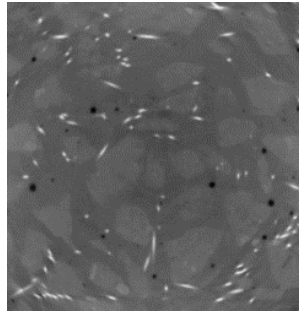


Figure 2-25 An original CT image of steel fibre reinforced sample [69].

However, the opposite is found for polymeric fibres. For example, polypropylene (PP) fibres have a density of around 910 kg/m^3 , which is closer to plain concrete (2400 kg/m^3) compared to the steel-concrete difference, and is more difficult to identify. For most polymeric fibres testing, a contrast threshold needs to be further adjusted and confirmed to select all low density objects (air voids and fibres). Then, the fibres can be filtered by their elliptical shape and size. Finally, adjustments are made to rule out some unusually shaped air voids. Bordelon and Roesler [76] demonstrated in 2014 that 90% of synthetic fibres can be identified by using this method.

When scanning a thicker fibre-reinforced concrete sample, a higher power source X-ray machine is always required to produce a clearly contrasting resolution [76]. Due to technical limitations in the past, the thickness for testing specimens ranged from 10-50 mm. Nowadays, industrial X-ray scanning machines can even be used to scan $150 \times 150 \times 1200$ mm beam samples [77].

After identifying the fibres in the specimen, the fibre orientation tensor (described in Section 2.2.1) can be calculated. Firstly, the fibres in the image are processed using image analysis techniques (as stated in Section 2.4.2) (Figure 2-26a). Then, the image is divided into small areas (Figure 2-26b). Finally, the orientation tensor is calculated in each small area (Figure 2-26c). The orientation tensor is always calculated by projecting the 3D orientation ellipsoids into 2D orientation ellipses [60]. The orientation tensor can be calculated by using image analysis software (e.g., Volume Graphics, VG Studio R) and it can be used directly in the Digimat software to create a geometry which has a similar fibre orientation distribution condition. By using this method, a more reliable model can be created and analysed.

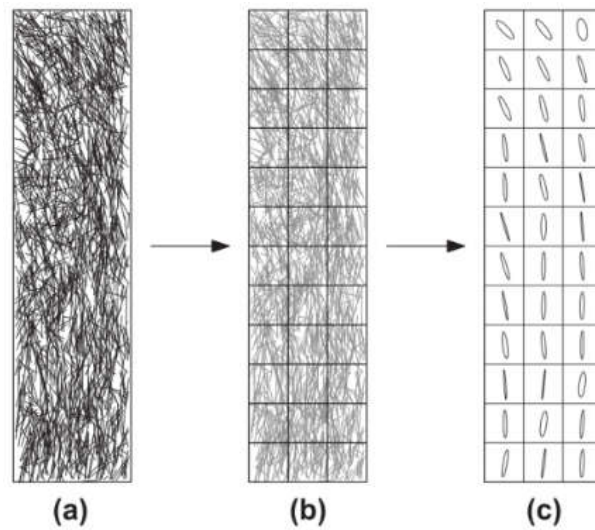


Figure 2-26 Procedure of obtaining second-order orientation tensor from CT image (take 2D projection as an example) [60].

Despite all the advantages that this method has, it can only be used for research purposes since no scanner is powerful enough to scan a pre-cast concrete member on a real construction site. Even in the research lab, using X-ray CT scanning has many health and safety issues, since X-rays are known to be harmful to human health if people are exposed to them. It requires experienced and skillful technicians to operate the scanning machine, which further increases the cost of applying this technique.

This method is not adopted in this research, although using X-ray scanning can get the most accurate orientation and location of each fibre. Based on the market research in China, most X-ray CT scanners are produced for electronic component scanning or medical use. An industrial scanner is very hard to find in the Chinese market. Moreover, the cost for delivering concrete samples to the lab and the testing fee is very expensive. The price for testing one 100×100×100 mm UHPFRC specimen is over 3000 Chinese Yuan (around 430 US dollars or 340 UK pounds). Thus, more economic and convenient methods should be considered instead.

2.4.4 AC-IS method

AC-IS is the abbreviation for Alternating Current-Impedance Spectroscopy. In the past, this method had been used to test hydration development [52], cracking (damage evolution) [78], pore structure [79], and chloride ion diffusivity [35]. Then, it was gradually employed in observing clumping, segregation, and fibre dispersion [80].

In 2006, Ozyurt *et al.* [52] researched using AC-IS to test conductive fibre orientation for industrial scale samples, and it proved to be useful in structural elements. It works by applying an excitation voltage over a range of frequencies to a specimen and measuring the current responses. Because of the oxide film on the steel fibres, conductive fibres are insulating under low frequencies (Hz) of AC. However, they are conductive under high frequencies (MHz) due to the displacement currents short-circuiting the oxide/polarization layer [81] [82].

Figure 2-27 shows the experimental setup of an AC-IS test. The electrodes are submerged in highly conductive NaCl solution reservoir. AC-IS measurement was recorded by testing different regions at different directions and repeated to ensure the stability of the test.

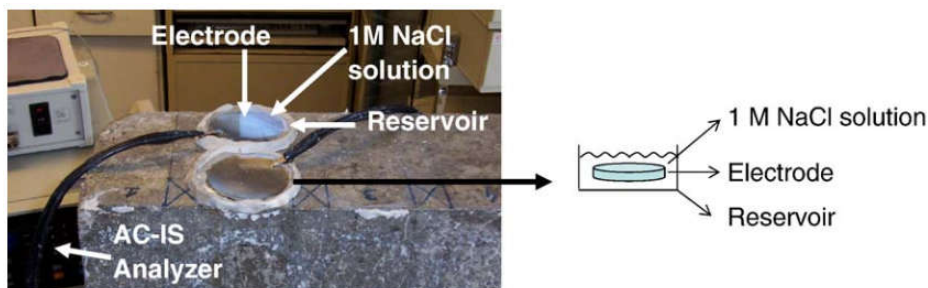


Figure 2-27 Experimental setup of AC-IS test [52].

The data are described in real (x-axis) and imaginary (y-axis) values of impedance and plotted on a Nyquist plot (Figure 2-28). The rightmost curve (electrode curve) is related to the electrode response and does not correlate with the material properties. The bulk curve next to the electrode curve is associated with the material. Plain concrete shows a single arc with a single low-frequency cusp while a high frequency cusp separates two bulk curves with the addition of conductive fibres. To conclude, the occurrence of dual-arc behaviour is the frequency dependent behaviour of conductive fibres [52]. The concrete

matrix conductivity and composite conductivity can be derived from these cusps. By comparing the data obtained from different directions, the fibre orientation can be determined.

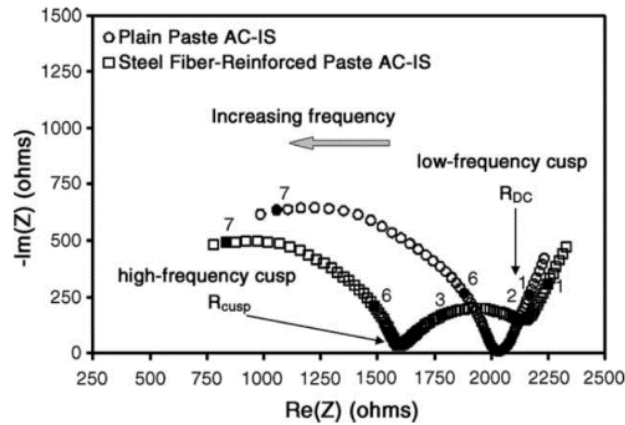


Figure 2-28 Example of Nyquist curves for plain and SFRC [52].

The advantage of the AC-IS is that it is a non-destructive test and it can be used for large-scale specimen testing. The disadvantage is that it can only be applied to conductive fibre reinforced concrete specimens. Moreover, how to prepare a suitable electrode and to match the NaCl solution requires an electrochemical background, thus making it difficult for outsiders. Particularly in this research, the main focus is still on the structure and material performance level rather than the investigation of new testing techniques to identify fibre distribution. Hence, this method is also not adopted in this research.

2.4.5 Magnetic core inductive test method

The magnetic core inductive method is a non-destructive test that uses an electrical coil (Figure 2-29) and its electromagnetic properties to estimate the quantity and orientation of fibres in concrete based on the Faraday electromagnetic induction principle. Its basic concept is related to the variation of the inductance (ΔL) that is observed when a steel fibre reinforced concrete specimen is placed in the middle of an electromagnetic field. Then, if the specimen is located into the coil in different positions, different ΔL levels are measured. The performance of the inductive method depends on the shape of the specimen [83] [84]. In the case of cylindrical specimens, ΔL_T is obtained considering four ΔL readings in different positions: the vertical one (ΔL_z), and three horizontal positions considering three different angles: 0° , 45° , and 90° (ΔL_0 , ΔL_{45} , and ΔL_{90} , respectively). By analysing the sum of them (ΔL_T), the fibre content and its orientation can be estimated [85] [86].



Figure 2-29 Electromagnetic coil used in the magnetic core inductive test.

Similar to the AC-IS test, this test is also used for conductive fibres only. Due to the size limitation of the coil, this test can only be used for small concrete components in the research lab. Common coil dimensions are 200-300 mm in diameter and 300-400 mm in height, depending on the dimensions of the testing specimens. In theory, a larger coil can be made to cope with larger specimens, but this needs further investigation.

2.4.6 C-shape ferromagnetic probe inductive test method

The C-shape ferromagnetic probe test, which is also called as ‘magnetic probe test’ for short, shares the same working principle with the magnetic core inductive test by testing the permeability differences caused by conductive fibres. This method was first proposed by Faifer *et al.* [87] in 2010 and then further developed by Nunes *et al.* [88] in 2016 for fibre distribution detection use of UHPFRC. Nunes made a simple and cheap C-shaped ferrite core with coils wound on it (Figure 2-30a). By placing the probe on 300×300×30 mm specimens (Figure 2-30b) in two orthogonal directions and testing the inductance, the corresponding fibre distribution conditions can be identified. An electromagnetic frame was used to manually adjust the orientation of the steel fibres.



Figure 2-30 Magnetic probe and experiment setup in Nunes’ research [88].

Based on the experimental results, the relationship between the fibre volume content and relative magnetic permeability readings is shown in Figure 2-31.

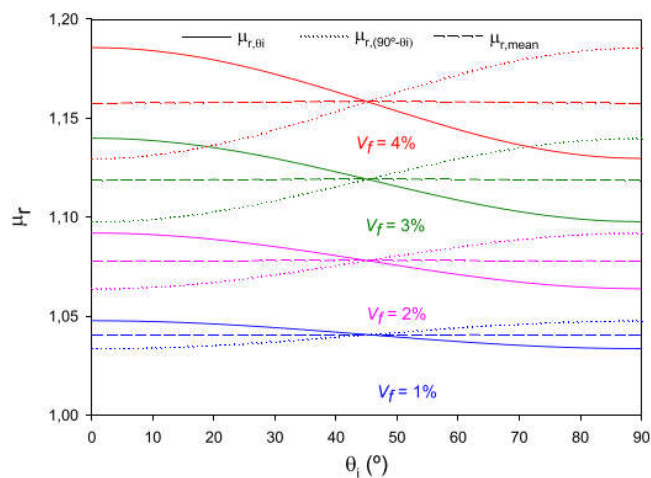


Figure 2-31 Variation of μ_{r,θ_i} , $\mu_{r,(90^\circ-\theta_i)}$, and $\mu_{r,mean}$ with the angle θ_i . [88]

According to Nunes *et al.* [88], a relative magnetic permeability $\mu_{r,mean}$ which reflects fibre content can be calculated as:

$$\mu_{r,\theta_i} = \frac{L_{\theta}}{L_{air}} \quad \text{Equation 2-23}$$

$$\mu_{r,(90^\circ-\theta_i)} = \frac{L_{(90^\circ-\theta_i)}}{L_{air}} \quad \text{Equation 2-24}$$

$$\mu_{r,mean} = \frac{\mu_{r,\theta_i} + \mu_{r,(90^\circ-\theta_i)}}{2} \quad \text{Equation 2-25}$$

where L_{θ_i} , $L_{(90^\circ-\theta_i)}$, and L_{air} represent the magnetic inductance at θ_i , $(90^\circ - \theta_i)$, and in the air.

Figure 2-32 shows the relationship orientation indicator ρ_{Δ} and calculated relative magnetic permeability where

$$\rho_{\Delta} = \rho_{(90^\circ-\theta_i)} - \rho_{\theta_i} = \frac{\mu_{r,(90^\circ-\theta_i)} - \mu_{r,\theta_i}}{2(\mu_{r,mean} - 1)} \quad \text{Equation 2-26}$$

Nunes *et al.* [88] found the orientation indicator has a sinusoidal relationship with the fibre orientation angle, but there was little difference between orientation indicator ρ_{Δ} for different fibre volume content at a given orientation angle, especially the angles between 20° to 70° .

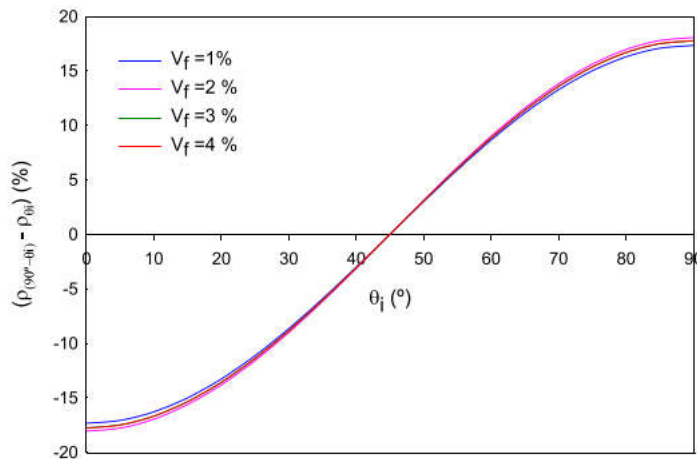


Figure 2-32 Variation of orientation indicator with θ_i for different fibre contents [88].

There are many advantages of this method:

1. Producing the probe is easy and cheap compared to other methods. It only requires an appropriate ferrite core, enough copper wires, and insulated rubber tape. Additionally, an LCR meter is needed for testing the inductance;
2. Applying this method does not require a rich reserve of knowledge and skills since the theory behind this is well investigated;
3. Unlike magnetic core inductive test which is used to test an overall fibre distribution of one specimen, C-shape ferromagnetic probe test is more focused on the particular fibre distribution at one spot. Therefore, it is easier to detect the weak spot in a member;
4. There is no size limitation for specimens using this magnetic probe test. In prospect, it could be used in the construction field as a quality control approach.

2.4.7 Summary

These six methods summarized above have their own advantages and disadvantages. Since this research is mainly focusing on UHPFRC, manual counting is inaccurate and impossible. In the Chinese market, it is hard to find a suitable X-ray CT scanning machine with an affordable price. Hence, X-ray CT scanning is discounted. Compared to the two inductive methods, the theory of the AC-IS method is very complicated and the test requires a deep background study. As a result, the C-shape ferromagnetic probe inductive test together with image analysis were finally chosen to determine the fibre distributions in UHPFRC specimens.

CHAPTER 3 SPECIMEN PREPARATION

After understanding the research gap, a series of experiments was designed based on different types of concrete specimens. This chapter describes the preparation of these specimens. It starts with two different concrete mix designs used in this research, followed by the concrete mixing and casting procedure. A slump test aiming at finding the workability is also explained. Finally, the water and steam curing arrangements are introduced.

3.1 Self-developed UHPFRC Mix

UHPFRC with a target compressive strength of 150 MPa was used in this research. In order to achieve the high compressive strength, 52.5 grade cement was mixed with fine sand, silica fume, ground quartz, water (ice cubes), superplasticizer and steel fibres (Figure 3-1). The maximum grain size of the fine sand was 0.6 mm.



Figure 3-1 All raw materials used in self-developed UHPFRC.

Figure 3-2 shows the steel fibres used in this research. The straight steel fibres were covered with a brass coating to resist corrosion. The diameter and length of fibres were 0.25 mm and 12.5 mm respectively, given an aspect ratio of 50. The uniaxial tensile strength of the fibres can go up to 2850 MPa. It should be noticed that the fibre content added in this research is calculated by volume proportion instead of weight proportion

for convenience. In the following content, '1% vol.' represents the fibre volume content is 1%.



Figure 3-2 Brass coating steel fibres used for UHPFRC.

Table 3-1 shows the control mix proportion for the self-developed UHPFRC mix design without fibres. 1%, 2%, and 3% of steel fibres were added by volume content, given a dosage of 78, 156, and 234 kg/m³.

Table 3-1 Control mix proportion for self-developed UHPFRC.

Material	Content (kg/m ³)
Cement	712
Water	65
Ice cube	65
Silica fume	231
Fine sand	1020
Ground quartz	211
Superplasticizer	40
Total	2344

The original water content should be 130 kg/m³. In the trial casting, the workability of fresh UHPFRC was extremely poor. The reason being that most concrete castings were finished in summer at a room temperature over 30°C. The high temperature resulted in the quick evaporation of water during mixing and reduced the actual amount of water for hydration reaction with the cement.

To lower the mixing temperature, some ice cubes (around 20 mm in size) were used to replace half of the total water amount (65 kg/m³ ice cubes and 65 kg/m³ water). Given the time for melting the ice cubes, the reaction time was longer compared to other UHPFRC mixes with all water. The mixing temperature was controlled to be below 28°C

to ensure good workability. Table 3-2 records the mixing sequence with detailed time durations. Actual mixing times varied ± 1 min depending on the temperature and humidity on the casting date. The addition of fibres may also increase the mixing time accordingly. This self-developed mix design is referred as ‘SD mix’ in the following content.

Table 3-2 *Mixing procedure and time for self-developed UHPFRC.*

Procedure	Duration (min)
Mix sand and powder material	10
Add water, ice cubes, and 50% superplasticizer	30
Add fibres	3
Add 50% superplasticizer	3

3.2 UHPFRC Mix with Pre-mix Powders

Although the concrete strength produced from the self-developed mix design can fulfill the strength requirement of this research, there were still some apparent disadvantages. Firstly, the mixing time was too long because of the melting of the ice cubes. Secondly, the cement used for SD mix design was kept in a plastic bucket without any effective sealing measures. Most castings were conducted in summer, which was especially rainy and humid in Suzhou. Some cement powder was found to be agglomerated in this condition. Thus, it was hard to maintain the consistency of cement for every batch. Thirdly, weighing all the raw materials individually cost more time and labour.

In order to save the mixing and casting time, pre-mix powder and superplasticizer provided by company were used in the latter part of the experimental work. The pre-mix powder was delivered using sealed plastic bags wrapped with outer paper packaging as can be seen in Figure 3-3. This packaging ensured the freshness of the cement.



Figure 3-3 Pre-mix powder provided by company.

The dry pre-mix powder material contained the basic components needed for UHPFRC (cement, fine sand, silica fume, quartz, and active agent), but the detailed proportions were unknown due to company confidentiality. Since this research is mainly focused on the distribution of fibres, this material can be adopted as long as the concrete strength can reach the ultra-high strength and keep consistency for every batch. Figure 3-4 shows all the raw materials used in this design, including pre-mix powder, water, steel fibres, and superplasticizer.



Figure 3-4 All raw materials used in pre-mix UHPFRC.

By using these materials, five more UHPFRC batches were cast with 0, 1%, 2%, 2.5%, and 5% fibre volume content, given a dosage of 0, 78, 156, 195, and 390 kg/m³. Detailed control mix proportions without fibres can be seen in Table 3-3.

Table 3-3 Control mix proportion for pre-mix UHPFRC (provided by company).

Material	Content (kg/m ³)
Dry-mix	2200
Water	192
Superplasticizer	20.5
Total	2413

Table 3-4 shows the suggested mixing procedure and mixing time provided from the supply company. The overall mixing time was much shorter comparing to the self-developed mix design. First of all, there was no need to mix all the powder materials. Secondly, the hydration reaction took less time because of the addition of the active agent. Considering environmental and fibre amount differences, the mixing time varied by ± 30 seconds. This mix design provided by the supplier is referred to as ‘Pre-mix’ in the following content.

Table 3-4 Mixing procedure and time for pre-mix UHPFRC.

Procedure	Duration (min)
Mix pre-mix material	1
Add superplasticizer and 2/3 water	6
Add 1/3 water	3
Add fibres	1

3.3 Concrete Mixing

For both two types of concrete mixes, a DEX MP500/330 planetary mixer was used to mix the concrete (Figure 3-5a, b). The maximum capacity for this mixer is 1 m³. Before mixing, the mixer was cleaned and moisturized to prevent the water absorption by the inner walls. Also, it helped cool down the mixer temperature. A humidity and temperature tester was used to monitor the temperature change. Generally, the mixing temperature was controlled below 28°C to ensure good workability.

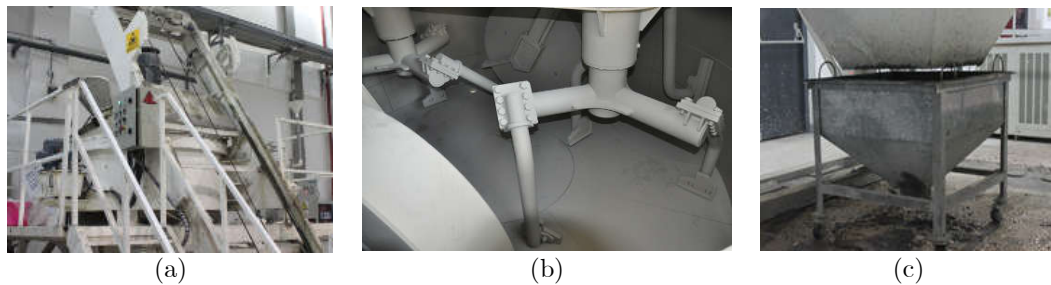


Figure 3-5 Concrete mixer (a) (b) and funnel (c) used in concrete casting.

Although the mixing sequence for the two mix designs were slightly different, the overall hydration process performance was similar. After liquid (water, ice, and superplasticizer) was added to the powder material, the hydration reaction of the cement began. During mixing, some water beads were covered with powder material resulting in small cement balls (can be seen in Figure 3-6). Then, these small cement balls were shattered by the mixer.

After adding all liquid, the chemical reaction was heightened. As the mixing time goes on, the concrete colour became darker and more viscous. When the concrete was flowable and contained no cement balls, fibres were added at a constant rate to avoid the fibre balling effect. Concrete mixing continued until no fibre can be seen. After mixing, fresh concrete was poured from the mixer to the casting funnel, which is shown in Figure 3-5c.



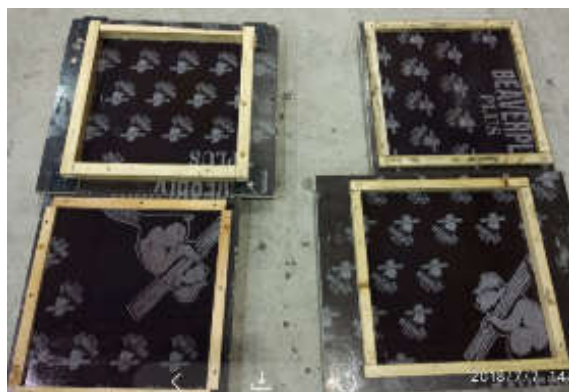
Figure 3-6 Concrete balls during mixing.

During concrete mixing, all moulds were oiled to assist demoulding. Figure 3-7 shows some moulds used in this research.

- (a) Wood moulds for 75×75×450 mm beams;
- (b) Wood moulds for 500×500×15 mm, 500×500×20 mm, 500×500×35 mm, and 500×500×50 mm slabs;
- (c) Plastic moulds for 100×100×100 mm cubes, 100 dia. × 200 mm cylinders, and 100×100×400 mm beams;
- (d) Steel moulds for 380×150×50 mm dog bone shape specimens.



(a)



(b)

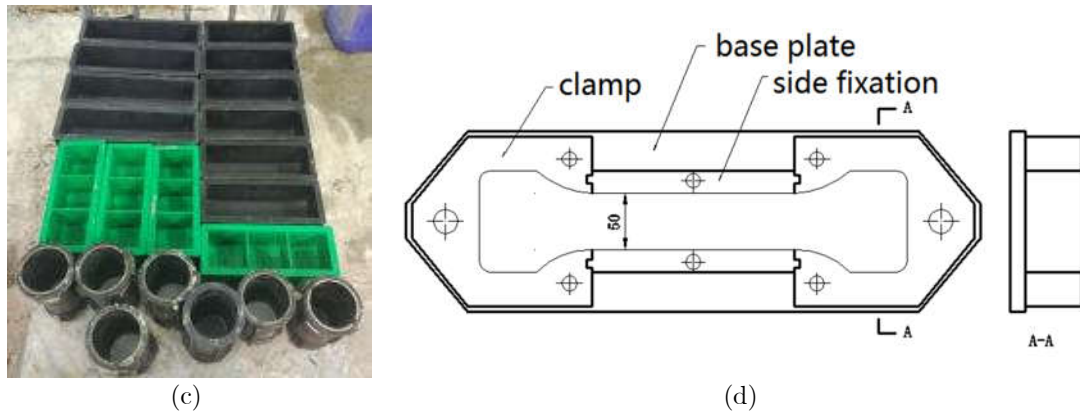


Figure 3-7 Concrete moulds used in the research.

Table 3-5 lists the dimensions and casting purpose of all specimens. Since the number of specimens were different in every batch, the detailed amounts and properties of specimens are listed in Appendix 1.

Table 3-5 Specimen list and casting purpose for different types of specimens.

Shape	Dimension (mm)	Casting purpose	Total amount
Cylinder	D100, H200	Compressive test	12
Cube	100×100×100	Compressive test	42
Thin slab	160×160×10	Magnetic probe test	3
Dog bone	380×150×50	Uniaxial tensile test	12
Beam	75×75×450	Flexural test, Magnetic probe test	24
Beam	100×100×400	Flexural test, Magnetic probe test	16
Slab	500×500×15	Flexural test, Magnetic probe test	1
Slab	500×500×20	Flexural test, Magnetic probe test	1
Slab	500×500×35	Flexural test, Magnetic probe test	1
Slab	500×500×50	Flexural test, Magnetic probe test	1

3.4 Concrete Casting

By opening the valve of the funnel, fresh concrete would flow into the mould. The casting method can be summarized as:

1. All the cubes, cylinders, and dog bone specimens were cast in three layers with minor vibration by hand to expel the air trapped in the fresh concrete;
2. For slabs, concrete was poured from the centre towards the four edges (see Figure 3-8a). No table vibration was used to avoid the segregation of fibres;
3. All the beams were cast in two layers with minor hand vibration. Concrete was poured from the centre of the beam and flowed to the two ends until the beam was fully filled with concrete (see Figure 3-8b);
4. For some special batches, half of the beams were vibrated on the vibration table for 15 minutes with a frequency of 50 Hz when casting.

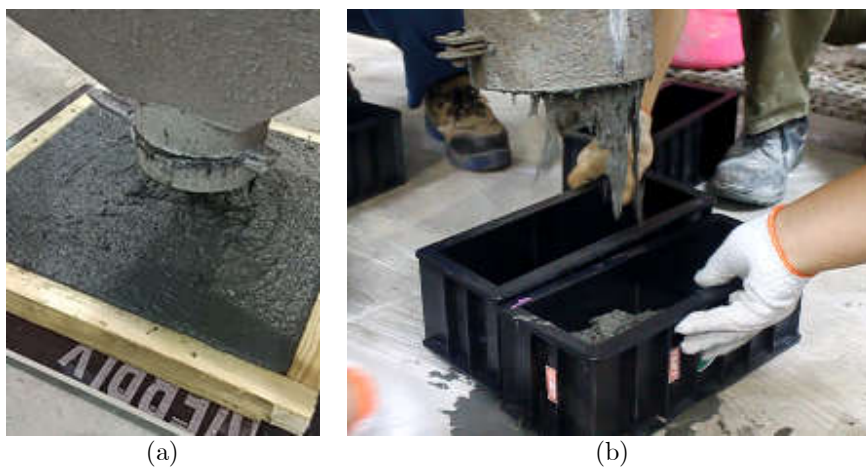


Figure 3-8 Cast slabs (a) and beams (b).

3.5 Workability Test

Since the workability has a significant relationship with concrete properties and fibre distributions, a slump test was carried out on some of the concrete batches based on the code GB50119-2013: Code for concrete admixture application Appendix. A [89]. The testing equipment included an 8 mm dia.×300 mm long steel bar, a 500×500×5 mm glass slab, and a steel cone (see Figure 3-9a). The upper and bottom diameters of the cone were 50 mm and 100 mm respectively. The height of the cone was 150 mm. The procedure of the slump test can be summarized as:

1. Place the glass slab on a horizontal surface, moisturize the glass slab, steel bar, and steel cone using a wet cloth;
2. Put the cone in the middle of the glass slab and cover it with the wet cloth while waiting for the fresh concrete mix;
3. Fill half of the steel cone with fresh concrete and compact the concrete 15 times clockwise from cone centre to cone edge;
4. Repeat the previous step for the remaining half;
5. Smooth the top surface and lift the cone vertically (Figure 3-9b);
6. After 10 seconds, measure the expanding diameter (Figure 3-9c) in two perpendicular directions. The average value of these two measurements is the result for the slump test.

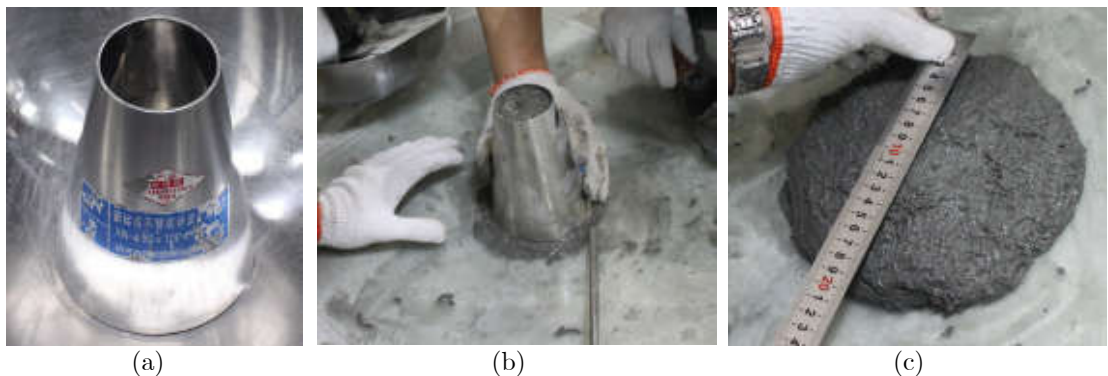


Figure 3-9 Slump test for fresh UHPFRC.

3.6 Concrete Curing

All the fresh concrete specimens were covered with a plastic film (Figure 3-10) to prevent the early shrinkage due to water evaporation.



Figure 3-10 Fresh concrete covered with plastic film.

After 24 hours of hardening, all specimens were demoulded. The base slabs of dog bone shape specimens were removed to avoid the irregular concrete swelling during curing. All the specimens made from the self-developed concrete mix were cured in the water curing tank (Figure 3-11a). For the specimens made from pre-mix powders, steam curing (Figure 3-11b) was recommended by the supplying company to maximize the concrete strength.

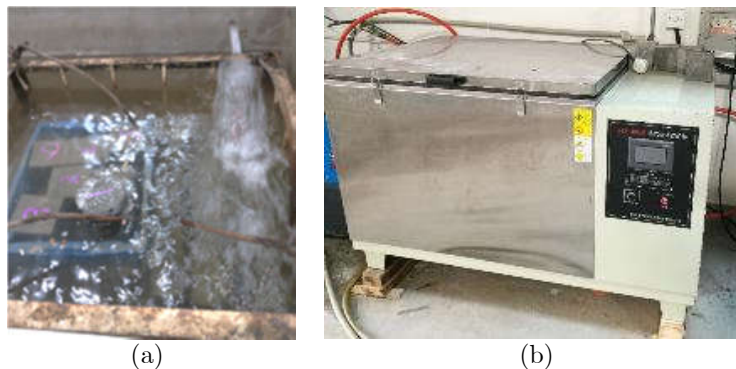


Figure 3-11 Water (a) and steam (b) curing tank.

The curing time was the same for all specimens, which included 2 hours for increasing the curing temperature to 90°C and then another 48 hours curing at 90°C. Both the water and steam curing tanks did not have a cooling function. After curing, the tank lid was slightly opened for cooling to prevent a shrinkage cracking due to the sudden temperature drop. All the UHPFRC specimens were tested at an age of 7 days.

CHAPTER 4 FIBRE DISTRIBUTION TEST METHOD

The distribution of fibres were tested after concrete curing. Based on the literature review, the C-shape ferromagnetic probe test was chosen to be the detecting method in this research. In this chapter, a cylindrical permanent magnet test is invented and used to test the spatial distribution. Then, the C-shape ferromagnetic probe test method is explained in further detail. Finally, image analysis conducted by MATLAB is introduced to validate the result obtained from magnetic probe test.

4.1 Cylindrical Permanent Magnet Test Method

4.1.1 Theoretical derivation

Magnetic permeability is a material property that describes how a material responds to magnetism. This property is usually shown by what extent a magnet attracts the material. The force to separate a magnet from a small steel block is smaller than a big steel block if the steel block is made from the same material. Therefore, calculating the attracting force between a permanent magnet and steel fibre reinforced concrete can be used to detect the spatial distribution of steel fibres in the concrete.

Some derivations have been made to calculate the relationship between the magnetic force and fibre content. According to Wang [90], the magnetic force F_m can be expressed as Equation 4-1, where μ_v and μ_f represent permeability of vacuum and relative magnetic permeability of fibres. B_m represents the magnetic flux density. S represents the reaction area between the magnetic field and the steel fibres.

$$F_m = \frac{\mu_f - 1}{2\mu_v\mu_f} \iint B_m dS \quad \text{Equation 4-1}$$

As stated in the next section (Section 0), the testing area was very close to the size of the permanent magnet. To simplify this equation, the magnetic flux density is considered to

be the same within testing areas like a uniform magnetic field. Therefore, Equation 4-1 can be simplified to

$$F_m = \frac{\mu_f - 1}{2\mu_v\mu_f} B_m S \quad \text{Equation 4-2}$$

For non-ferromagnetic materials, the relative magnetic permeability is very close to the permeability of a vacuum. For a ferromagnetic material like steel, the magnetic permeability is much larger than the permeability of a vacuum ($\mu_f \gg 1$) [90]. Therefore, the magnetic force can be further simplified to

$$F_m = \frac{B_m S}{2\mu_v} \quad \text{Equation 4-3}$$

160×160×10 mm UHPFRC slabs were used to verify this equation. Since the slab depth was smaller than the fibre length ($l_f = 12.5$ mm), fibres distribution can be considered as a 2D distribution (horizontal distribution). Therefore, the reaction area between the magnetic field and the fibres can be calculated as:

$$S = d_f \cdot l_f \cdot \frac{V_s \cdot V_f}{\pi \cdot \left(\frac{d_f}{2}\right)^2 \cdot l_f} = \frac{4V_s \cdot V_f}{\pi \cdot d_f} \quad \text{Equation 4-4}$$

where

- d_f diameter of steel fibre;
- l_f length of steel fibre;
- V_s volume of the testing area;
- V_f fibre volume content.

Combining Equation 4-3 and Equation 4-4,

$$F_m = \frac{2B_m \cdot V_s \cdot V_f}{\mu_v \cdot \pi \cdot d_f} \quad \text{Equation 4-5}$$

It can be seen from Equation 4-5 that if the types of the permanent magnet and steel fibres used remain the same, the magnetic force is linearly related to fibre volume content.

4.1.2 Test setup

In order to verify this Equation 4-5, a cylindrical permanent magnet test was proposed. Initially, this experiment was designed to be as Figure 4-1a. The load was measured by an S-shape force sensor. A cylindrical permanent magnet was glued to the bottom of the sensor. A string was tightened to the top of the force sensor. By pulling the string, the load can be recorded by the S-shape force sensor. However, during the experiment, it was hard to pull up the magnet uniformly and one side was always pulled up first. This unbalanced behaviour caused a big fluctuation and led to inaccurate results. In the next experiment, the string was replaced with a steel bar (Figure 4-1b). After replacement, the unbalanced situation was slightly relieved but it still existed. Therefore, this test setup was abandoned.

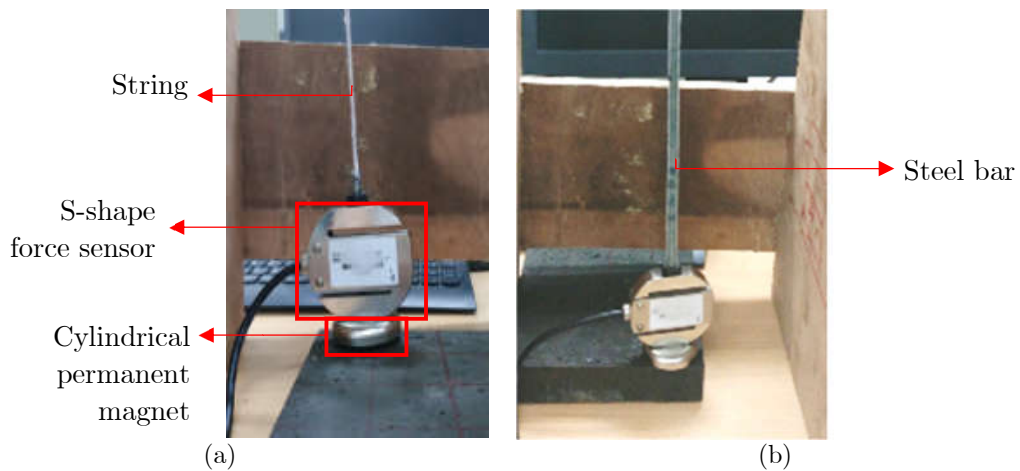


Figure 4-1 Initial cylindrical permanent magnet test setup.

With the purpose of increasing the force measurement accuracy, a Flexiforce A40 force sensing resistor (FSR) (Figure 4-2b) was adopted. The force sensing resistor was a polymer thick film device which exhibited a decrease in resistance with an increase in the force applied to the active surface. The thickness of the sensor was 0.203 mm. The diameter of sensing area was 25.4 mm. The FSR had a measuring range of 110 N with an accuracy less than $\pm 3\%$.

The FSR was connected to an analogue/digital converter (Figure 4-2b). The analogue/digital converter was used to translate the resistance to a voltage signal. By applying this equipment together with the LabVIEW software, the voltage can be

recorded and further converted into force. The cylindrical permanent magnet (Figure 4-2a) was an N42 Neodymium magnet with Ni-Cu-Ni coatings. The diameter and thickness of the magnet were 25 mm and 10 mm.

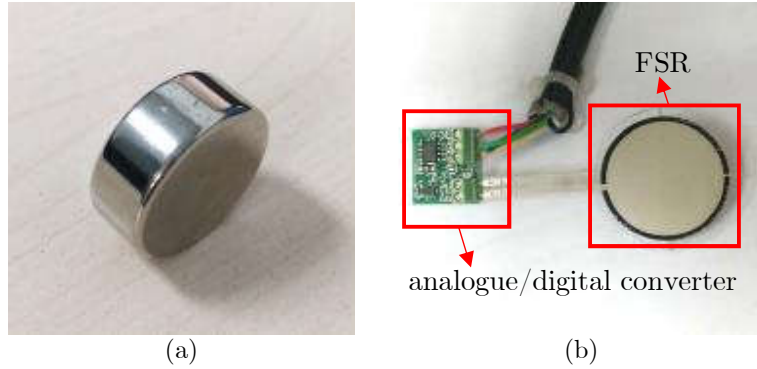


Figure 4-2 Cylindrical permanent magnet and FSR used in the experiment.

Three 160×160×10 mm UHPFRC slabs were used in this research. The fibre volume content was designed to be 0.5%, 1%, and 2.5%. Each slab was divided into 16 small sections as shown in Figure 4-3. Each section had a dimension of 40×40×10 mm.

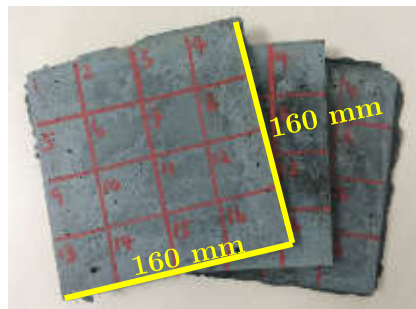


Figure 4-3 UHPFRC slabs used in cylindrical permanent magnet test.

The bottom surface was used as the testing surface since it was smooth and flat. The experimental setup was shown in Figure 4-4. The force sensing resistor was placed on every centre point of the small sections. Then, a permanent magnet was placed on top of the sensor. Instead of testing the pull-up force, the attracting force between the magnet and steel fibres were measured. In this case, the force tended to be more stable and reliable.

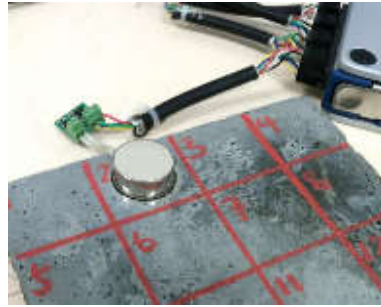


Figure 4-4 *Final cylindrical permanent magnet test setup.*

The test was designed mainly for quality control purposes in the construction field. There are some typical advantages for this method:

1. Testing equipment is cheap to build;
2. Testing method is easy to carry out and there is no need to train a skilful technician;
3. No delay in getting the test results;
4. Can be used to detect fibre distribution in specific points.

4.2 C-shape Magnetic Probe Inductive Test Method

4.2.1 Probe specification

A magnetic probe was made based on Nunes' research [88]. The ferrite core used in this research was 76 mm tall, 93 mm long, and 30 mm wide. Detailed dimensions of the magnetic probe can be seen in Figure 4-5.

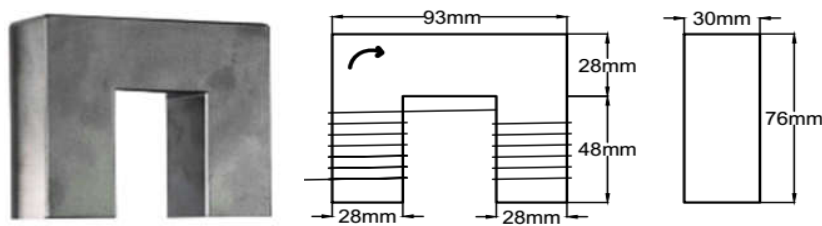


Figure 4-5 Appearance and detailed dimensions of ferrite core.

The probe (Figure 4-6a) was made of a high frequency inductive Mn-Zn ferrite core wrapped by 350 turns of 0.9 mm diameter enamelled copper wire (Figure 4-6b). Black insulated rubber tape was wrapped tightly to the wires to protect the safety of users.

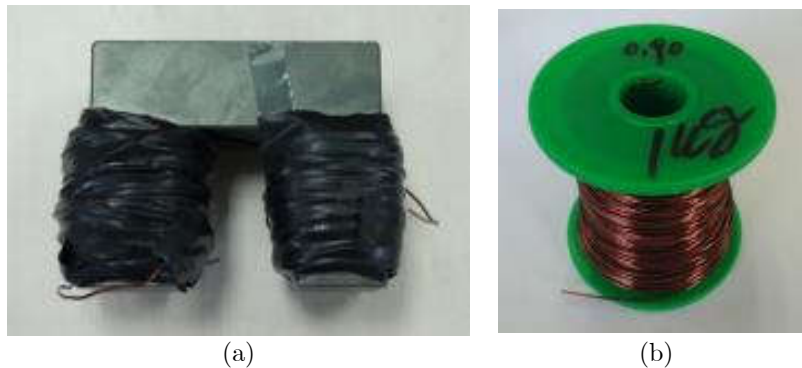


Figure 4-6 Magnetic probe (a) and copper wire (b).

The inductive test was carried out after finishing curing. The magnetic probe was placed on a smooth surface of the UHPFRC specimen and the probe was connected to the LCR meter with two clips (Figure 4-7). With the inductance value measured by the LCR meter, fibre orientation and spatial distribution could be determined.

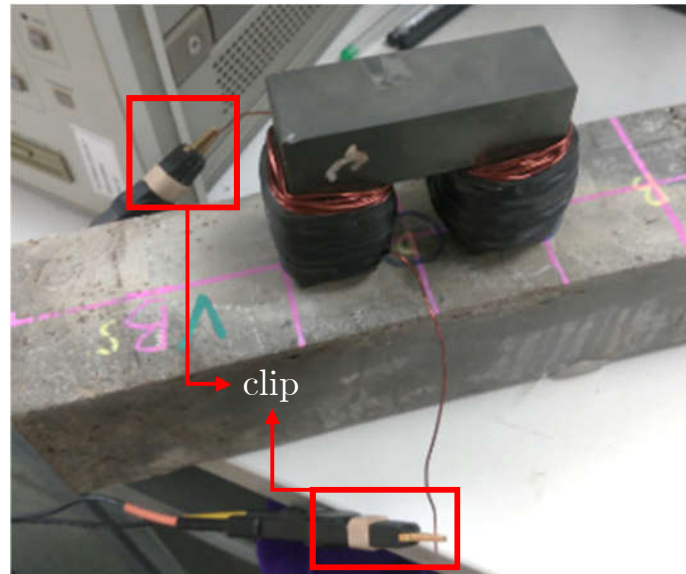


Figure 4-7 C-shape magnetic probe inductive test setup.

Two LCR meters were used to obtain the inductance measurements. In the beginning, an Agilent HP4284A (Figure 4-8a) LCR meter was used from in the lab of Department of Electrical and Electronic Engineering in XJTU. It had a testing range of 20 Hz to 1 MHz. Since more specimens were going to be tested in later research, it was very inconvenient to borrow the LCR meter every time. Therefore, a Tonghui TH2830 LCR meter was purchased and used instead. The testing frequency of this meter ranges from 50 Hz to 100 kHz. The accuracy of this LCR meter was 0.05%. Fast (75 times/sec), medium (83 times/sec) and slow (370 times/sec) testing speeds can be chosen for different testing situations.



Figure 4-8 Agilent HP4284A (a) and Tonghui TH2830 (b) LCR meter.

According to the literature [88], the inductance remained steady and almost constant from 20 Hz-2 kHz. For the Agilent HP4284A LCR meter, 50 Hz with a test signal of

100mV was applied. The test was repeatable and the inductance results were steady with an accuracy of ± 0.01 mH.

However, when using the Tonghui TH2830 LCR meter, the inductance values had a large fluctuation (over ± 0.1 mH) under low frequencies. Until reaching 1000 Hz, the data was steady and repeatable. As a result, 1 kHz with a test signal of 1V was chosen. Under this testing condition, the variation of inductance for a single object was less than ± 0.01 mH.

Before testing the beams, several basic objects were tested and the results can be seen in Table 4-1. It can be seen that the air inductance tested by two LCR meters were slightly different. This might result from the differences between the testing machine and testing environment.

Table 4-1 Inductance data of basic objects (unit: mH).

Object	Inductance tested by	
	Agilent HP4284A	Tonghui TH2830
Air	18.44	17.33
Acrylic slab (100×150×H mm)	18.43	17.34
Wood testing table	18.45	17.38
0.5% vol. UHPFRC 10 mm thick slab	18.73	17.57
1% vol. UHPFRC 10 mm thick slab	18.95	17.75
2% vol. UHPFRC 10 mm thick slab	19.51	18.51
Steel (50×100×200 mm)	79.15	76.52

4.2.2 Effective depth test

In the previous research, the magnetic probe had not been applied on specimens with less than 25 mm thick. Since this method is going to be applied on thin member, a test aimed at determining the effective depth of the magnetic probe was proposed. Table 4-2 lists all the specimens used in this effective depth test.

Table 4-2 UHPFRC beams used for effective depth test.

Beam dimension (mm)	Mix design	Fibre vol. content	Vibration condition	Testing equipment
75×75×450	SD mix	2%	Yes	Agilent HP4284A
75×75×450	SD mix	2%	No	Agilent HP4284A
75×75×450	SD mix	3%	Yes	Agilent HP4284A
75×75×450	SD mix	3%	No	Agilent HP4284A
100×100×400	Pre-mix	1%	No	Tonghui TH2830
100×100×400	Pre-mix	2%	No	Tonghui TH2830

From Table 4-1, the inductance differences when placing the probe in air and on the acrylic slab are less than 0.01 mH. Therefore, the magnetic permeability of an acrylic slab can be generally considered the same as air and its effect on the result on the inductance of UHPFRC beam can be neglected. By placing 100×150 mm acrylic slabs (Figure 4-9a) with a different thickness between the specimens and the magnetic probe (Figure 4-9b), the inductances were measured.



Figure 4-9 Acrylic slabs used in the experiment (a) and experiment set up (b).

The acrylic slabs used in this experiment had thicknesses of 2, 4, 8, 12, 15, and 20 mm. By adding acrylic slab with different thickness, the inductance at a distance of 0, 2, 4, 8, 12, 15, 17, 20, 24, 28, 32, and 36 mm were measured at difference points of UHPFRC beams. The slab combination is listed in Table 4-3.

Table 4-3 Acrylic slab combination for effective depth test (unit: mm).

Targeting thickness	Slab combination
2	2
4	4
8	8
12	12
15	15
17	2+15
20	20
24	4+8+12
28	8+20
32	20+12
36	20+12+4

4.2.3 Inductive Test on UHPFRC beams

For the inductive test on $75 \times 75 \times 450$ mm beams, the magnetic probe was placed on the top and bottom surfaces of the beam. The inductance data from Points 1 to 4 was measured (Figure 4-10). The area between Points 1 to 4 was also the pure bending area in the four-point bending test (stated in Section 5.3). The Agilent HP4284A LCR meter was used in this test. The testing frequency was 50 Hz with a test signal of 100mV.

There were some drawbacks with the inductive test on the $75 \times 75 \times 450$ mm UHPFRC beams. One important reason was that the beam width (75 mm) is shorter than the probe length (93 mm). Therefore, it was impossible to test the beam in the two orthogonal directions to obtain the fibre orientation.

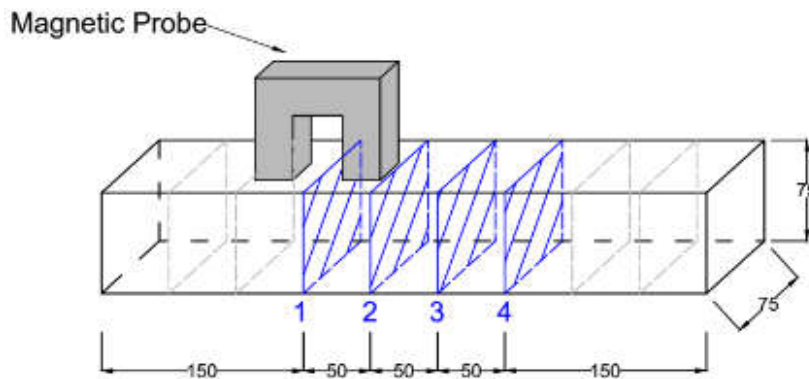


Figure 4-10 Horizontal testing on $75 \times 75 \times 450$ mm UHPFRC beams (unit: mm).

In order to solve this problem, the dimensions of the beam cast in later pre-mix batches were increased to $100 \times 100 \times 400$ mm. In order to gather more information, the concrete beam was divided into eight sections with seven cross section areas 1 to 7. Each section was $100 \times 100 \times 50$ mm. The pure bending area in the four-point bending test ranges from Points 3 to 5. The magnetic probe was placed at the centre of each section horizontally (Figure 4-11a) and vertically (Figure 4-11b) to measure the inductance. The Tonghui TH2830 LCR meter was used in this test. The testing frequency was 1 kHz with a test signal of 1 V.

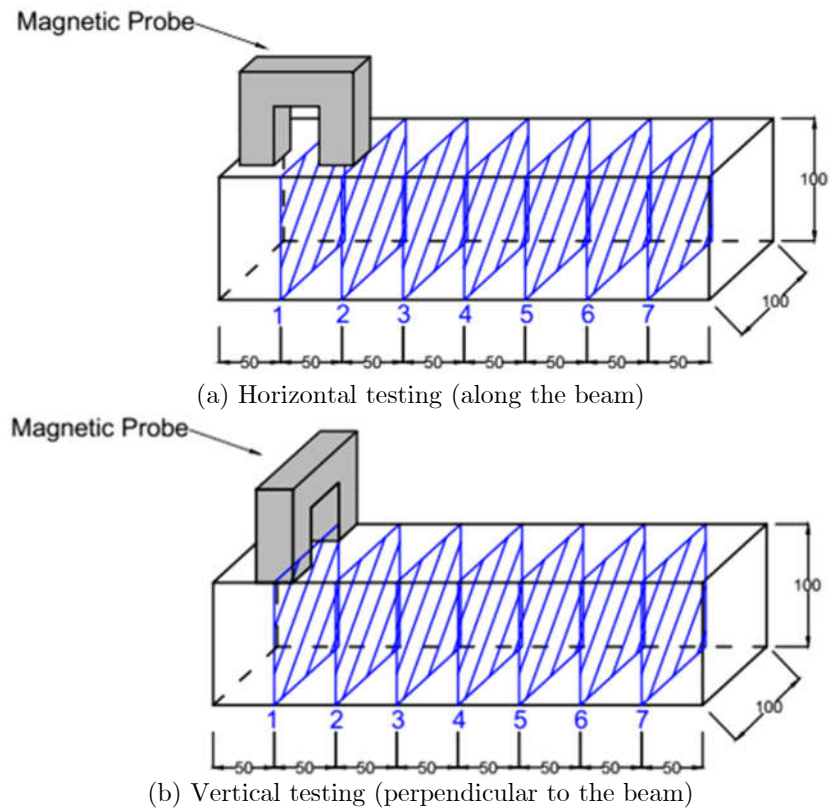


Figure 4-11 Horizontal (a) and vertical (b) testing method on UHPFRC beams (unit: mm).

4.2.4 Inductive Test on UHPFRC slabs

The initial purpose of conducting the four-point bending test was to keep a constant bending area and checked how different fibre orientations or spatial distributions affect the performance. However, the previous inductive test (Section 4.2.3) and further four-point bending tests had some limitations:

1. Inductance value obtained by vertical testing was always lower than the horizontal value due to the limitation of beam width;
2. Some beams failed in shear failure instead of flexural failure since the pure bending area is equal to the beam width (100 mm).

To improve the accuracy and reliability of the tests, a series of 500×500 mm UHPFRC slabs with thicknesses of 15 mm, 20 mm, 35 mm, and 50 mm were cast and tested using the magnetic probe (Figure 4-12a). By testing larger slabs, the inductance data influenced by the boundary condition was largely eliminated. This experiment was carried out on 1%, 2%, and 2.5% vol. UHPFRC slabs only since this test was meaningless on UHPC slabs. The Tonghui TH2830 LCR was used with a testing frequency of 1 kHz and test signal of 1V.

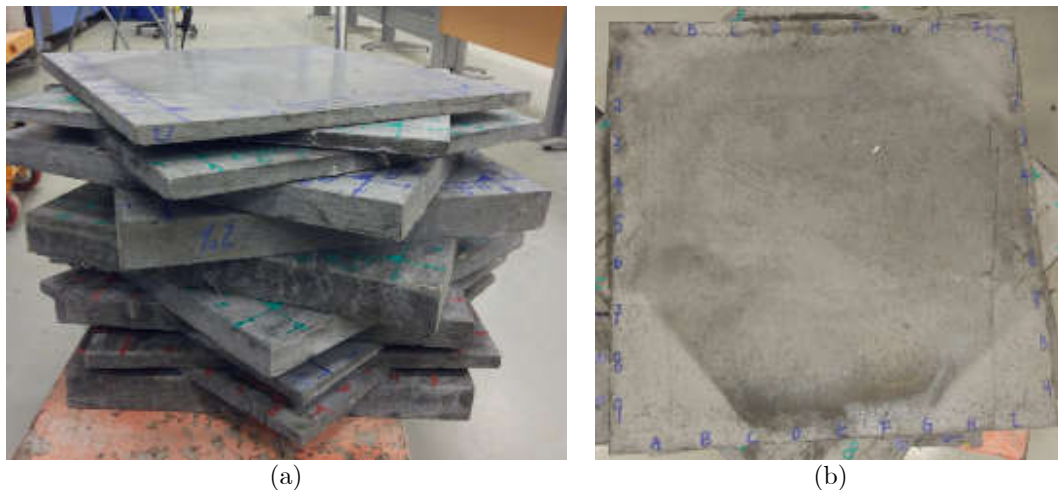


Figure 4-12 500×500×H UHPFRC slab used for inductive test.

The bottom surfaces during casting were used as the testing surface since they were smooth and flat. Since the length of the magnetic probe is 93 mm, the 500×500 mm slabs were labelled on a 9×9 grid from A1 to I9 at equal distances of 50 mm (Figure 4-13a). All

UHPFRC slabs were labelled from A to I and 1 to 9, as shown in Figure 4-12b. A paper testing map (Figure 4-13b) with 81 points highlighted in red was made to save the time of drawing all the gridlines on the concrete surface.

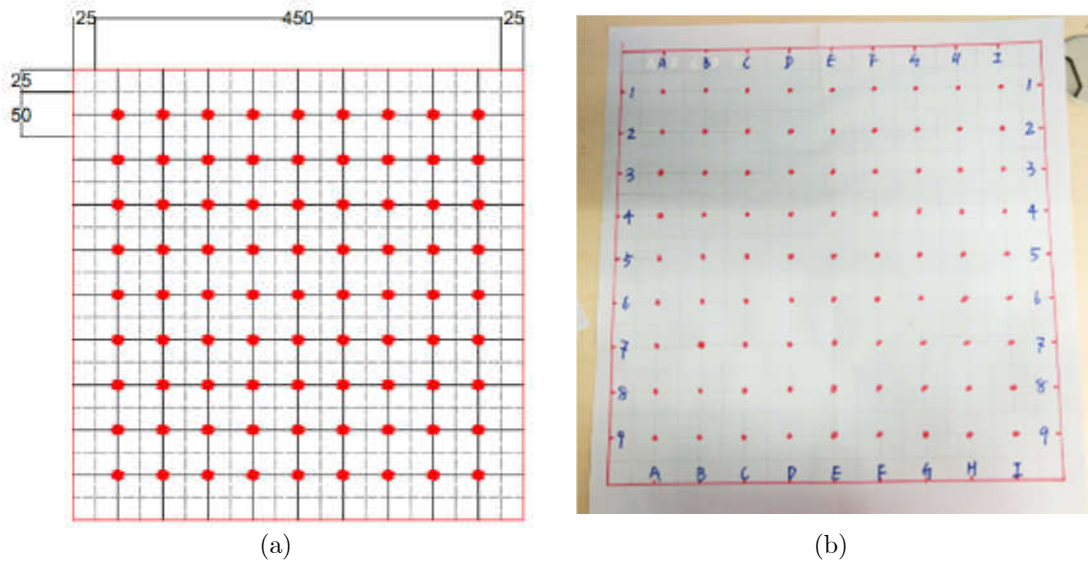


Figure 4-13 Testing area divisions of UHPFRC slab (unit: mm).

The paper testing map was placed on the slabs. By placing the magnetic probe in two orthogonal directions, the spatial distribution and orientation distribution at each red point can be measured. Figure 4-14 shows the horizontal and vertical testing directions.

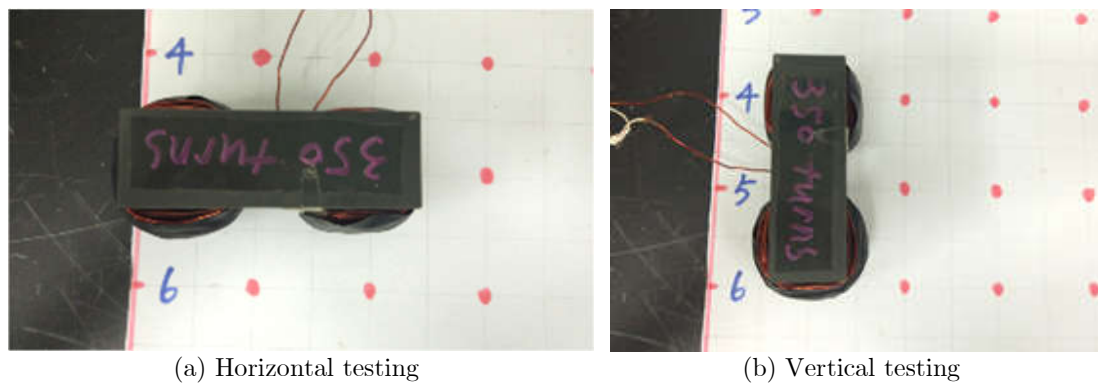


Figure 4-14 Horizontal (a) and vertical (b) testing directions.

4.3 Image Analysis Using Matlab

In order to verify the relationship between inductance and number of fibres, image analysis was carried out on the 75×75×450 mm and 100×100×400 mm UHPFRC beams after conducting four-point bending tests. As shown in Figure 4-15, beams were cut at the blue cross sections. If the concrete cracked at these particular points, the cutting point can be moved slightly towards either side to avoid a poor cross sectional graph.

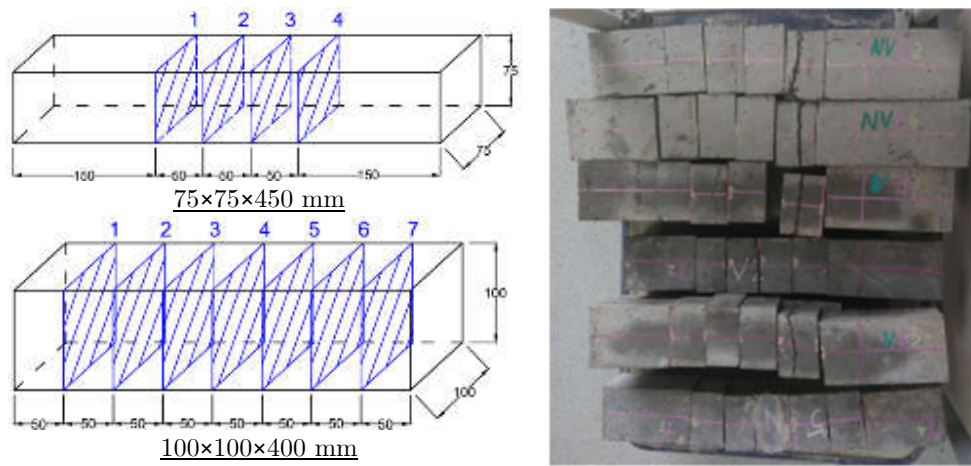


Figure 4-15 Cutting positions on UHPFRC beams.

Photos were taken with a Canon DS126231 camera and the number of steel fibres in each cross section was counted using the MATLAB program. The image analysis processing procedures are shown in Figure 4-16 where, from (a) to (e) are:

- (a) Original picture taken by camera;
- (b) Greyscale picture (using command 'rgb2gray');
- (c) Black-white picture by setting a certain threshold (using command 'im2bw');
- (d) Black-white picture after eliminating the noise (e.g., sand particles and air voids, etc.) (using command 'imerode' and 'bwareaopen');
- (e) Enlarged yellow area in the (d) with fibre locations marked with red points (using command 'bwlabel').

However, due to the limitation of the concrete cutter and the camera, the border of the steel fibres were stretched and vague. Thus, only the spatial distribution can be obtained.

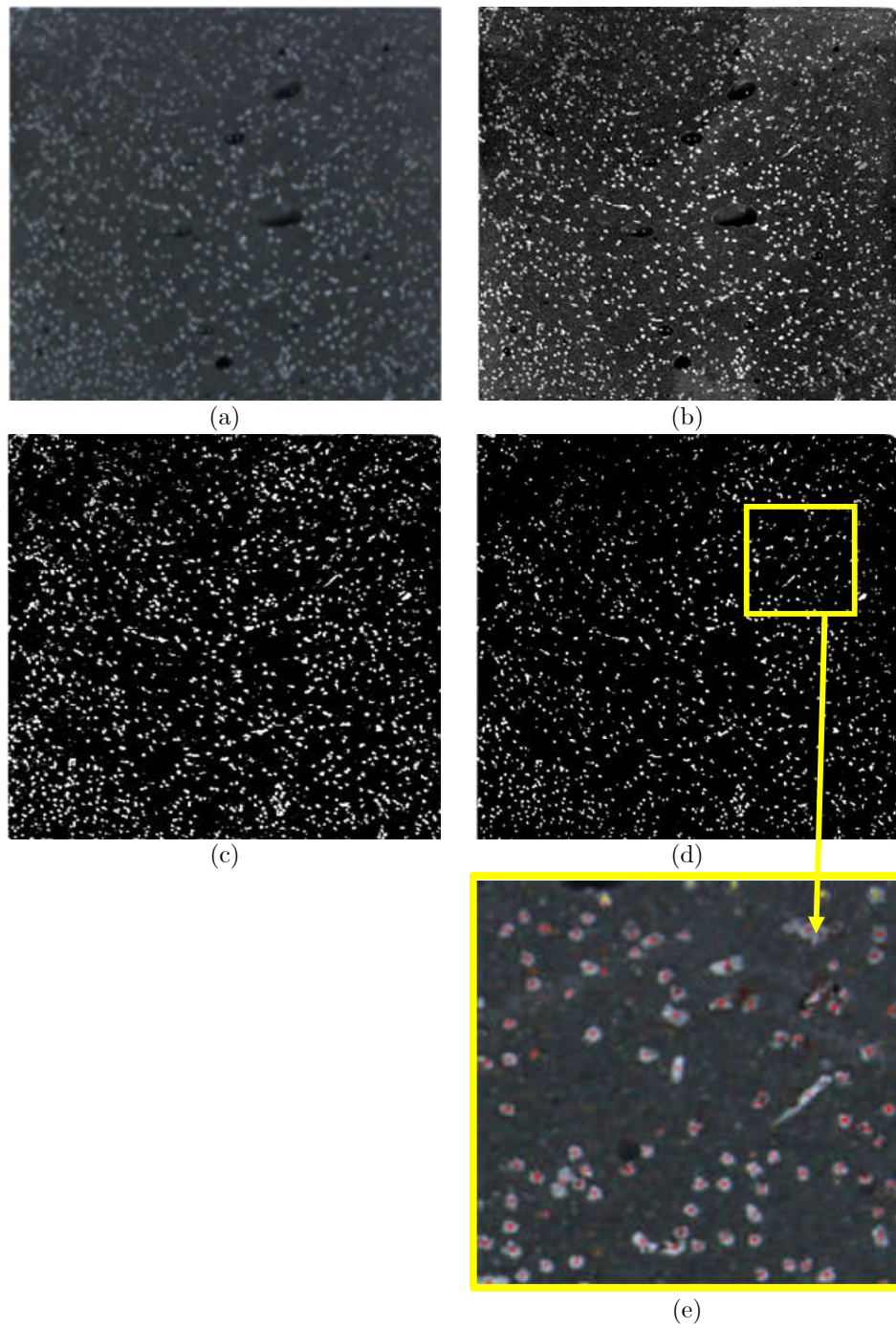


Figure 4-16 Image processing procedures.

CHAPTER 5 MECHANICAL TESTS METHOD

This chapter will introduce the compressive test, uniaxial tensile test, four-point bending test, and three point bending test conducted in this research. Testing specimens, testing machines, experimental setup, and experimental procedures will be presented.

5.1 Compressive Test

100×100×100 mm cube and 100 dia.×200 mm cylindrical specimens were used to obtain the compressive strength of UHPFRC. The compressive test followed the testing standard ‘GB/T 50081-20 02: Standard for test method of mechanical properties on ordinary concrete [91]’. This test was carried out on a 300 ton compressive test machine as can be seen in Figure 5-1a. Force control was used with a loading rate of 1 MPa/s.

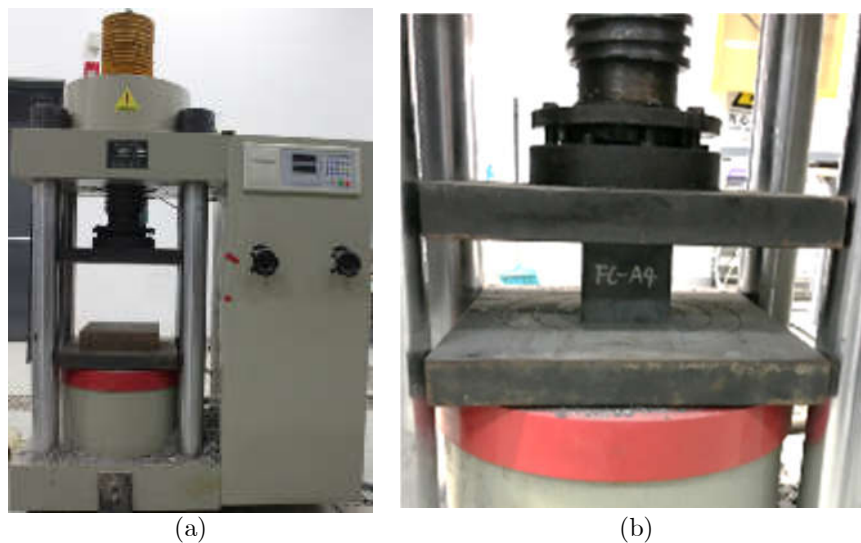


Figure 5-1 Compressive test setup.

For the cube specimens, two smooth and flat side surfaces were chosen as load faces. For the cylindrical specimens, the bottom surface were flat, but the top surface needed to be ground or cut. Although the UHPFRC specimens did not have any noticeable shrinkage effects, the actual dimensions of the specimens were still measured using slide callipers and recorded before the test. The measurements showed that the size reduction of 100

mm caused by shrinkage or specimen movement was less than 1 mm. The testing machine and testing setup can be seen in Figure 5-1b. The specimens were placed in the middle of the loading slab. The machine head was adjusted to almost touch before starting the test, then the load indicator was zeroed. All specimens were tested until they crushed.

The compressive strength can be calculated as:

$$f_c = \frac{F_c}{A} \quad \text{Equation 5-1}$$

where

- f_c compressive strength;
- F_c peak compressive load;
- A cross section area of the cube specimens.

For the UHPFRC cylinders, the compressive strength can be calculated as:

$$d = \frac{d_1 + d_2}{2} \quad \text{Equation 5-2}$$

$$f_c = \frac{4F_c}{\pi d^2} \quad \text{Equation 5-3}$$

where d_1 and d_2 are two diameters measured in orthogonal directions.

5.2 Uniaxial Tensile Test

Dog bone specimens were used for the uniaxial tensile test. The uniaxial tensile test was conducted on the DNS-300 (Figure 5-3a) and DNS-100 universal testing machines (UTM) produced by Changchun Research Institute for Mechanical Science Co. Ltd. There was no difference between these two testing machines apart from the loading capacities (30 ton and 10 ton).

It is difficult to have the same strain on each side of the specimen due to the addition of fibres. Hence, four strain gauges were attached to the centre of all four sides of the specimen. Strain data was collected and processed using LabVIEW. In the beginning, an extensometer was also used to obtain the mid-span deflection. However, the accuracy of

the extensometer was found to be not precise enough, so its use was not applied in the following experiment.

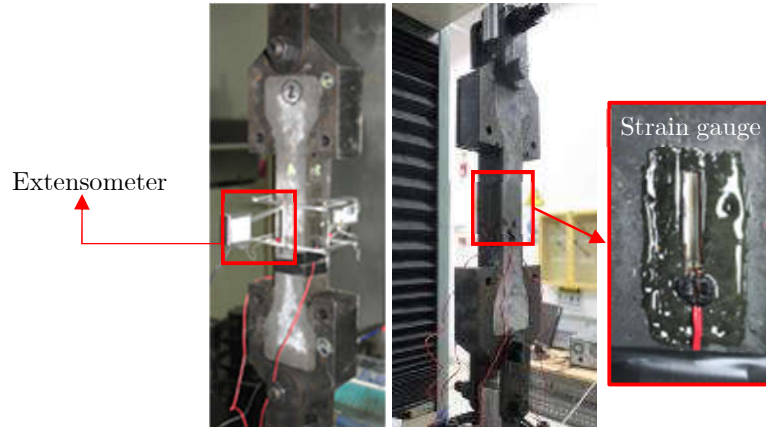


Figure 5-2 Uniaxial tensile test setup.

Since there is no universal uniaxial tensile testing standard, the recommendations from the Switzerland Standard ‘SIA 2052-2016’ was adopted [92]. The steel testing mould was connected to the testing machine by two steel slabs fixed by screws, as shown in Figure 5-3b. In order to make sure the stresses were consistent on each side and prevent any unbalanced load caused by rotation, the specimens were loaded to around 500 N at first. Then, all the strain data was checked. After checking, the specimens were unloaded to lower than 100 N and then the test was started. According to the standard, the loading rate (by deflection control) was controlled to be 0.1 mm/min before cracking and 0.3 mm/min after cracking. The test was stopped after the residual load was lower than 30% of the peak load.



Figure 5-3 DNS-300 UTM (a) and connection between steel mould and UTM (b).

The uniaxial tensile strength f_t can be calculated as:

$$f_t = \frac{F_t}{A} \quad \text{Equation 5-4}$$

where F_t represent the uniaxial tensile load and A represent the cross section area of the specimen. In this test, the cross section area is designed to be 50×50 mm.

5.3 Four-Point Bending Test on Thick Beams

Four-point bending tests were conducted on 75×75×450 mm and 100×100×400 mm beams aiming at finding the load-deflection diagram and peak tensile strength. The test was carried out on both the 30 ton and 10 ton UTMs. Following the test standard ‘GB/T 50081-20 02: Standard for test method of mechanical properties on ordinary concrete [91]’, the loading rate was set to be 0.3 mm/min. The experiment stopped when the residual load was lower than 50% of the peak load. Two deflection gauges were fixed on each side of the beam by the steel clamps to record the mid-span deflection (Figure 5-4). Deflection was calculated by taking the average of the two deflection gauges.

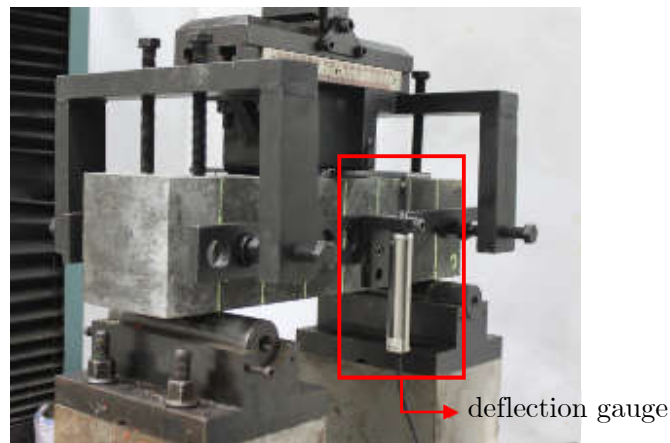


Figure 5-4 Four-point bending test setup on 100×100×400 mm beams.

The schematic diagram of the flexural test can be seen in Figure 5-5 and Figure 5-6.

For the 75×75×450 mm beams, it was not a standard flexural test setup. The effective span was 350 mm with a pure bending distance of 150 mm.

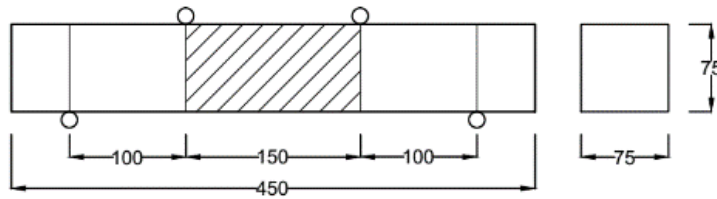


Figure 5-5 Schematic graph of the bending test on self-developed UHPFRC beams (unit: mm).

For the standard 100×100×400 mm beams, the effective span was 300 mm with a pure bending distance of 100 mm.

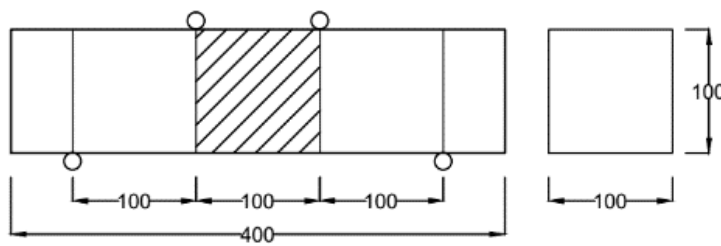


Figure 5-6 Schematic graph of the bending test on pre-mix UHPFRC beams (unit: mm).

The flexural strength f_f can be calculated using Equation 5-5 to Equation 5-7,

$$M = \frac{F_f \times L_s}{2} \quad \text{Equation 5-5}$$

$$W = \frac{BH^2}{6} \quad \text{Equation 5-6}$$

$$f_f = \frac{M}{W} \quad \text{Equation 5-7}$$

where

F_f peak flexural load;

L_s distance between support and the nearby loading point (100 mm in standard and non-standard cases);

M external moment;

W section modulus;

B width of the beam cross section;

H height of the beam cross section;

f_f flexural strength.

5.4 Three-Point Bending Test on Thin Beams

Three-point bending tests was carried out on the 500×500×15 mm, 500×500×20 mm, 500×500×35 mm, and 500×500×50 mm slabs. Due to the size limitation of the cutter in the university lab, all slabs were sent to the Tianhe Building Material Processing Company and cut by a water blade (Figure 5-7a) into four pieces. Each piece had a dimension of 250×250×H mm (Figure 5-7b).



Figure 5-7 Concrete slabs cut by water blade.

All 250×250×H specimens were further divided into four thin beams. The division pattern can be seen in Figure 5-8. Each thin beam was 200×50 mm with different thicknesses. They were labelled from 1 to 16, so the mechanical test results can be compared with the inductive test results in the later study. It should be noted that only specimen numbers 1 to 8 were tested in this research. The red points in Figure 5-8 were the testing points in the inductive test.

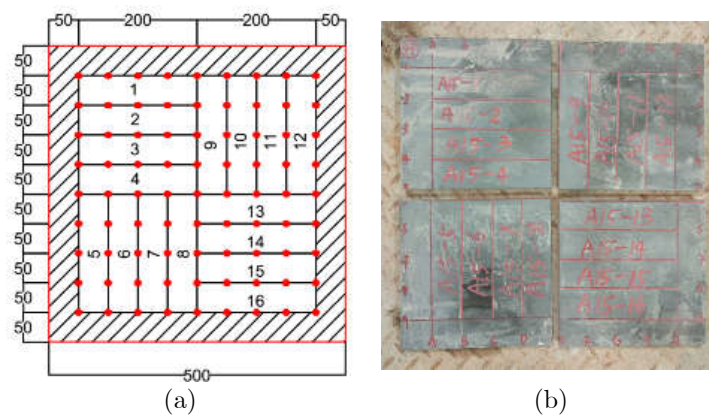


Figure 5-8 Cutting division of concrete slab.

Taking a 15 mm thick beam as an example, the three-point bending test setup can be seen in the following figure. The effective span is 150 mm.

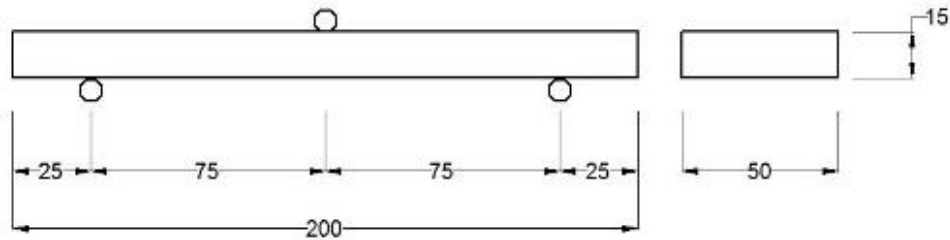


Figure 5-9 Three-point bending test for UHPFRC beam.

The flexural strength for a three-point bending test can be calculated from Equation 5-8 to Equation 5-10. L also represents the distance between two supports. All the other abbreviations have the same meaning as the four-point bending test.

$$M = \frac{F_f \times L}{4} \quad \text{Equation 5-8}$$

$$W = \frac{BH^2}{6} \quad \text{Equation 5-9}$$

$$f_f = \frac{M}{W} \quad \text{Equation 5-10}$$

The experiment was carried out on a 3 ton UTM machine at a constant loading speed of 0.3 mm/min. Figure 5-10 shows the testing setup. The experiment stopped when the load dropped below 50% of the peak load. The displacement movement from the machine is used to plot the load-displacement diagram later.



Figure 5-10 Three-point bending test setup on a 200×50×20 mm UHPFRC beam.

CHAPTER 6 FIBRE DISTRIBUTION TEST RESULTS

This chapter shows the test results obtained from cylindrical permanent magnetic test and C-shape magnetic probe inductive test. Due to the limitation of cylindrical permanent magnet test, this test method is not further investigated. For the C-shape magnetic probe test, the effective depth of the probe is examined, followed by the detailed fibre volume content distribution and fibre orientation angle distribution analysis. The verification of magnetic probe test results using image analysis method is also presented.

6.1 Cylindrical Permanent Magnet Test Results

These results are based on the cylindrical permanent magnet test described in Section 4.1. Figure 6-1 shows the signal voltages obtained from the experiments on 0.5%, 1%, and 2% fibre volume UHPFRC slabs. The voltage has a linear relationship with the attracting force. However, due to an operation mistake, the conversion formula between voltage and attracting force was missing. Therefore, only the general distribution trend can be drawn. The colour contours from blue to red represent the increasing voltage between the cylindrical permanent magnet and UHPFRC slabs. The colour bar on the right shows the force range. The spatial distributions can be viewed clearly on each slab.

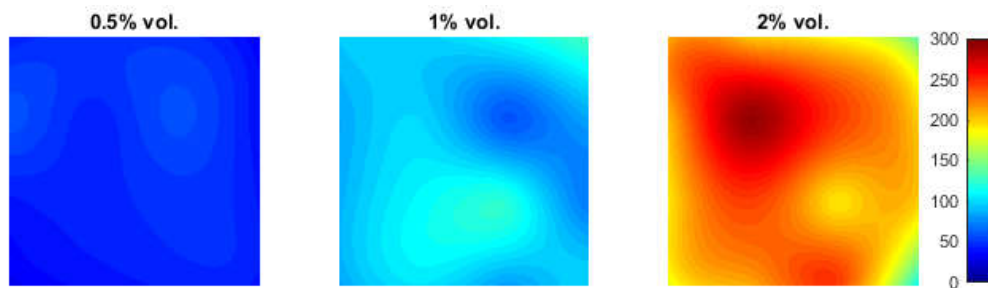


Figure 6-1 Contour graph of fibre volume content of 0.5%, 1%, and 2% vol. UHPFRC slabs (unit: mV).

Table 6-1 shows the exact values from each slab. It can be seen that with the increase of fibre volume content, the attracting force increases in proportion. This result can be

correlated with Equation 4-5 in Section 4.1.1, the attracting force F_m is in a linear relationship with fibre volume content V_f . The coefficient of variation (COV) is calculated by ‘standard deviation/ mean’. It is a standardized measurement of the dispersion of a probability distribution. It can be seen from the COV, the spatial distribution of fibres tends to be more non-uniform with the increase of fibre volume content.

Table 6-1 Signal voltage obtained from experiment.

Slab number	Signal voltage (mV)		Coefficient of variation
	Mean	Standard deviation	
0.5% vol. UHPFRC	43.7	7.7	0.18
1% vol. UHPFRC	94.6	18.0	0.19
2% vol. UHPFRC	201.7	42.8	0.21

Based on the results of the experimental work, there are some limitations of this method. One is that the attracting force data seriously fluctuates during testing, so every location needs to be tested more than five times to avoid any mistakes. Another one is that fibre orientation distribution cannot be obtained. Despite these limitations, the test can still be used in the construction field as a quality control test method with a more stable FSR. For the laboratory research in this study, fibre orientation is also a critical part. As a result, this method was not further investigated in any depth.

6.2 Inductive Test Results for Determining Effective Depth

The effective depth testing was conducted on SD 2%, 3%, Pre-mix 2.5%, and 5% vol. UHPFRC beams. In total, 8 points (2 points for each group) were tested. The relative magnetic permeability (RMP) μ can be calculated as:

$$\mu = \frac{L_0}{L_{air}} \tag{Equation 6-1}$$

where

- L_0 magnetic inductance obtained by the LCR meter directly on the specimen;
- L_{air} magnetic inductance when placing the magnetic probe in the air and far from any conductive object.

Table 6-2 shows all the average relative permeabilities obtained for different fibre volume contents with different testing distance t .

Table 6-2 Average relative magnetic permeabilities obtained for each group.

t (mm)	Attenuation factor			
	SD 2% vol.	SD 3% vol.	Pre-mix 2.5% vol.	Pre-mix 5% vol.
0	1.074	1.129	1.083	1.170
2	1.054	1.092	1.064	1.125
4	1.041	1.070	1.049	1.106
8	1.029	1.048	1.034	1.065
12	1.017	1.030	1.023	1.043
15	1.014	1.023	1.018	1.033
17	1.011	1.020	1.015	1.028
20	1.009	1.016	1.012	1.021
24	1.005	1.010	1.009	1.017
32	1.002	1.005	1.005	1.009
36	1.002	1.003	1.003	1.007

It can be seen from Table 6-2, the relative magnetic permeability decreased with the increase of slab thickness. However, since the initial relative magnetic permeability for each group is different, it is difficult to reflect on how the relative magnetic permeability decays with the increase of thickness. Thus, an attenuation factor (AF) is introduced to describe the residual proportion of magnetic permeability. It can be calculated as:

$$AF_t = \frac{\mu_t - 1}{\mu_0 - 1} \times 100\% \quad \text{Equation 6-2}$$

where

μ_t magnetic permeability at thickness t ;

μ_0 magnetic permeability when placing the probe directly on the specimen.

Based on Equation 6-2, AF for each group can be calculated and the results are shown in Table 6-3. For specimens with lower fibre content, the relative magnetic permeability tends to drop quicker. All groups of AF data drop below 10% for depths greater than 24 mm. This proves that the fibres 24 mm away from the testing surface have little effect on the relative magnetic permeability.

Table 6-3 Average attenuation factors calculated for each group.

t (mm)	Attenuation factor			
	SD 2% vol.	SD 3% vol.	Pre-mix 2.5% vol.	Pre-mix 5% vol.
0	100%	100%	100%	100%
2	73%	72%	76%	74%
4	55%	54%	59%	62%
8	39%	37%	41%	38%
12	23%	23%	27%	25%
15	19%	18%	21%	20%
17	15%	15%	18%	16%
20	12%	13%	15%	13%
24	6%	8%	10%	10%
32	3%	4%	6%	5%
36	3%	3%	4%	4%

The attenuation trend can be seen in Figure 6-2. It can be seen that the attenuation factor has a very similar exponential trend for all groups of data. It proves that the fibres closer to the testing surface has a more significant effect on the relative magnetic permeability, especially within 6 mm of the testing surface since after this the attenuation factor drops below 50%.

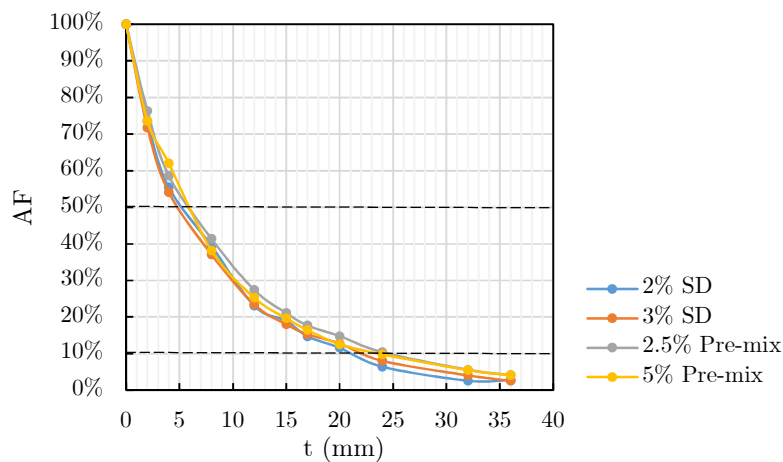


Figure 6-2 Average attenuation factor at different depth for each group.

To get a theoretical expression of this relationship, a curve fitting analysis was conducted using MATLAB. The relationship between the testing depth and attenuation factor can be calculated to be expressed by Equation 6-3 with an R-squared value equal to 0.995. The R-squared value reflects the goodness of fit. The closer to one, the better it fits the data.

$$AF = e^{-0.115t}$$

Equation 6-3

The comparison between the experimental value and theoretical value calculated from Equation 6-3 can be seen in Figure 6-3. This test reveals the effective depth when using this particular probe. If any thin specimens are going to be tested in future, AF can be used for correction purposes to get the real fibre volume content value.

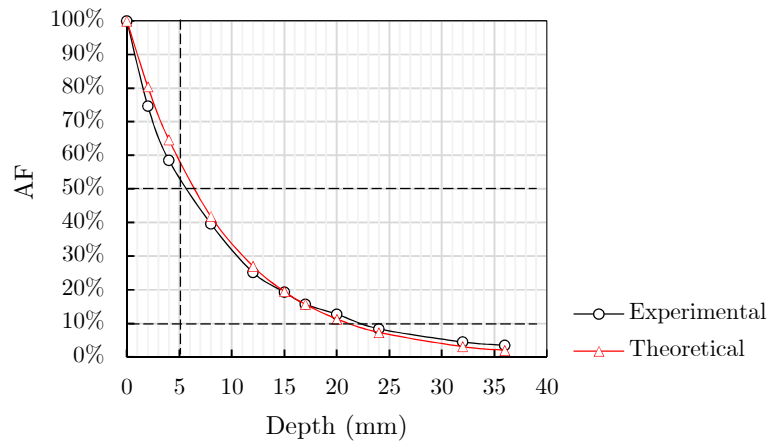


Figure 6-3 Comparison between experimental and theoretical attenuation factor at different depth.

6.3 Image Analysis Results

6.3.1 Layer analysis

The depth is equal to 20 mm when AF drops below 10% using Equation 6-3. In order to verify the equation and reliability of the testing accuracy, image analysis was conducted on 2%, 2.5%, 3%, and 5% vol. UHPFRC beams cross sections. Since the total number of fibres were too big for 5% vol. UHPFRC, many fibres were stuck to each other during cutting, as can be seen in Figure 6-4b. The number of fibres counted using MATLAB was very inaccurate. Therefore, the image analysis results of 5% vol. UHPFRC beams are not included here.

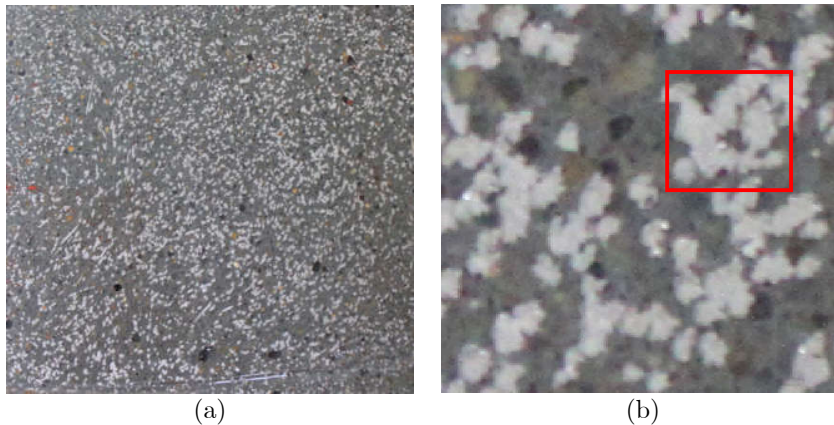


Figure 6-4 Original (a) and enlarged (b) images taken from a 5% vol. UHPFRC cross section.

Layer analysis was carried out by counting the number of fibres in different layers, as can be seen in Figure 6-5. 32 cross sections (75×75 mm) of 2% vol. UHPFRC were analysed by layer analysis. The numbers of fibres 75, 50, 20, and 15 mm away from the bottom surface were counted.

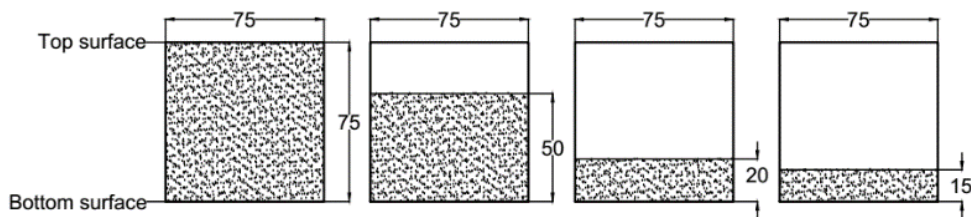


Figure 6-5 Number of fibres in different regions in layer analysis (unit: mm).

Figure 6-6 shows the relationship between the numbers of fibres and inductance and the equations for each trend line. It can be seen that the 20 mm group has the best correlation with an R-squared value of 0.5883. This proves the reliability of the previous effective depth that the fibres outside 20 mm regions do not have a significant effect on the final relative magmatic permeability value.

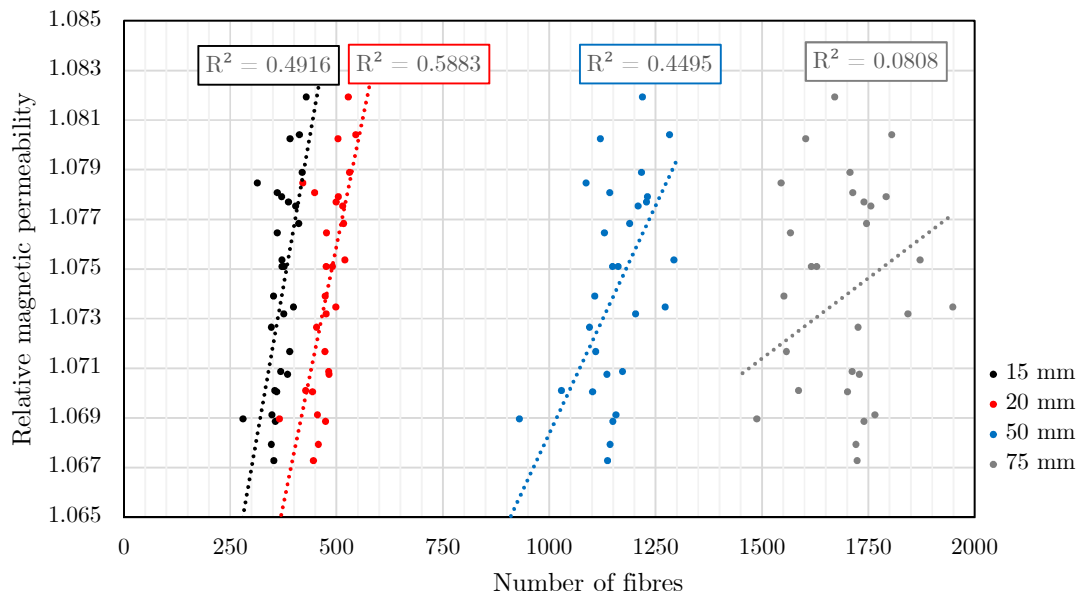


Figure 6-6 Relationship between relative magnetic permeability and number of fibres of 2% vol. UHPFRC within different regions.

Based on layer analysis, the number of fibres in the bottom 20×75 mm regions for 2% and 3% vol. were counted. The cross section is 100×100 mm for 2.5% vol. UHPFRC beams. In order to be consistent with the other two groups, the number of fibres in the middle 75 mm region is used, as shown in Figure 6-7.

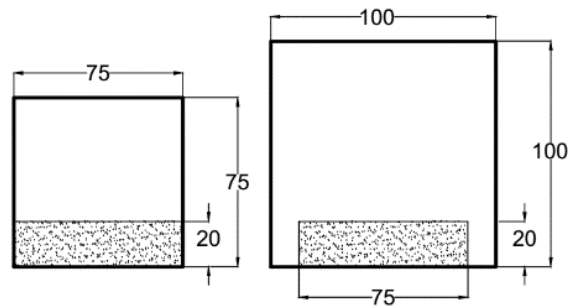


Figure 6-7 Areas of number of fibres counted for 75×75 mm and 100×100 mm cross sections (unit: mm).

To sum up, 62, 52, and 48 points were collected from 2%, 2.5%, and 3% vol. UHPFRC beams. They are labelled as black, blue, and red dots in Figure 6-8. For a 75×20 mm region, there is a linear relationship between the number of fibres and relative magnetic permeability. The linear regression line has an R-squared value of 0.581.

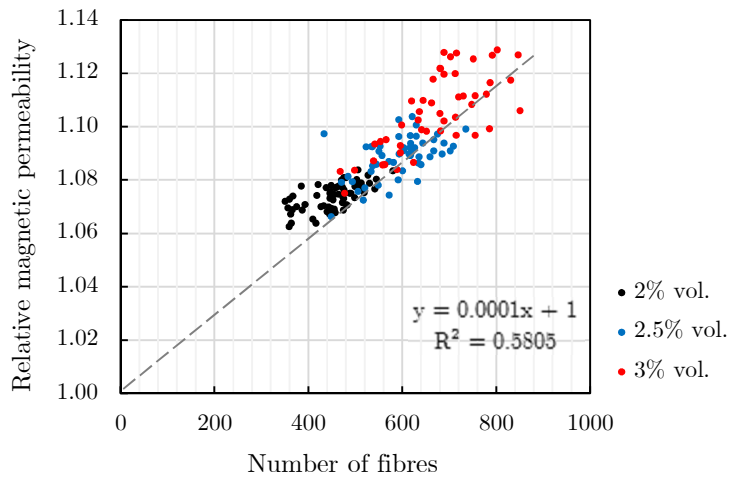


Figure 6-8 Relationship between relative magnetic permeability and number of fibres in 75×20 mm region.

Some points in the image analysis results (Figure 6-6 and Figure 6-8) drift off from the regression line and results have an R-squared value of 0.588, which is not considered very high in statistics. Many factors influence the accuracy:

1. Due to the limitation of the testing specimen (75mm), only the inductance along the beam was obtained;
2. The inductance generally reflects the fibre distribution in the whole testing area rather than just the cross section;
3. Even for UHPFRC with a fibre volume content less than 5%, some fibres were still stuck to each other, therefore, affecting the total number of fibres.

6.3.2 Fibre segregation effect due to external vibration

As mentioned in Section 3.4, some 75×75×500 mm beams were vibrated during casting to manually create a different fibre distribution. From the previous section, only the fibres within 20 mm of the surface can be detected. Therefore, the fibres within the upper 20 mm and bottom 20 mm regions were counted (Figure 6-9).

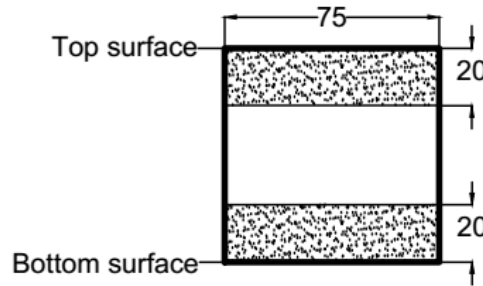


Figure 6-9 Number of fibres counted in the top and bottom 20 mm region (unit: mm).

Magnetic inductive tests and image analysis were also conducted on the 2% and 3% vol. vibrated and non-vibrated beams where each group has three specimens with four cross sections. The segregation ratio is calculated by:

$$\text{Segregation ratio} = \frac{\text{Number of fibres in bottom 20 mm region}}{\text{Number of fibres in top 20 mm region}} \quad \text{Equation 6-4}$$

Table 6-4 describes the differences of relative magnetic permeability and fibre amount differences for vibrated and non-vibrated prisms. It can be seen that there is no noticeable segregation if no vibration is applied, and the segregation ratio are closer to 1. On the other hand, the vibrated prisms shows a significant difference. More fibres tend to settle to the bottom of the beams and results in a larger number of fibres and RMP value.

Table 6-4 Differences between vibrated and non-vibrated 2% and 3% vol. UHPFRC beams.

Specimen number	RMP	Number of fibres	Segregation ratio
2% vol. Non-vibrated top	1.077	458	0.993
2% vol. Non-vibrated bottom	1.071	455	
2% vol. Vibrated top	1.071	404	1.225
2% vol. Vibrated bottom	1.077	495	
3% vol. Non-vibrated top	1.096	640	1.078
3% vol. Non-vibrated bottom	1.112	690	
3% vol. Vibrated top	1.085	612	1.209
3% vol. Vibrated bottom	1.122	740	

6.4 Inductive Test Results for UHPFRC Slabs

6.4.1 Fibre volume content distribution results

As stated in Section 4.2.4, the inductance at each specific point was measured in two perpendicular directions. In Figure 6-10, the magnetic inductances of the red points were read directly from the LCR meter. In total, 81 data points were collected for each slab.

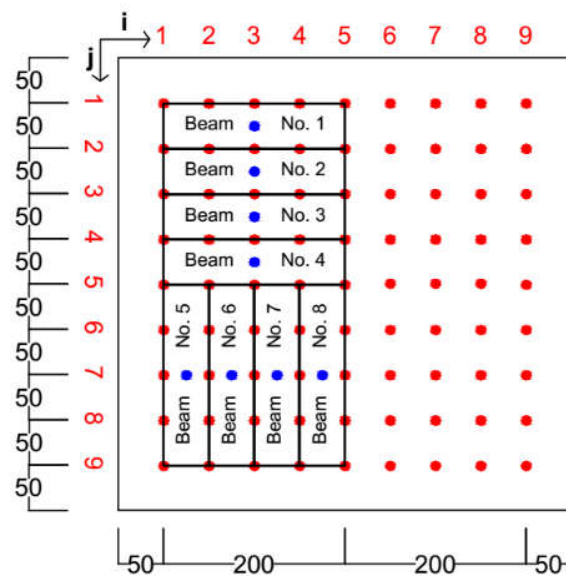


Figure 6-10 Three different groups of data calculated in the research (unit: mm).

Air inductance is labelled as L_{air} . The magnetic inductance values measured in the horizontal and vertical directions are labelled as L_x and L_y . All the magnetic inductance values were divided by the air inductance to get the relative magnetic permeability, which are labelled as μ_x and μ_y .

The average of relative magnetic permeability measured in two orthogonal directions is the indication of fibre volume content. Based on Equation 2-25, the average relative magnetic permeability on each red point can be calculated as Equation 6-5. Symbols i and j are used to represent the point location, e.g. $\mu_{11,x}$ represents the horizontally measured relative magnetic permeability at the point on top left corner.

$$\mu_{ij,ave} = \frac{\mu_{ij,x} + \mu_{ij,y}}{2} \quad \text{Equation 6-5}$$

To correlate the result between fibre distribution test and mechanical test for each beam, the relative inductance values of the blue points in Figure 6-10 are also needed. The value is derived from the nearby two red points. For the blue points of beam 1 to 4, the average relative magnetic permeability can be expressed as:

$$\mu_{ij,ave} = \frac{\mu_{ij,x} + \mu_{ij,y} + \mu_{i(j+1),x} + \mu_{i(j+1),y}}{4} \quad \text{Equation 6-6}$$

For beam 5 to 8, it can be calculated by:

$$\mu_{ij,ave} = \frac{\mu_{ij,x} + \mu_{ij,y} + \mu_{(i+1)j,x} + \mu_{(i+1)j,y}}{4} \quad \text{Equation 6-7}$$

Detailed mean, standard deviation, and coefficient of variance of relative magnetic permeabilities for all slabs can be seen in Table 6-5. It can be seen that with the increase of fibre content, the relative magnetic permeability also increases. It also increases with the increase of slab thickness from 15 to 35 mm. Since the magnetic probe has limited testing depth, there is no obvious difference between thicknesses 35 and 50 mm.

Table 6-5 Mean, STD, and COF of relative magnetic permeabilities of all slabs.

		15 mm	20 mm	35 mm	50 mm
Mean	1% vol.	1.031	1.035	1.038	1.043
	2% vol.	1.059	1.060	1.074	1.075
	2.5% vol.	1.069	1.078	1.095	1.088
Standard deviation	1%	0.0004	0.0005	0.0002	0.0005
	2%	0.0005	0.0006	0.0006	0.0012
	2.5%	0.0016	0.0009	0.0008	0.0017
Coefficient of variance	1% vol.	0.039%	0.048%	0.019%	0.048%
	2% vol.	0.047%	0.057%	0.056%	0.112%
	2.5% vol.	0.150%	0.084%	0.073%	0.156%

Combining the results from Table 6-5 and the results from Nunes [88], a relationship between the theoretical relative magnetic permeability μ can be derived as shown in Figure 6-11. When fibre volume content is 0, the relative magnetic permeability value equals to 1, which represents the magnetic permeability of air. The R-squared value of 0.9987 shows a near perfect linear fitting.

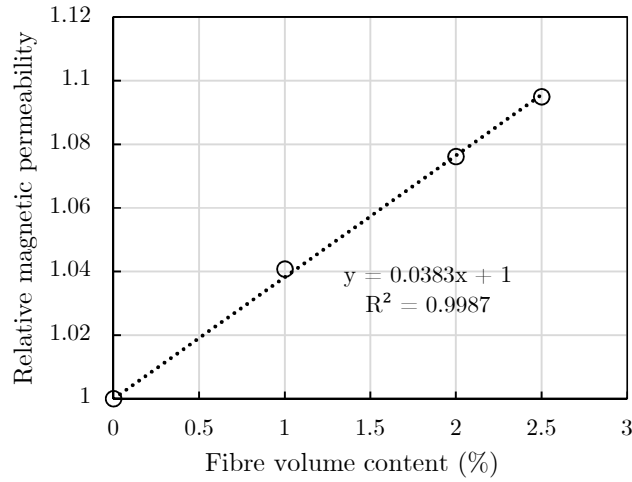


Figure 6-11 Relationship between fibre volume content and relative magnetic permeability.

Considering the effective depth of the magnetic probe, if relative magnetic permeability μ_{test} is obtained on a thin specimen, the attenuation factor should be applied to calculate the real fibre volume content. The relationship between relative magnetic permeability μ and fibre volume content V_f is further developed into

$$\mu_{cal} = \frac{\mu_{test} - 1}{1 - AF_t} + 1 \quad \text{Equation 6-8}$$

$$\mu_{cal} = 0.0383 \cdot V_f + 1 \quad \text{Equation 6-9}$$

where AF_t represent the attenuation factor when the specimen's thickness is t . Combining Equation 6-8 and Equation 6-9, the corrected relationship is

$$V_f = \frac{\mu_{test} - 1}{0.0383 \cdot (1 - AF_t)} \quad \text{Equation 6-10}$$

By using Equation 6-10, fibre volume content can be derived and is shown in Table 6-6. For all the 1% vol. slabs, the fibre content fulfils the designed requirement. For 2% and 2.5% vol., some slabs have a lower fibre volume content than the designed value.

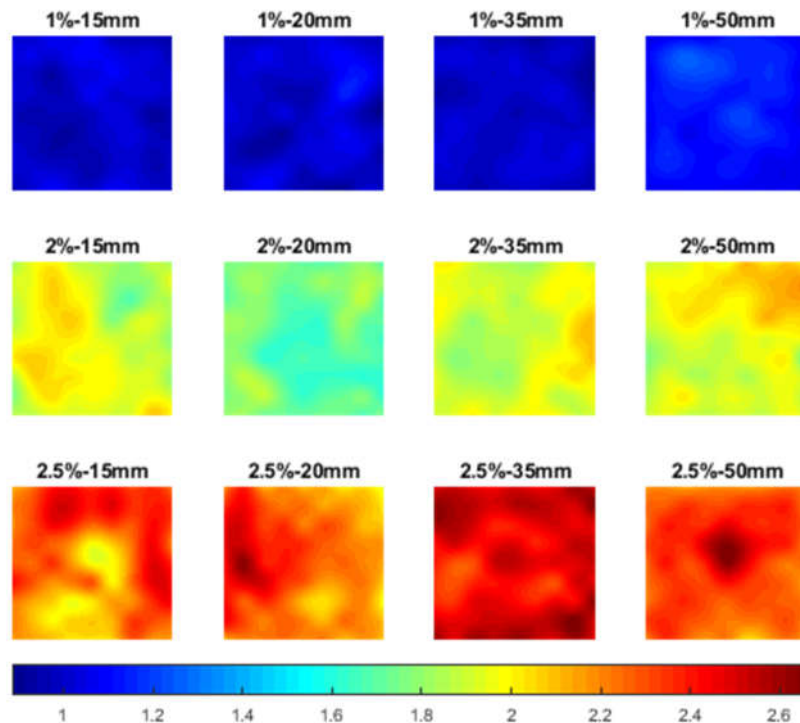
With the increase of fibre volume content, the standard deviation also increases, which reveals that fibre tends to distribution more non-uniformly. This effect is more severe with the 2.5% vol. UHPFRC slabs. A possible reason includes the fibre balling effect or fibre gathering effect due to inferior workability. Although there are some fibre volume

content differences within each slab, the differences are very small compared to the total fibre volume content. Therefore, the slabs can be considered almost uniformly spatially distributed.

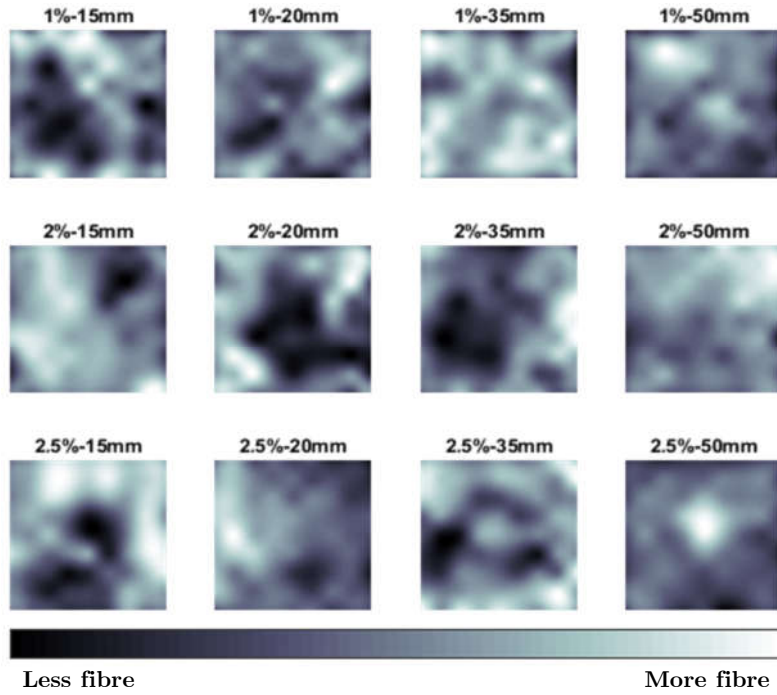
Table 6-6 Mean and STD of fibre volume content of all slabs.

		15 mm	20 mm	35 mm	50 mm
Mean	1% vol.	1.0%	1.0%	1.0%	1.1%
	2% vol.	1.9%	1.7%	1.9%	2.0%
	2.5% vol.	2.2%	2.2%	2.5%	2.3%
Standard deviation	1%	0.013%	0.016%	0.006%	0.014%
	2%	0.018%	0.018%	0.016%	0.030%
	2.5%	0.052%	0.026%	0.020%	0.045%

The first coloured contour plot in Figure 6-12a describes the fibre distribution of all slabs at a unified scale. Colours ranging from blue to red represent the differences of fibre volume content. It can be seen directly that slabs 2%-20 mm and 2.5%-15 mm have a lower fibre volume content than the designed fibre volume content. Since the range of data is too wide in the coloured contour plots, and the detailed fibre distribution cannot be visualized. Thus, a greyscale contour plot is given as Figure 6-12b.



(a) with a scale as fibre volume content in percentage



(b) with a general non-unified scale

Figure 6-12 Fibre volume content distribution of all slabs.

6.4.2 Fibre orientation distribution results

Based on previous literature by Nunes [88], the fibre orientation was expressed by an orientation indicator ρ_{Δ} . The orientation indicator of the red points can be calculated as:

$$\rho_{\Delta} = \frac{\mu_{ij,y} - \mu_{ij,x}}{2(\mu_{ij,ave} - 1)} \quad \text{Equation 6-11}$$

For the blue points, the orientation indicator can be derived from the nearby two red points. For the blue points on beam 1 to 4, the orientation indicator ρ_{Δ} can be derived as:

$$\rho_{\Delta} = \frac{\mu_{ij,y} + \mu_{i(j+1),y} - \mu_{ij,x} - \mu_{i(j+1),x}}{\mu_{ij,y} + \mu_{i(j+1),y} + \mu_{ij,x} + \mu_{i(j+1),x} - 4} \quad \text{Equation 6-12}$$

For the blue points on beam 5 to 8, the equation is:

$$\rho_{\Delta} = \frac{\mu_{ij,y} + \mu_{(i+1)j,y} - \mu_{ij,x} - \mu_{(i+1)j,x}}{\mu_{ij,y} + \mu_{(i+1)j,y} + \mu_{ij,x} + \mu_{(i+1)j,x} - 4} \quad \text{Equation 6-13}$$

Nunes *et al.* (2016) found the orientation indicator has a sinusoidal relationship with the fibre orientation angle, but an analytical expression between fibre orientation angle and orientation indicator ρ_{Δ} was not presented. Through further derivation, it is found that the orientation indicator is a function of polynomial terms of $\cos(\varphi)$ For example, the full expression of orientation indicator 1% vol. UHPFRC in terms of orientation angle φ according to Nunes *et al.* (2016) can be expressed as:

$$\rho_{\Delta,1\%} = \frac{-1076.68 \cos^6(\varphi) + 1615.03 \cos^4(\varphi) + 4.03 \times 10^7 \cos^2(\varphi) - 2.02 \times 10^7}{-0.96 \cos^6(\varphi) + 5.68 \times 10^5 \cos^4(\varphi) - 5.68 \times 10^5 \cos^2(\varphi) - 6.41 \times 10^7 + 0.48 \cos^2(\varphi)}$$

Equation 6-14

After numerical analysis, only the constant terms and the $\cos^2(\varphi)$ term on the numerator are found to be critical to the value of fibre orientation indicator ρ_{Δ} . Therefore, Equation 6-14 can be further simplified to:

$$\rho_{\Delta,1\%} \approx -0.63 \cos^2(\varphi) + 0.315 = 0.315 \cos(2\varphi)$$

Equation 6-15

Figure 6-13 shows the comparison between the original fibre orientation indicator calculated using Equation 6-14 and the simplified orientation indicator calculated using Equation 6-15. No obvious difference can be observed from 0-90°. Therefore, the original equation can be replaced with the simplified equation. There also works with other fibre volume percentage.

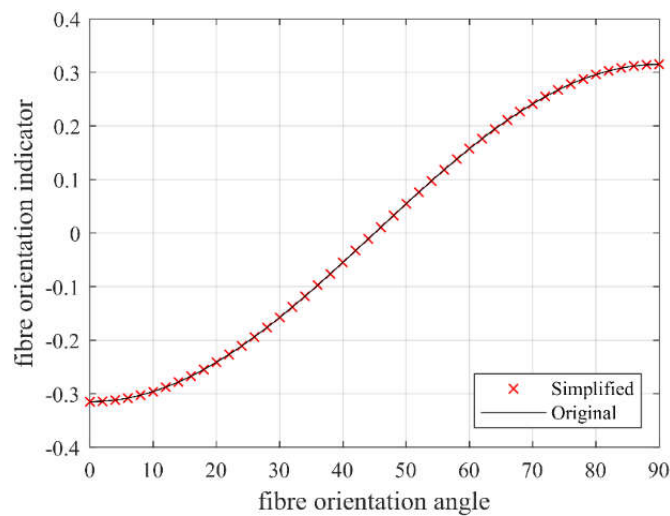


Figure 6-13 Relationship between fibre orientation angle and fibre orientation indicator.

The relationship for other fibre percentage can also be derived as:

$$\rho_{\Delta,2\%} \approx -0.299 \cos(2\varphi) \quad \text{Equation 6-16}$$

$$\rho_{\Delta,3\%} \approx -0.297 \cos(2\varphi) \quad \text{Equation 6-17}$$

$$\rho_{\Delta,4\%} \approx -0.282 \cos(2\varphi) \quad \text{Equation 6-18}$$

This relationship was drawn in Figure 6-14. It can be seen that the fibre volume content does not have a significant effect on the fibre orientation indicator, especially when the fibre orientation angle is around 45°.

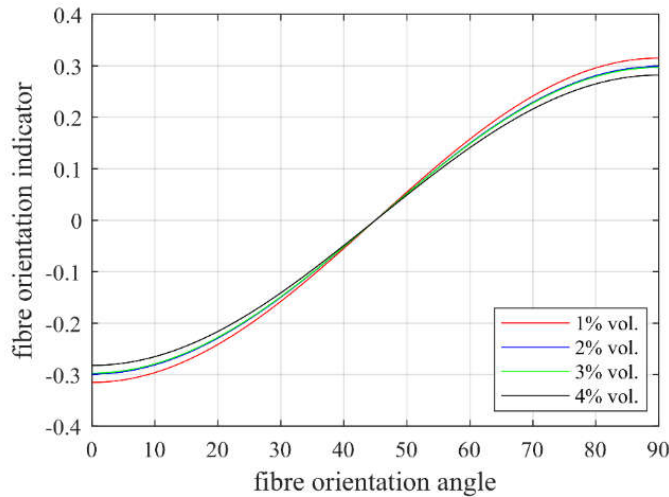


Figure 6-14 Relationship between fibre orientation angle and fibre orientation indicator at different fibre volume content.

Generally, the fibre orientation indicator can be expressed as:

$$\rho_{\Delta} = \lambda \cos(2\varphi) \quad \text{Equation 6-19}$$

where the fibre orientation indicator coefficient λ slightly ranges around -0.3 depending on the fibre volume content.

By using Equation 6-19, the fibre orientation distributions can be characterized. Figure 6-15 shows the fibre orientation distribution of all slabs. Instead of contour plots, the fibre orientation angle is represented by dots in different colours. The fibre orientation ranges from 0° to 90° from the horizontal axis. It

can be seen that fibres tends to orient at 0° degree at the top and bottom boundaries, while orienting at 90° along the left and right boundaries. There are two possible reasons:

1. Fibre tends to align their orientation to the mould due to wall effect of the slab mould boundary, which is described in Section 2.3.2;
2. Fibre contents at the four boundaries were lower compared to other parts, which resulted from the testing method. The vertical testing value at the top and bottom points and the horizontal testing value at the furthest left and right points were lower.

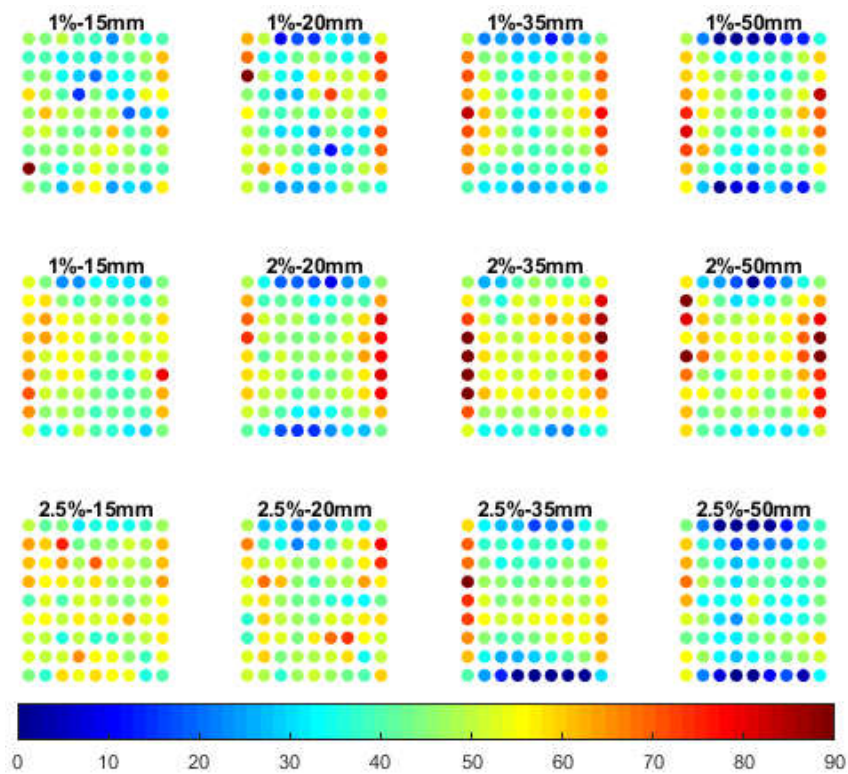


Figure 6-15 Fibre orientation angle distribution of all slabs.

Detailed fibre orientation values can be seen in Table 6-7. It can be seen that fibres tend to align at 45° . The increase of fibre content and fibre distribution do not have a direct relationship with the fibre orientation angle. Because of the wall effect, the coefficient of variance for fibre orientation angle is higher compared to the fibre volume content.

Table 6-7 Mean, STD, and COF of fibre orientation angles of all slabs.

		15 mm	20 mm	35 mm	50 mm
Mean	1% vol.	43	43	45	41
	2% vol.	48	46	54	51
	2.5% vol.	51	48	43	35
Standard deviation	1%	2.8	3.1	3.0	2.6
	2%	2.2	2.4	4.0	3.0
	2.5%	2.0	1.2	3.3	3.7
Coefficient of variance	1% vol.	6.5%	7.2%	6.6%	6.4%
	2% vol.	4.7%	5.3%	7.5%	5.7%
	2.5% vol.	3.9%	2.6%	7.7%	10.8%

Figure 6-16 shows the distribution of fibre orientation angle based on 972 sample points. It can be seen from the graph that the distribution of fibre orientation angle follows a normal distribution.

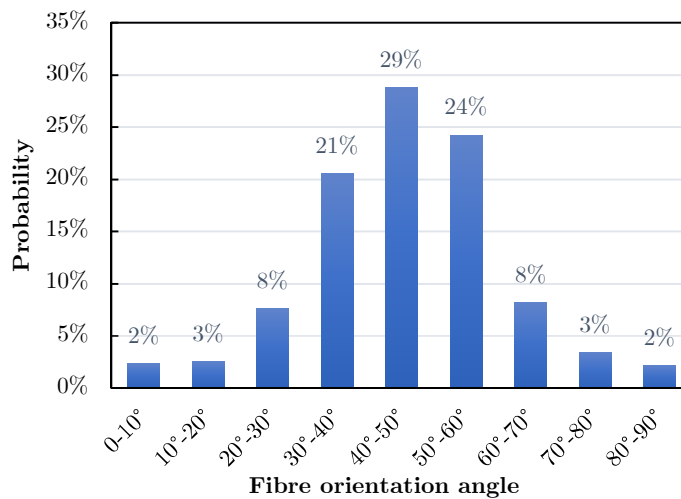


Figure 6-16 Distribution of fibre orientation angle.

The normal distribution function can be calculated based on the mean and standard deviation values of fibre orientation angle. The probability density function can be represented as:

$$f(\varphi) = \frac{1}{\sqrt{2\pi}\sigma} \exp\left(-\frac{(\varphi - STD)^2}{2\sigma^2}\right) \tag{Equation 6-20}$$

where mean $\sigma = 45.595^\circ$ and $STD = 15.315^\circ$. The probability density function graph can be seen in Figure 6-17.

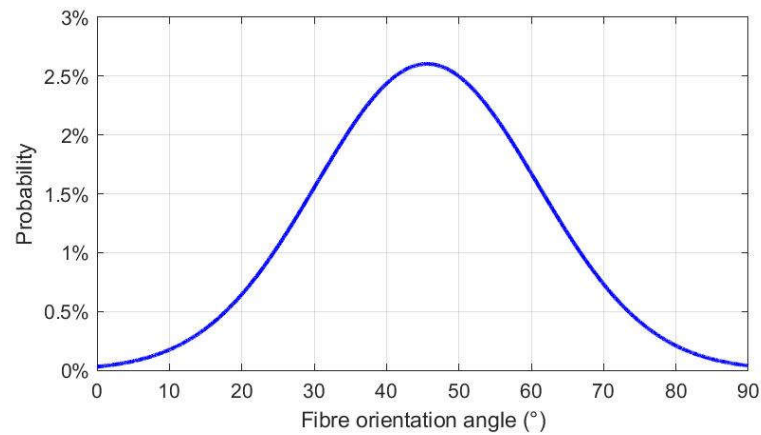


Figure 6-17 Probability density distribution of fibre orientation angle.

6.4.3 Summary

By testing the magnetic inductance of 15, 20, 35, and 50 mm thick UHPFRC slabs with 1%, 2%, and 2.5% fibre vol., both the fibre content and orientation distribution can be obtained on each particular points. Although the effective testing depth of the magnetic probe is limited to 20 mm, the fibres in the bottom part of the beam are the most critical factor in a bending test. Hence, these results are considered relevant to the mechanical properties.

CHAPTER 7 MECHANICAL TEST RESULTS

The mechanical test results are shown in this chapter. Not only the differences between two concrete mix designs are compared, but also the differences between each fibre volume content group. This chapter also includes some general correlation between the mechanical results and the fibre distribution results.

7.1 Compressive Test Results

The compressive test was carried out on SD 2%, 3%, Pre-mix 0, 1%, 2%, 2.5%, and 5% specimens. Six specimens were tested from each group. During the compressive test, a large explosive sound was heard for plain UHPC specimens when the concrete cracked. Concrete was crushed into pieces and behaved in a highly brittle manner after cracking (Figure 7-1a). With the increase in fibre content, fibres were able to restrain the concrete from explosive failure, hence, the sound was lower and the post-cracking stage became more ductile (Figure 7-1b).



Figure 7-1 UHPC and 2% vol. UHPFRC specimens after compressive test.

Figure 7-2 shows the box chart of compressive strength distribution. The average and the variation of compressive strengths of each specimen group can be seen in Table 7-1. The coefficient of variance stays within 5.4%, which demonstrates the reliability of the test. It can be seen that from SD-2% and SD-3%, the compressive strength drops from 167.2 to 151.8 MPa. Although adding too many fibres may reduce the peak compressive strength,

but 3% is still within the applicable range. The main reason for this drop is because the cement was not preserved well. Therefore, it caused the decrease of the compressive strength of the concrete matrix.

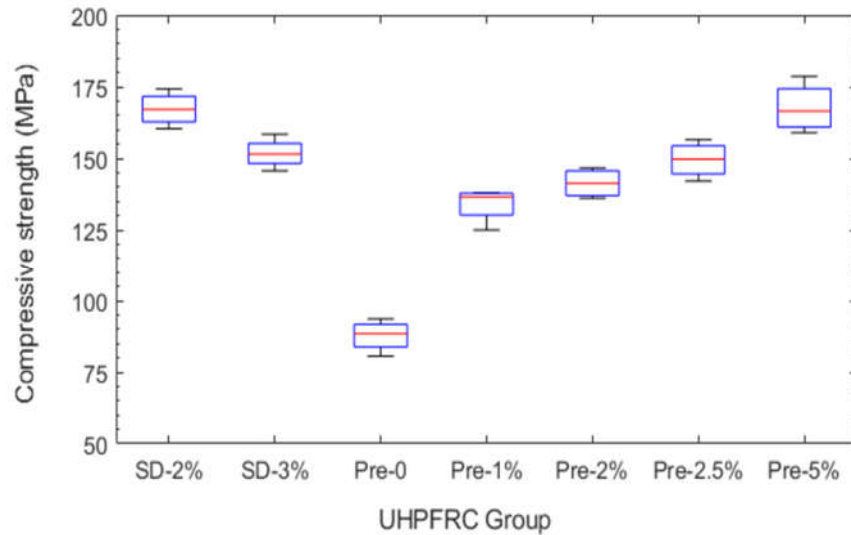


Figure 7-2 Compressive strength of different groups of 100 mm cube specimens.

To solve this problem, the pre-mix powder was used in the later research. The general compressive strength is lower compared to the SD mix design, which can be proved by the 2% vol. SD (167.2 MPa) and Pre-mix (141.4 MPa) groups. Despite this, the Pre-mix group is not as strong as the SD groups, it still fulfils the requirement of being considered as UHPFRC. By adding the fibres, there is a huge jump between 0 and 1% vol. UHPFRC.

Table 7-1 Compressive strength of different groups of 100 mm cube specimens.

Specimen group	Shape	Compressive strength (MPa)		COV
		Average	STD	
SD-2%	100 mm cube	167.2	5.1	3.1%
SD-2%	100 dia. 200 height cylinder	152.4	7.5	4.9%
SD-3%	100 mm cube	151.8	4.5	3.0%
SD-3%	100 dia. 200 height cylinder	140.1	4.9	3.5%
Pre-0	100 mm cube	87.8	4.7	5.4%
Pre-1%	100 mm cube	134.1	5.3	4.0%
Pre-2%	100 mm cube	141.4	4.4	3.1%
Pre-2.5%	100 mm cube	149.5	5.4	3.6%
Pre-5%	100 mm cube	167.6	7.5	4.5%

With the increase of fibre content, the compressive strength steadily and almost linearly increases. There is no drop of compressive strength even at 5% vol. The higher variance

of 5% vol. UHPFRC (STD 7.5 MPa and COV 4.5%) also suggests that fibres are not distributed uniformly inside the concrete matrix. Whether adding more fibres above 5% can further increase the compressive strength remains unknown, but the workability for 5% vol. UHPFRC was not good and the mixing time was longer than other groups. Even if the strength will continue to increase, it is very inconvenient to apply in industry.

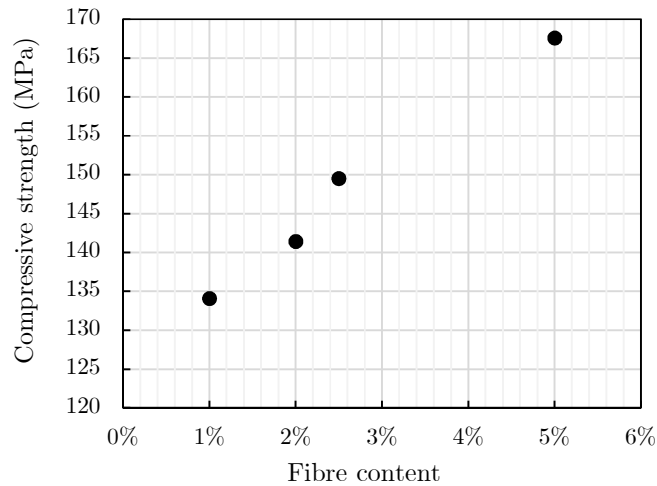


Figure 7-3 Relationship between fibre content and compressive strength for Pre-mix 100 mm cubes.

Apart from the test on 100 mm cube specimens, cylinder specimens with 100 mm dia. and 200 mm height was also tested for SD-2% and 3% vol. UHPFRC. For the both specimens with 100 mm size, the cylindrical specimen has a relatively lower strength. For conventional concrete, the reduction factor is usually around 0.8 [93] [94]. From the test results, the relationship between the compressive strength of 100 mm cube specimens $f_{c,cu}$ and 100 mm dia. cylindrical specimens $f_{c,cy}$ can be calculated as:

$$f_{c,cy} = 0.92 \times f_{c,cu} \quad \text{Equation 7-1}$$

7.2 Uniaxial Tensile Test Results

In total, 12 dog bone specimens were used in the uniaxial tensile test to determine the Young's modulus and uniaxial tensile strength. Three specimens were tested for Pre-mix 1% and 5% vol. UHPFRC. Six specimens were tested for Pre-mix 2% vol. UHPFRC.

Figure 7-4 shows the 2% vol. UHPFRC specimens after cracking. The specimen on the left is an ideal cracked specimen with the tensile crack within the strain gauge region. Previous researchers stated that micro-cracking happens long before the forming of the macro-cracks [17]. In this experiment, no micro-cracking was observed before the macro-crack formed. Hence, in the following description, cracking tensile strength refers to the tensile strength when macro-cracking is first observed.

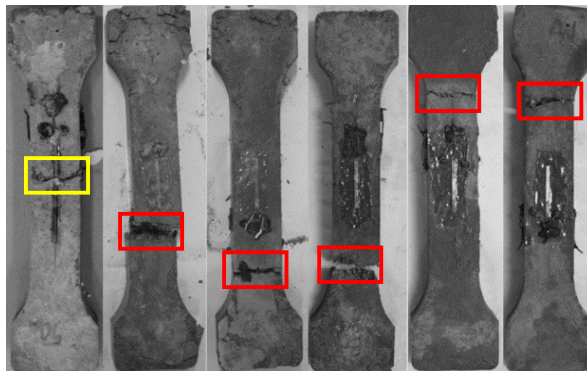


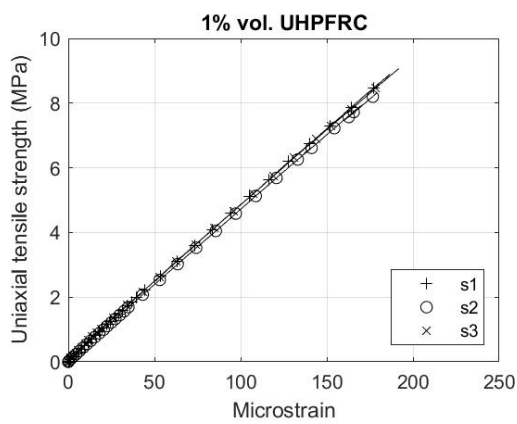
Figure 7-4 2% vol. UHPFRC dog bone specimens after uniaxial tensile test.

Table 7-2 shows the Young's modulus calculated from the linear region of the stress-strain curve for each specimen. For 1% and 2% vol. UHPFRC, Young's modulus is around 47 GPa. When the fibre amount increases to 5%, the Young's modulus increases significantly to 50 GPa since steel fibres have a much higher Young's modulus than UHPC.

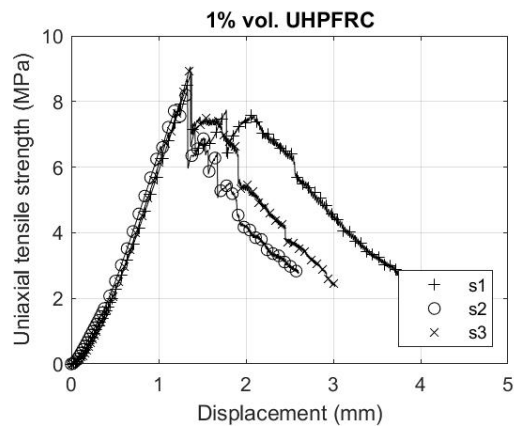
Table 7-2 Young's modulus for all the specimens (unit: GPa).

	1% vol.	2% vol.	5% vol.
s1	47.4	44.72	53.09
s2	46.51	47.44	46.59
s3	47.44	45.08	51.36
s4	-	46.67	-
s5	-	48.14	-
s6	-	47.18	-
Average	47.12	46.54	50.35
STD	0.43	1.24	2.75
COV	0.9%	2.7%	5.5%

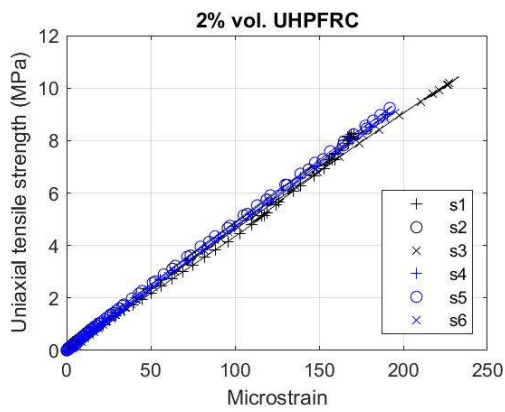
Since the extensometer used in this research is not accurate enough for measuring CMOD, the strain data for each specimen takes the average value of all strain gauges attached. The load data was obtained directly from the testing machine. Based on Equation 5-4, the stress-strain relationship can be seen in Figure 7-5a, c, e. These three figures only state the relationship before concrete cracking, since the data from the strain gauge after cracking is not reliable. Figure 7-5b, d, f show the full load-displacement curves for all specimens. The displacement values were obtained from the movement of the testing clamps.



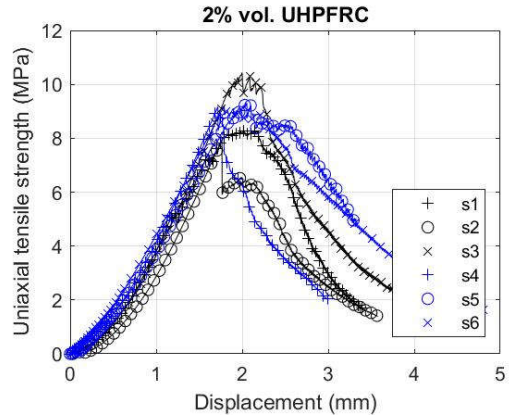
(a) 1% vol. uniaxial tensile stress-strain curve



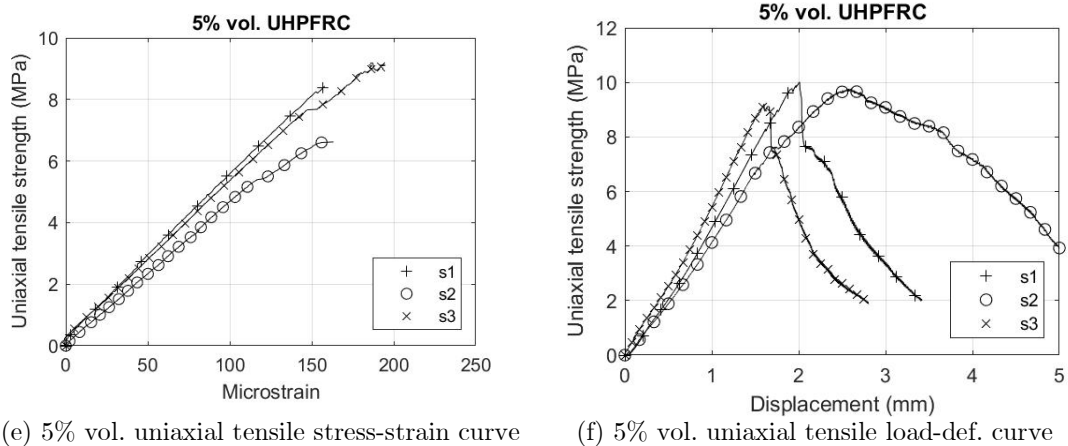
(b) 1% vol. uniaxial tensile load-def. curve



(c) 2% vol. uniaxial tensile stress-strain curve



(d) 2% vol. uniaxial tensile load-def. curve



(e) 5% vol. uniaxial tensile stress-strain curve (f) 5% vol. uniaxial tensile load-def. curve

Figure 7-5 Stress-strain curves and load-displacement curves for all specimens.

Table 7-3 summarized the cracking and peak uniaxial tensile strengths and Young's moduli for each specimen. Combining the curves in Figure 7-5 and the data from Table 7-3, it can be noticed that:

1. The cracking tensile strength mainly depends on the properties of the concrete matrix. The increase of fibre content slightly increases the cracking tensile strength, but over-adding the fibres may reduce the cracking tensile strength, since the fibres will destroy the completeness of the concrete matrix. Especially for specimen s2 of 5%, it has the lowest first crack tensile strength of 6.62 MPa, but the peak tensile strength 9.77 MPa is still above the average;
2. For 1% vol. UHPFRC specimens, a sudden drop of load can be seen after the concrete cracks from Figure 7-5b. Then the load will further increase due to the elongation and pull-out behaviour of fibres, but this load increase will not exceed the previous load peak, therefore, gives a strain softening performance;
3. For 2% vol. UHPFRC specimens, the load-displacement curve in Figure 7-5d shows that most of the loads are sustained after the concrete cracks. Only s2 has a sudden drop after cracking. This suggests that the elongation and pull-out force of fibres for 2% vol. is higher than 1% vol., and the post-cracking performance is related to the fibre orientation distribution;

4. For 5% vol. UHPFRC specimens, the load keeps on increasing after the specimen cracks (Figure 7-5f). This proves that the fibres are sufficient to sustain the tensile load carried by the concrete matrix and give a strain hardening performance.

Table 7-3 Crack and peak uniaxial tensile strength for all the specimens (unit: MPa).

Specimen Number	Crack uniaxial tensile strength			Peak uniaxial tensile strength		
	1% vol.	2% vol.	5% vol.	1% vol.	2% vol.	5% vol.
s1	8.90	7.39	8.43	8.90	8.28	10.01
s2	6.64	9.06	6.62	8.32	9.06	9.77
s3	9.06	9.79	9.18	9.06	10.43	9.21
s4	-	9.17	-	-	9.17	-
s5	-	7.82	-	-	9.31	-
s6	-	9.19	-	-	9.19	-
Average	8.20	8.74	8.08	8.76	9.24	9.66
STD	1.11	0.84	1.07	0.32	0.63	0.34
COV	13.5%	9.6%	13.3%	3.6%	6.8%	3.5%

Compared to the compressive and flexural tests, the direct tensile test is more difficult to perform, and it is even more difficult to obtain the full stress-strain curve. Mainly because:

1. Although the dog bone specimens are used, it was hard to ensure the concrete cracks within the uniaxial tensile region;
2. Due to the length limit of the strain gauges, it is hard to make sure concrete cracks within the strain gauge region. If concrete cracks outside the strain gauge region, the strain data will drop after cracking;
3. Even if the concrete cracks at the strain gauge region, strain gauges will be broken into two parts after cracking. An extremely precise extensometer for measuring the Crack Mouth Opening Displacement (CMOD) is needed.

Apart from these difficulties, another limitation is that the fibre orientation for the specimens cannot be identified, since the steel mould used largely affected the magnetic probe test results.

7.3 Four-Point Bending Test Results

7.3.1 Four-point bending test results for 75×75×450 mm beams

The four point bending test was conducted on SD-2% and 3% vol. 75×75×450 mm UHPFRC beams. Twelve beams were cast for each fibre content group. During casting, half of the beams in each group were vibrated. Thus, the results are divided into four groups, which are 2% vol. non-vibrated, 2% vol. vibrated, 3% vol. non-vibrated, and 3% vol. vibrated beams. The crack location can be seen from Figure 7-6. Yellow arrows and red arrows represent the crack location inside and outside the pure bending region. It can be seen that most beams cracked from bending failure.

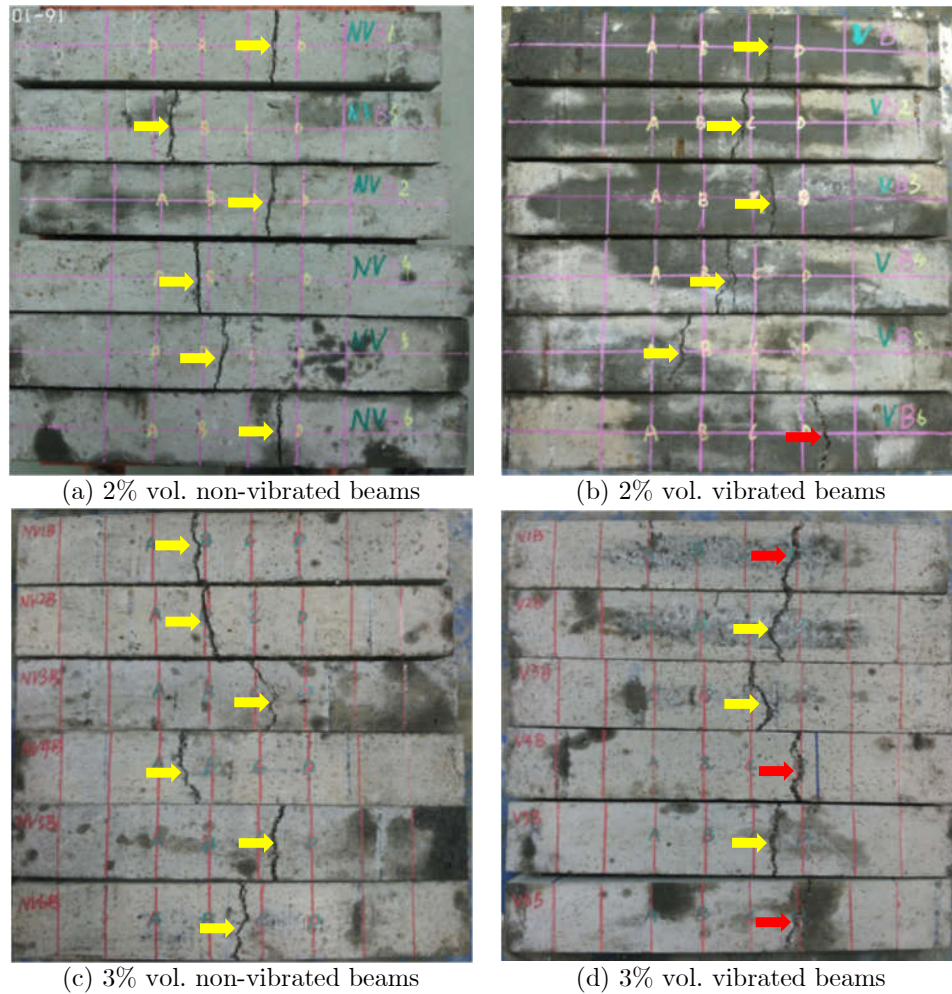


Figure 7-6 75×75×450 mm 2% and 3% vol. beams after four-point bending test.

Figure 7-7 shows the load-deflection curves for all the tested specimens. Apart from the 2% non-vibrated beams, the other three groups have a lower variance. Since the data of s4, s5, and s6 have an extremely large variance, their data are not used in future strength or deflection calculations. Only s1, s2, and s3 are adopted in the non-vibrated 2% vol. UHPFRC group. Generally, all beams behave highly linearly at the beginning and the slopes are very close. For 2% vol. beams, zigzag drops can be seen after the concrete cracks and the load decreases around 3-4 kN (around 2-3 MPa in flexural strength) in each drop. For the 3% vol. UHPFRC beams, the curves are smoother. Even after the concrete cracks, the load slightly drops (1-2 kN) since more fibres are activated.

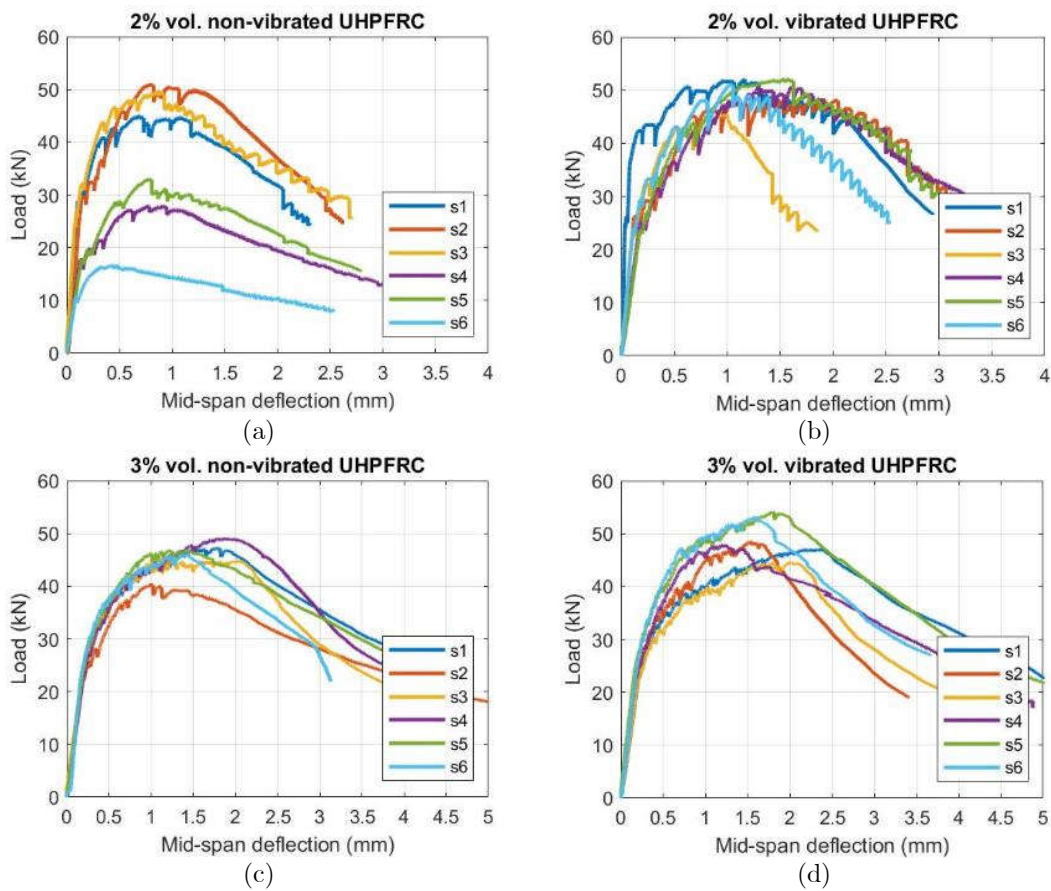


Figure 7-7 Load-deflection curves for 2% and 3% vol. UHPFRC beams.

The average strength, deflection and relative magnetic permeability (RMP) results for each SD specimen group can be seen in Table 7-4. From the previous fibre distribution results in Section 6.3.2, the number of fibres in the bottom region is larger after vibration. The differences between vibrated and non-vibrated UHPFRC beams prove that the

critical part of a beam in a bending test is the bottom region of the beam. With the increase of fibre content, the vibrated beams has a higher flexural strength and mid-span deflection. Although from literature, the flexural strength should increase with the increase of fibre content, this research gives an opposite result. This is mainly resulted from the low compressive strength of the 3% vol. UHPFRC (151.8 MPa comparing to 2% vol. of 167.2 MPa).

Table 7-4 Average peak flexural strength, corresponding mid-span deflection and RMP for SD group.

	First crack strength (MPa)	Peak flexural strength (MPa)	Mid-span deflection (mm)	RMP
2% vol. non-vibrated	19.1	34.5	0.78	1.071
2% vol. vibrated	19.1	35.5	1.24	1.077
3% vol. non-vibrated	17.4	32.6	1.43	1.112
3% vol. vibrated	17.3	35.0	1.78	1.122

7.3.2 Four-point bending test results for 100×100×400 mm beams

Four-point bending tests were also conducted on Pre-mix 1%, 2%, and 5% vol. 100×100×400 mm UHPFRC beams. Each group has four specimens. From the cracked specimen photos in Figure 7-8a, b, it can be seen that there is an inclined crack for specimen 2% vol. - s2. Ideally, the cracking pattern should be almost straight from bottom to top in a four-point bending test. The non-ideal cracking pattern may result from the inappropriate testing setup, which may cause the rotation of the beam during loading. Thus, specimens with 2% vol. - s2 are not taken into account in further calculations.

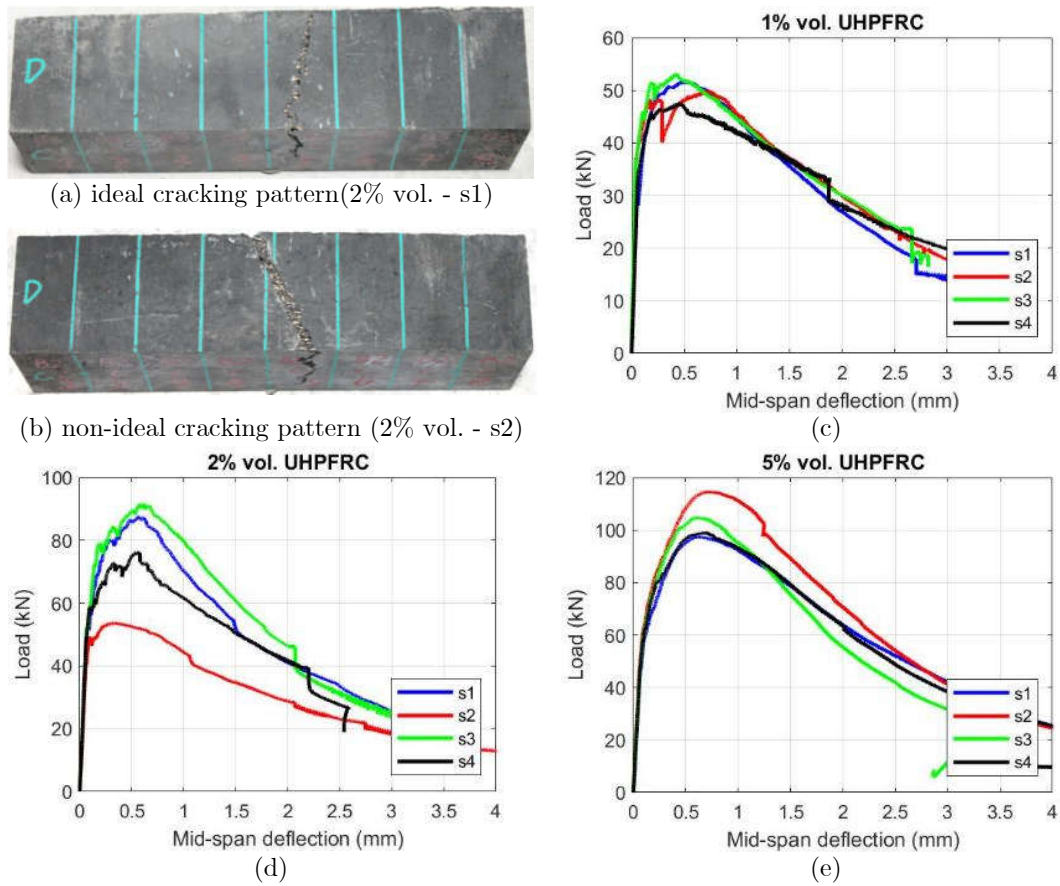


Figure 7-8 Load-deflection curves for 1%, 2%, and 5% vol. UHPFRC beams.

Table 7-5 shows the average peak flexural strength and corresponding mid-span deflection for Pre-mix specimen group. Compared to 2% vol. self-developed mix design, the peak flexural strength of 2% vol. Pre-mix group is 10 MPa lower, considering that the compressive strength is also lower.

Table 7-5 Average peak flexural strength, corresponding mid-span deflection, and RMP for Pre-mix group.

Specimen group	Peak flexural strength (MPa)	Mid-span deflection (mm)	RMP
Pre-mix 1% vol.	15.0	0.53	1.032
Pre-mix 2% vol.	25.5	0.56	1.082
Pre-mix 5% vol.	31.2	0.67	1.152

7.3.3 Four-point bending test summary

From the uniaxial tensile test results and the four-point bending test results, it can be concluded that:

1. The first crack strength depends highly on the properties of the concrete matrix. Adding fibres usually has little positive impact, on the contrary it may slightly decrease the first crack strength with a large dosage;
2. With the increase of fibre content, the peak tensile strength and flexural strength increase accordingly, and the same with mid-span deflection;
3. The addition of fibres will enhance the post-cracking performance of UHPFRC. The load-deflection curve tends to become smoother with the increase of fibre content.

In the four-point bending test, the effect of fibre content on the mechanical performance of UHPFRC can be seen. However, the relationship between fibre orientation and mechanical performance cannot be obtained from this experiment. This is mainly because of the limitation of the testing region. The initial purpose of broadening the beam width from 75 mm to 100 mm is because the vertical inductance cannot be measured. Although the length of the magnetic probe is 93 mm, the fibres outside the 93 mm region will also slightly affect the inductance value. Even for 100×100 mm cross section beams, the limitation of testing boundaries still exists.

Since the capacity of the testing machine is 30 tons (maximum load of 300kN), it is not possible to further increase the cross section size of the specimen. In order to diminish the effect of testing boundaries, the test was then conducted on a 500×500×H mm slabs, and then, beams were extracted from the slabs. Three-point bending tests was used instead of four-point bending tests to prevent the beam failing from shear or rotation and focus more on the mid-span performance.

7.4 Three-point Bending Test Results

The three-point bending test was conducted on 50×200×H mm Pre-mix UHPC, 1%, 2%, and 2.5% vol. UHPFRC beams cut from 500×500×H mm slabs. Eight beams were tested for each fibre volume content group. Figure 7-9 shows the cracked 50×200×20 mm beams. It can be seen from the photos that the majority of beams cracked in the middle of the span. Due to the lack of fibre bridging, UHPC beams cracked into two pieces after reaching the peak load (Figure 7-9a).

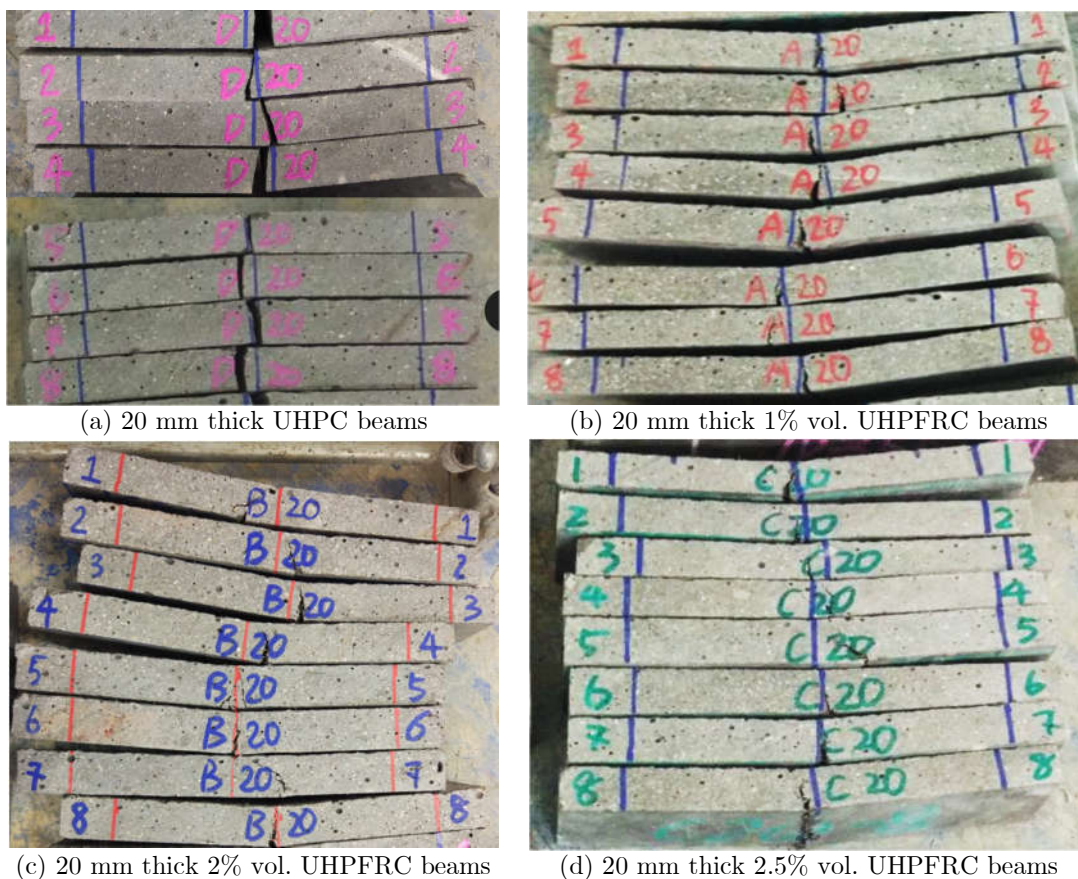


Figure 7-9 50×200×20 mm beams after three-point bending test.

Figure 7-10 shows the relationship between the slab thickness and the average peak flexural strength for four groups of specimens. Although previous researchers stated a relationship between the beam thickness and peak flexural strength, it is not applicable in this experiment. Because the beam thickness is very thin, comparing the specimen size, fibre distribution has a more significant effect on the flexural performance.

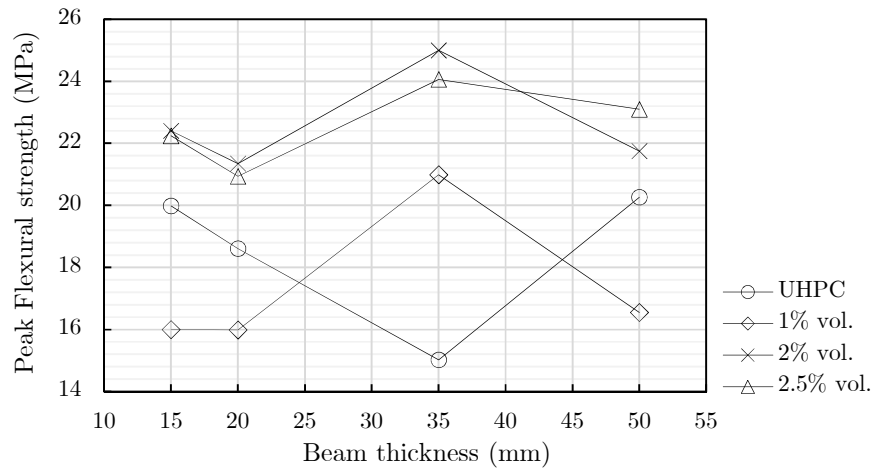


Figure 7-10 Relationship between beam thickness and average peak flexural strength.

Detailed first crack flexural strength and peak flexural strength of each specimen group can be seen in Table 7-6. The merged cell on the right side shows the average value of four slabs. For UHPC, no micro or macro-cracks can be observed before reaching peak load. The first crack strength is equal to the peak flexural strength.

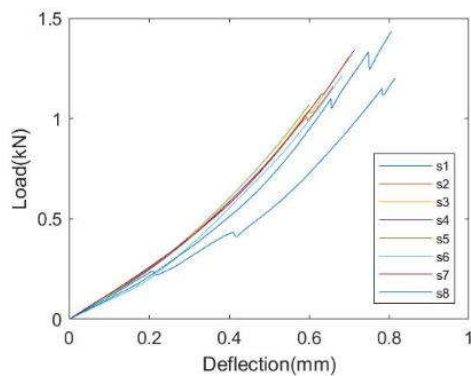
Table 7-6 First crack flexural strength and peak flexural strength for Pre-mix specimens (unit: MPa).

Fibre volume content-thickness	First crack flexural strength	Peak flexural strength		
0 - 15	20.0	20.0	18.5	
0 - 20	18.6	18.6		
0 - 35	15.0	15.0		
0 - 50	20.3	20.3		
1% - 15	15.1	16.3	16.0	17.4
1% - 20	13.9		16.0	
1% - 35	20.2		21.0	
1% - 50	15.8		16.6	
2% - 15	18.5	18.6	22.4	22.6
2% - 20	16.8		21.4	
2% - 35	19.6		25.0	
2% - 50	19.4		21.8	
2.5% - 15	18.0	17.9	22.2	22.6
2.5% - 20	16.2		20.9	
2.5% - 35	18.3		24.1	
2.5% - 50	18.9		23.1	

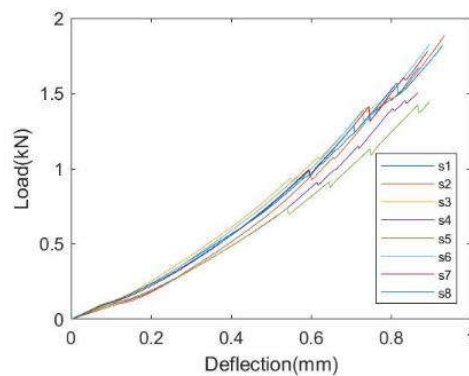
Figure 7-11 shows the load-deflection curves for 15 and 20 mm thick beams. Since no deflection gauge was used to measure the deflection, the deflection and load data from

the testing machine are used in this figure. Load-deflection plots for all the beams are attached in Appendix 2. For the UHPC beams, the load drops in the curve do not represent a concrete crack. This mainly resulted from the concrete crushing at the loading point. In the previous four-point bending test, the smooth side faces were used for loading and support. Unlike the four-point bending test, the casting face was also the testing face in this experiment. Only the sand paper were used to smooth the surface before the test, therefore, some rough places were unavoidable. UHPC beams behave in a highly brittle manner after the peak load, so no post-cracking performance can be observed.

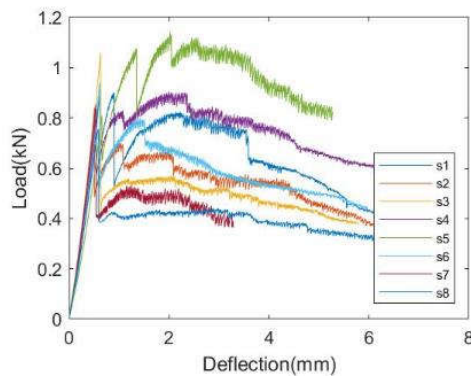
For all the 1% vol. UHPFRC beams, the load drops severely after peak load. After the sudden load drop, the load will keep on increasing due to the activation of the bridging effect of the fibres. Nevertheless, for 2% and 2.5% vol. UHPFRC beams, the load will also drop but due to the bridging effect of fibres, most beams have strain hardening performance. Only 5 and 3 beams in 2% and 2.5% vol. group did not have strain hardening effect.



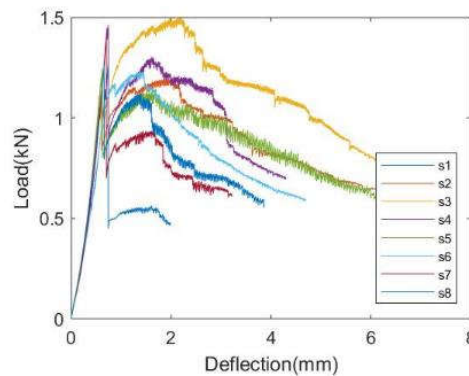
(a) UHPC 50×200×15 mm beams



(b) UHPC 50×200×20 mm beams



(c) 1% vol. 50×200×15 mm beams



(d) 1% vol. 50×200×20 mm beams

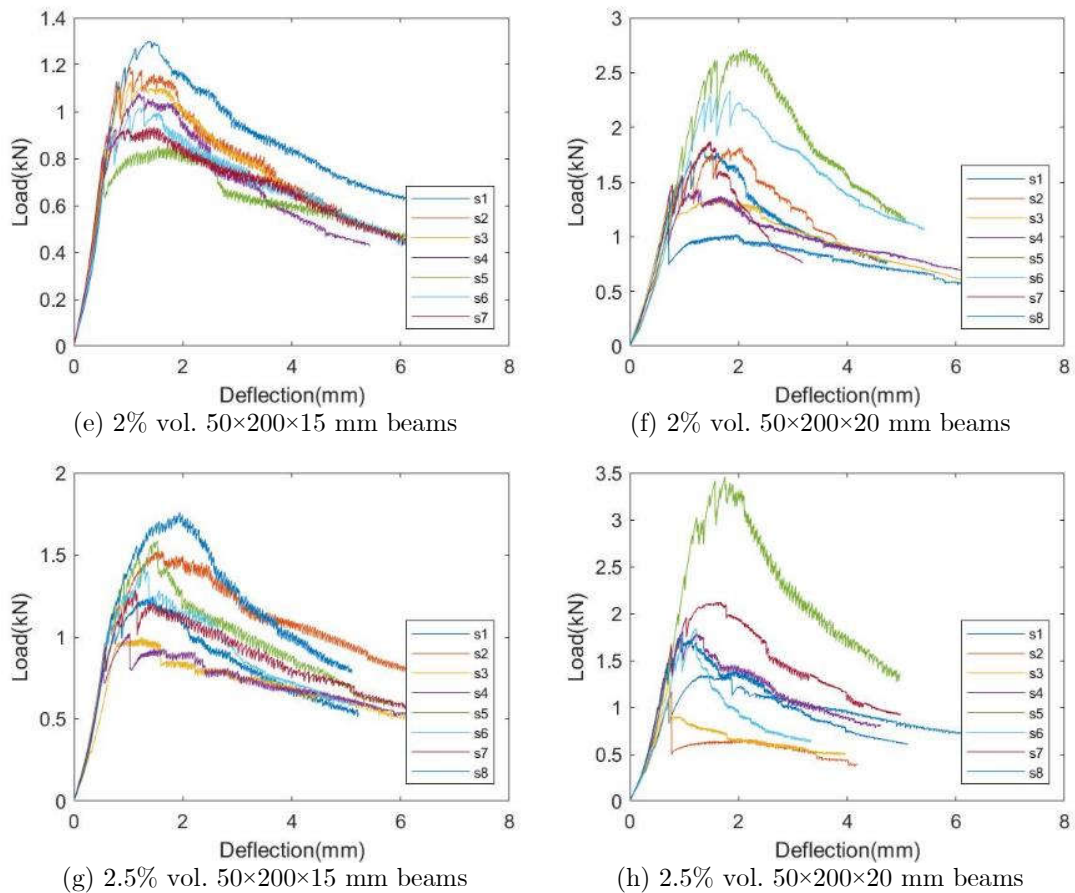


Figure 7-11 Load-deflection curves for 15 and 20 mm thick UHPC and UHPFRC beams.

As stated in Section 6.4.1, there are some differences of fibre volume content within each slab, but these differences are very small. Even for the 2.5%-15 mm slab with the biggest variance, the standard deviation is only 0.052% vol. These differences can even be neglected in the construction field and it usually will not cause a large mechanical performance variance.

However, it can be seen from Figure 7-11, the mechanical performance before and after cracking has a relatively large variation. For example, in Figure 7-11h, s5 shows a superior performance compared to other specimens. Therefore, apart from the influence of fibre content, the impact of fibre orientation should also be considered. The detailed relationship between the fibre distribution and the mechanical performance will be further discussed and analysed in the following chapter.

CHAPTER 8 ANALYSES AND DISCUSSIONS

As analysed in the Chapter 7, with the increase of fibre amount, the peak flexural strength increases. However, for the specimens with same concrete matrix and fibre volume content, the mechanical performance also varies. The difference is the fibre orientations of the specimens. Following discussions are mainly focusing on the relationship between fibre volume content, fibre orientation angle, first crack strength, and peak uniaxial tensile strength. Finite element analyses of ANSYS and Opensees are used to validate the theoretical derivations.

8.1 Theoretical Derivation on Working Mechanism of UHPFRC after Crack

Since the uniaxial tensile test is difficult to perform, flexural test is always used instead to determine the tensile performance of the material indirectly, especially on thin members. As stated in Section 2.1.2, for both uniaxial tensile test and flexural test, UHPFRC go through two main stages after crack: fibre activation stage and fibre pull-out stage. These two stages determine how UHPFRC perform, whether strain hardening or strain softening behaviour will occur. The forces result from fibre activation and fibre pull-out are closely related to the number of fibre across the crack plane and the fibre orientation angle. The following section will introduce the mechanisms of these two stages.

8.1.1 Fibre activation stage

Initially in the uniaxial tensile test, fibres are initially bonded with concrete, and the tensile load is mainly carried by the concrete matrix. Thus, the first crack tensile strength mainly depends on the tensile properties of concrete matrix. After concrete cracks, concrete can hardly sustain any loads. At this point, fibres are not pulled-out yet due to the static frictional force τ between fibres and concrete matrix.

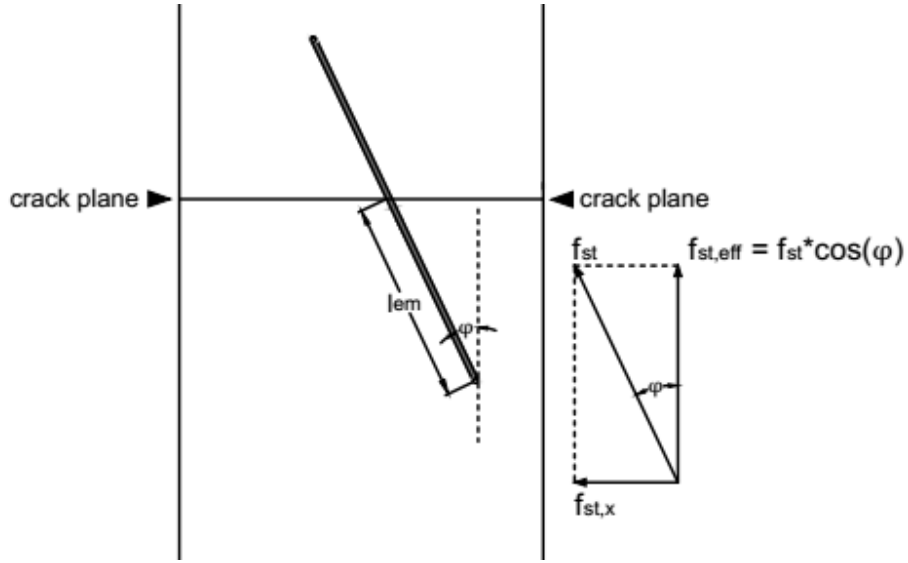


Figure 8-1 Effective embedment length of fibres inside concrete matrix in uniaxial tensile test in fibre activation stage.

The effective static frictional force $f_{st,eff}$ carried by one fibre can be estimated as:

$$f_{st} = \pi \cdot d_f \cdot l_{em} \cdot \tau \quad \text{Equation 8-1}$$

$$f_{st,eff} = f_{st} \cdot \cos\varphi = \pi \cdot d_f \cdot l_{em} \cdot \tau \cdot \cos\varphi \quad \text{Equation 8-2}$$

where

- f_{st} static frictional force;
- $f_{st,eff}$ effective static frictional force;
- d_f fibre diameter;
- l_{em} effective embedment length;
- τ static frictional strength;
- φ fibre orientation angle.

The total effective static frictional force $f_{st,n}$ can be calculated as:

$$f_{st,n} = f_{st,eff} \cdot n_f = \pi \cdot d_f \cdot l_{em} \cdot \tau \cdot \cos\varphi \cdot n_f \quad \text{Equation 8-3}$$

If the concrete matrix is consistent, the relationship between uniaxial tensile strength $f_{t,\varphi 1}$, $f_{t,\varphi 2}$ at different fibre orientation angles φ_1 , φ_2 can be calculated as:

$$\frac{f_{t,\varphi 1}}{\cos(\varphi_1) \cdot V_{f1}} = \frac{f_{t,\varphi 2}}{\cos(\varphi_2) \cdot V_{f2}} \quad \text{Equation 8-4}$$

8.1.2 Fibre pull-out stage

With the increase of uniaxial tensile load, the static frictional force also increases. Until the static frictional force reaches the maximum static frictional force τ_0 , fibres start to be pulled-out gradually. The force are transferred into sliding frictional force. With the increase of crack width, the effective embedment length decreases, therefore, the load starts to decrease.

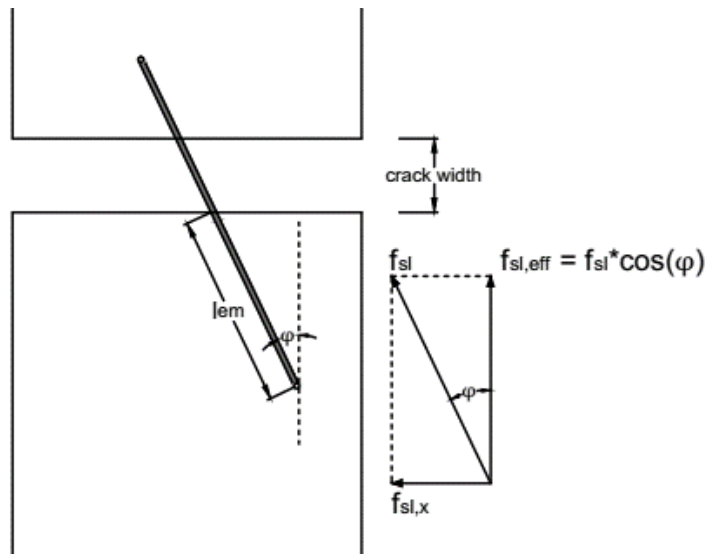


Figure 8-2 Effective embedment length of fibres inside concrete matrix in uniaxial tensile test in fibre pull-out stage.

Assuming the shear frictional strength τ_0 on the surface of the fibre is. The total effective sliding frictional force can be calculated as

$$f_{sl,n} = f_{sl,eff} \cdot n_f = \pi \cdot d_f \cdot l_{em} \cdot \tau_0 \cdot \cos\varphi \cdot n_f \quad \text{Equation 8-5}$$

where

- n_f number of fibres across the crack plane;
- f_{sl} sliding frictional force;
- $f_{sl,eff}$ effective sliding frictional force.

8.2 Further Analysis on Three-point Bending Test

8.2.1 Peak uniaxial tensile strength of UHPC

UHPC is a highly brittle material, and the first crack flexural strength is the peak flexural strength in this experiment. Since no uniaxial tensile experiment was conducted on pure UHPC specimens, the uniaxial tensile strength for pure UHPC was derived from bending results using Equation 2-4. It can be seen, apart from the 50 mm specimens, the calculated peak uniaxial tensile strength is around 7.34 MPa. The strength difference for the 50 mm specimens is mainly because that the effective span is not large enough compared to the specimen height. In later discussion, the peak uniaxial tensile strength will be taken as 7.34 MPa.

Table 8-1 Experimental peak flexural strength and calculated peak uniaxial tensile strength of UHPC (unit: MPa).

Plate thickness		Experimental peak flexural strength	Calculated peak uniaxial tensile strength
15mm	Average	20.0	7.32
	STD	2.0	0.08
20mm	Average	18.6	7.35
	STD	1.6	0.04
35mm	Average	15.0	7.34
	STD	1.2	0.07
50mm	Average	20.3	11.35
	STD	1.1	0.05

However, Equation 2-4 cannot be used directly to transform the bending results to uniaxial tensile results for UHPFRC, since fibre plays an important role after crack, but this equation only considers the material property of concrete matrix.

8.2.2 Relationship between fibre distribution and peak flexural strength of UHPFRC

For the specimens used for the four-point bending test, the orientation of fibres could not be tested due to the limitation of the probe. Fortunately, for the UHPFRC slabs, both the fibre content V_f and fibre orientation angle φ can be tested using the magnetic probe and the results can be seen in Section 6.4.2. The detailed mechanical performance and

fibre distribution of each specimen can be seen in Table 8-2. Due to the some operation mistakes, the bending test result of sample 2%-15-s3 and 2.5%-15-s3 are missing. From Equation 8-3, a linear relationship can be seen between peak uniaxial tensile strength and $n_f \cdot \cos(\varphi)$ (also $V_f \cdot \cos(\varphi)$).

Table 8-2 First crack, peak flexural strength and fibre distribution of Pre-mix specimens.

Specimen number	First crack flexural strength (MPa)	Peak flexural strength (MPa)	Fibre content	Fibre orientation angle
1%-15-s1	14.8	14.9	1.04%	38°
1%-15-s2	14.5	14.5	0.98%	46°
1%-15-s3	18.8	18.8	0.95%	43°
1%-15-s4	14.5	16.0	0.98%	31°
1%-15-s5	12.8	18.0	1.01%	37°
1%-15-s6	16.1	16.1	0.98%	50°
1%-15-s7	15.9	15.9	0.95%	56°
1%-15-s8	13.8	13.8	0.95%	63°
1%-20-s1	12.7	14.1	1.02%	44°
1%-20-s2	12.9	14.5	1.04%	36°
1%-20-s3	13.7	17.1	0.99%	34°
1%-20-s4	17.2	17.3	0.99%	43°
1%-20-s5	15.1	15.9	0.99%	29°
1%-20-s6	13.3	14.0	0.93%	39°
1%-20-s7	13.6	18.2	0.96%	39°
1%-20-s8	12.7	16.8	1.02%	36°
1%-35-s1	18.1	24.1	0.99%	34°
1%-35-s2	22.7	22.7	1.02%	41°
1%-35-s3	22.2	22.2	0.99%	46°
1%-35-s4	18.7	18.7	0.99%	50°
1%-35-s5	21.5	21.6	1.02%	34°
1%-35-s6	19.2	19.2	1.02%	42°
1%-35-s7	20.8	20.8	0.99%	42°
1%-35-s8	18.7	18.7	0.99%	47°
1%-50-s1	19.2	23.2	1.17%	30°
1%-50-s2	14.8	17.0	1.25%	40°
1%-50-s3	15.2	15.2	1.17%	47°
1%-50-s4	15.3	15.3	1.15%	50°
1%-50-s5	15.7	15.7	1.12%	41°
1%-50-s6	14.5	14.5	1.15%	51°
1%-50-s7	16.0	16.0	1.12%	55°
1%-50-s8	15.4	15.4	1.10%	52°
2%-15-s1	18.2	25.4	2.02%	36°
2%-15-s2	18.9	25.0	2.06%	40°
2%-15-s3	-	-	2.06%	38°
2%-15-s4	17.0	23.1	2.02%	42°
2%-15-s5	19.6	22.5	1.93%	38°

2%-15-s6	19.0	19.3	2.06%	44°
2%-15-s7	20.1	22.4	2.02%	41°
2%-15-s8	16.6	19.1	2.02%	39°
2%-20-s1	17.5	22.6	1.80%	38°
2%-20-s2	17.7	22.2	1.80%	48°
2%-20-s3	17.3	17.5	1.77%	50°
2%-20-s4	13.7	17.9	1.74%	48°
2%-20-s5	19.9	29.5	1.83%	24°
2%-20-s6	16.1	24.1	1.83%	37°
2%-20-s7	17.5	22.2	1.74%	45°
2%-20-s8	14.8	14.8	1.65%	50°
2%-35-s1	17.4	25.4	1.91%	38°
2%-35-s2	19.3	19.3	1.91%	53°
2%-35-s3	18.8	18.8	1.85%	54°
2%-35-s4	17.9	17.9	1.80%	53°
2%-35-s5	20.2	35.8	1.91%	17°
2%-35-s6	18.6	27.6	1.83%	28°
2%-35-s7	26.4	28.9	1.80%	28°
2%-35-s8	18.5	26.2	1.83%	28°
2%-50-s1	27.6	27.6	1.96%	28°
2%-50-s2	18.0	18.8	1.98%	41°
2%-50-s3	17.4	18.4	1.98%	46°
2%-50-s4	16.9	20.8	2.04%	43°
2%-50-s5	16.2	17.7	1.98%	52°
2%-50-s6	27.7	30.0	1.85%	18°
2%-50-s7	16.7	24.4	1.91%	29°
2%-50-s8	17.1	17.1	1.85%	36°
2.5%-15-s1	17.2	21.0	2.45%	50°
2.5%-15-s2	20.1	21.0	2.45%	46°
2.5%-15-s3	-	-	2.35%	54°
2.5%-15-s4	14.0	25.6	2.32%	52°
2.5%-15-s5	20.1	21.1	2.19%	36°
2.5%-15-s6	19.1	21.0	2.12%	41°
2.5%-15-s7	16.9	25.2	2.02%	39°
2.5%-15-s8	18.9	20.9	1.99%	30°
2.5%-20-s1	14.9	18.5	2.23%	51°
2.5%-20-s2	14.8	16.5	2.32%	65°
2.5%-20-s3	15.1	15.1	2.35%	61°
2.5%-20-s4	20.0	22.5	2.38%	43°
2.5%-20-s5	14.2	32.3	2.35%	25°
2.5%-20-s6	15.2	18.7	2.32%	39°
2.5%-20-s7	18.4	23.3	2.32%	40°
2.5%-20-s8	17.1	20.7	2.18%	40°
2.5%-35-s1	18.4	33.3	2.51%	28°
2.5%-35-s2	19.1	24.8	2.53%	48°
2.5%-35-s3	20.6	20.6	2.45%	56°
2.5%-35-s4	15.8	15.8	2.35%	55°

2.5%-35-s5	20.1	24.1	2.35%	41°
2.5%-35-s6	18.1	22.7	2.40%	46°
2.5%-35-s7	18.8	29.9	2.48%	47°
2.5%-35-s8	15.2	21.4	2.45%	51°
2.5%-50-s1	20.0	25.5	2.25%	33°
2.5%-50-s2	16.9	20.5	2.35%	46°
2.5%-50-s3	22.0	26.1	2.38%	40°
2.5%-50-s4	27.6	30.5	2.32%	33°
2.5%-50-s5	18.2	21.2	2.27%	46°
2.5%-50-s6	13.7	20.2	2.35%	51°
2.5%-50-s7	16.5	21.5	2.35%	52°
2.5%-50-s8	16.5	19.2	2.27%	54°

Figure 8-3 shows the load-deflection curves for two typical types of load-deflection curve for 1% vol. UHPFRC beams. A load drop can be seen after 0.8 kN, and then, the load keeps on increasing to some extent owing to the activation of fibres. For example, for specimen 1%-15-s4, the maximum load exceeds the flexural load at first crack. However, for 1%-15-s6, there is no such enhancing performance. As can be read from Table 8-2, the fibre volume contents have little variance. In addition, the concrete matrix properties are the same. The only variance is the fibre orientation angle. This difference not only happens to 1%-15mm beams but also beams with 20, 35, and 50 mm thicknesses.

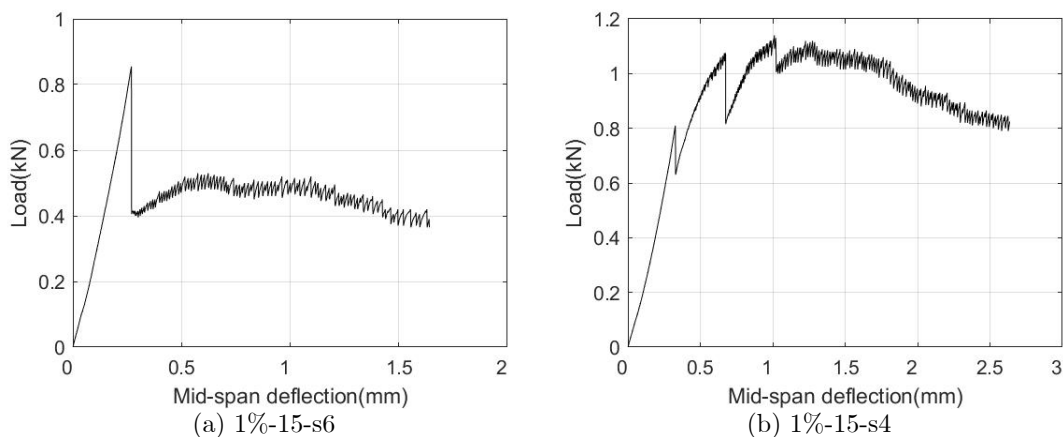


Figure 8-3 Load-deflection curves for 1% vol. 200×50×15 mm UHPFRC beams.

From the uniaxial tensile test results for 1% vol. UHPFRC (Figure 7-5b), there is no strain softening behaviour. However, the fibre orientation angle was not tested in the uniaxial tensile test, and only three specimens were tested. It can be concluded that, for 1% vol. UHPFRC specimens, when the fibre orientation angle is large, the reaction force between fibre and concrete matrix is not strong enough to produce a strain hardening

behaviour. With the decrease of fibre orientation angle, the reacting force becomes stronger and hardening behaviour can be observed. Only 9 out of 32 1% vol. UHPFRC beams have obvious strain hardening behaviour.

Hence, the first crack strength of 1% vol. UHPFRC is mainly determined by the material properties of concrete matrix, so there is no obvious relationship between the fibre distribution and peak flexural strength for 1% vol. UHPFRC (see Figure 8-4).

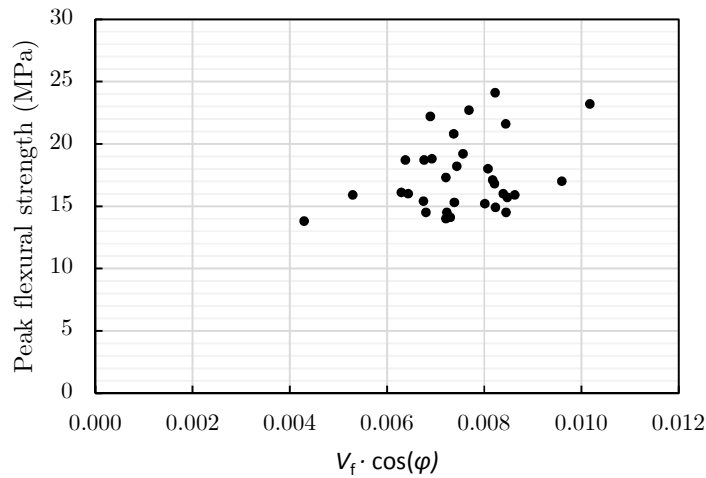


Figure 8-4 Relationship between $V_f \cdot \cos(\varphi)$ and peak flexural strength for 1% vol. UHPFRC beams.

Low strain hardening behaviour can be seen in uniaxial tensile strength for 2% vol. UHPFRC, as shown in Figure 7-5d. With the increase of fibre content, more fibres were activated and the loads carried by fibres are higher. Only 5 out of 31 beams do not have strain hardening behaviour after first crack. Most of the strain softening beams have an orientation angle above 50° .

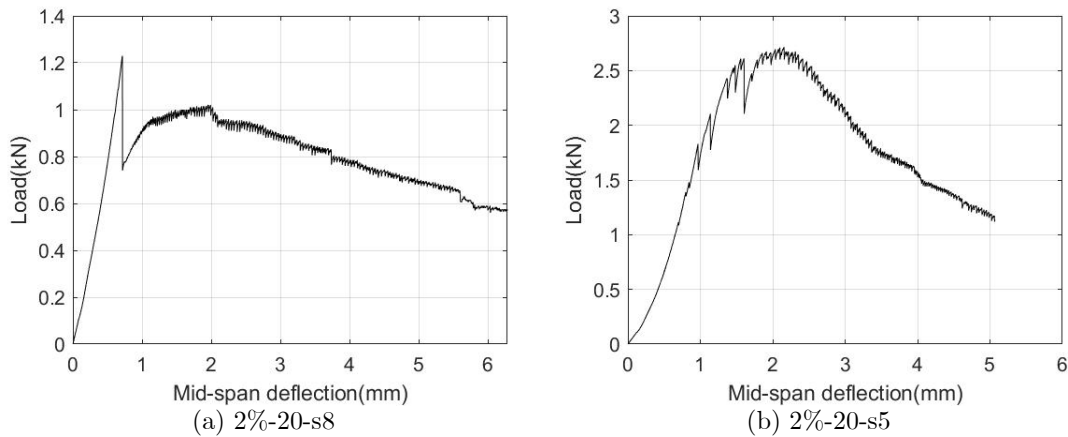


Figure 8-5 Load-deflection curves for 2% vol. 200×50×20 mm UHPFRC beams.

In this case, the peak flexural strength is significantly influenced by the fibre orientation angle. Figure 8-6 shows a linear relationship between $V_f \cdot \cos(\varphi)$ and the peak flexural strength. $\cos(\varphi)$ approaching 1 represents the orientation angle is approaching 0° , therefore, suggesting more fibres are perpendicular to the cracking plane. A linear regression analysis is given in the graph with an R-squared value of 0.5872. Since the peak flexural strength of UHPC is around 20 MPa, this curve is better fitted to the points above 20 MPa.

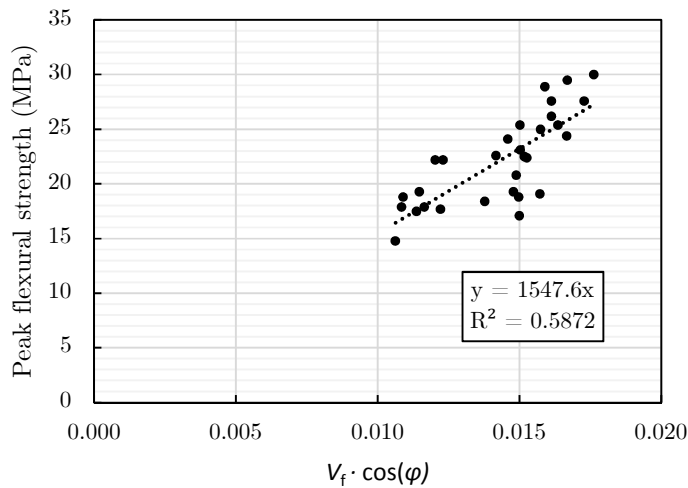


Figure 8-6 Relationship between $V_f \cdot \cos(\varphi)$ and peak flexural strength for 2% vol. UHPFRC beams.

For 2.5% vol. UHPFRC beams, only 3 out of 31 beams do not have strain hardening performance. Figure 8-7 also shows a linear relationship between $V_f \cdot \cos(\varphi)$ and peak

flexural strength, with a similar slope value of 1388.3 compared to 2% vol. Some values are not included in the graph because the fibre content is relative low, for example, 2.5%-15-s5, 6, 7, and 8.

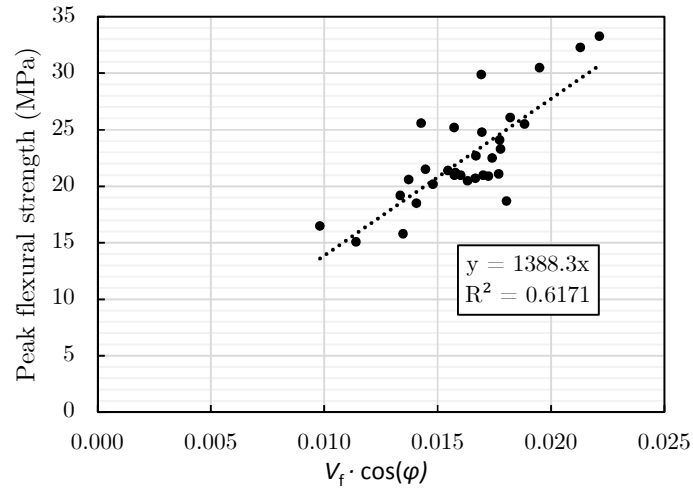


Figure 8-7 Relationship between $V_f \cdot \cos(\varphi)$ and peak flexural strength for 2.5% vol. UHPFRC beams.

8.3 Multiscale FEM using Digimat and ANSYS

8.3.1 Fibre geometry generation using Digimat

Digimat is a multiscale material modelling technology that helps the development of composite materials and structures. It can be used to form an analysis on both the micro- and macro-scopic level and work together with other finite element analyses software such as Ansys and Abaqus. The FE module in Digimat suite is usually used for generating the Representative Volume Element (RVE) of plastics, rubber, metal, graphite, etc. In this research, Digimat-FE is used to generate a concrete matrix containing steel fibres.

The first step for generating the UHPFRC geometry is to define the types of material used. The concrete and fibre can be defined separately as matrix and inclusion (see Figure 8-8).

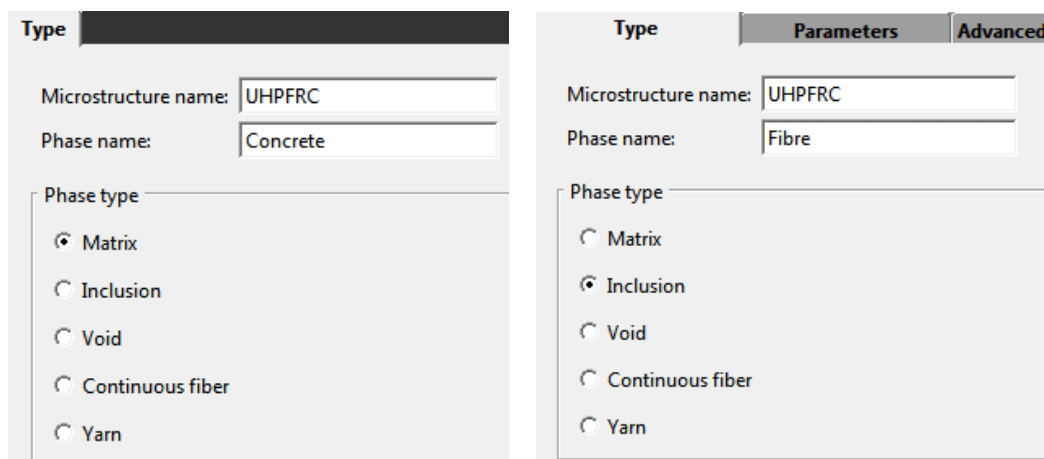


Figure 8-8 Define phase type of concrete and fibre in Digimat.

Next, the distribution of fibres inside concrete matrix was defined as in Figure 8-9. The fibre volume content can be input as volume fraction. The orientation distribution was input as fibre orientation tensor, as stated in Section 2.2.1. Here take random 3D distribution as an example.

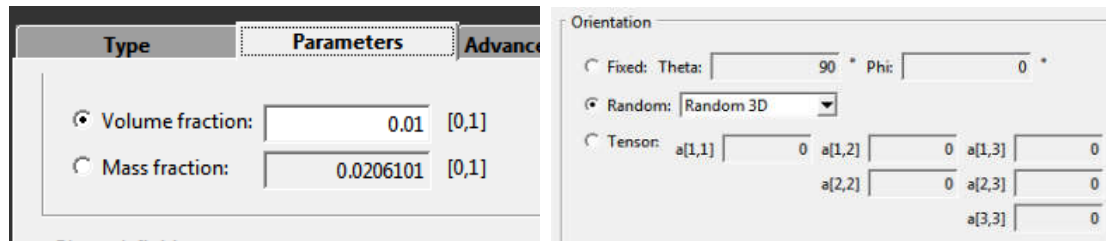


Figure 8-9 Define fibre volume content and fibre orientation distribution.

Then, the overall dimension (also known as RVE) of the UHPFRC model is defined as in Figure 8-10. The minimum relative distance between inclusions was set to be zero. The minimum relative volume (relative to elementary inclusion volume) was set to be one to avoid any cut-off part.

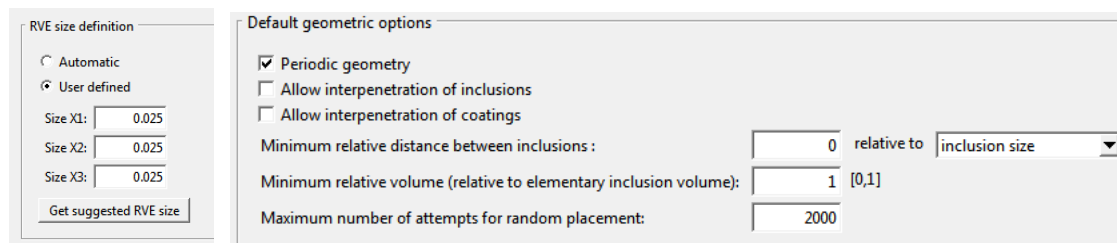


Figure 8-10 Define RVE options.

Due to the limitations of computer hardware, it is difficult to make a full-scale UHPFRC cube or beam model. Take a 100×100×100 mm 1% vol. UHPFRC cube with 12.5 mm long and 0.25 mm dia. fibres as an example, the model would contain 32595 fibres. Figure 8-11 shows the general and side views of a 3D random distribution cube model. This model has a size of 25×25×25 mm and 1% fibre volume content, counted to contain 255 fibres. The model was then export as an ‘.iges’ file.

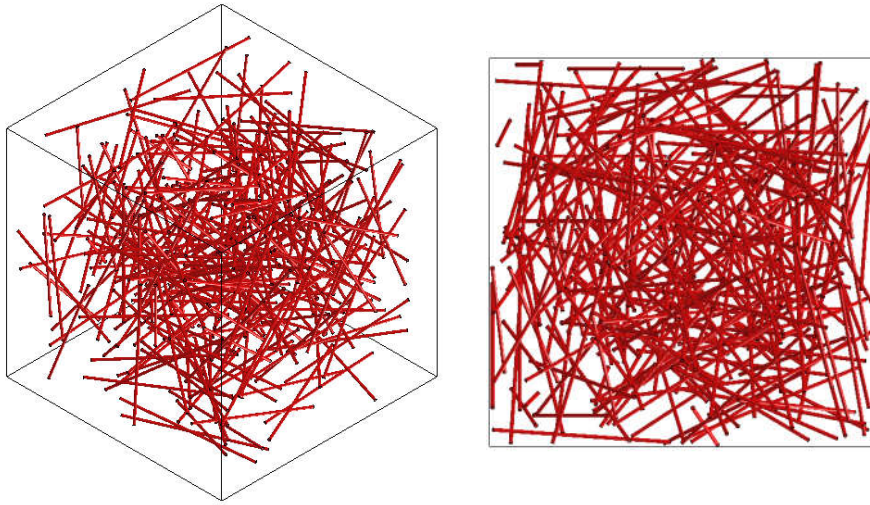


Figure 8-11 25 mm 1% vol. UHPFRC cube with 3D random distribution.

8.3.2 Ansys Workbench analysis and results

Using the '.iges' file generated from Digimat, further geometry modifications can be made using Ansys Workbench, including checking the completeness and dimensions of the model. Due to the existence of fibres, the concrete matrix is not able to be mesh in hexahedral elements, although hexahedral elements can benefit model convergence and increase the simulation accuracy. The overall mesh for the concrete matrix and a fibre can be seen in Figure 8-12.

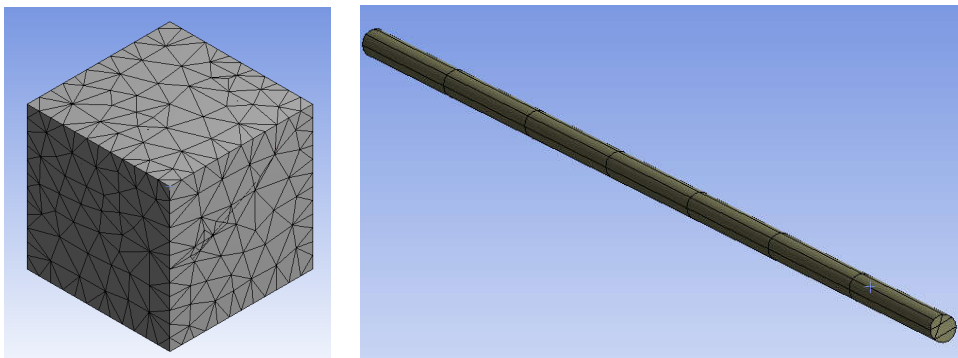


Figure 8-12 Mesh condition of concrete and fibre.

Figure 8-13 shows the tetrahedral elements for the concrete matrix. Some distorted tetrahedral elements with small angles can be seen in the detailed figure on the right. This can be partly solved by decreasing the element size. However, decreasing the element size will largely increase the total number of elements. In this model, there are 508862

nodes and 320070 elements in total. The linear material properties can be seen in Table 8-3. The contact elements are set to be fully bonded initially.

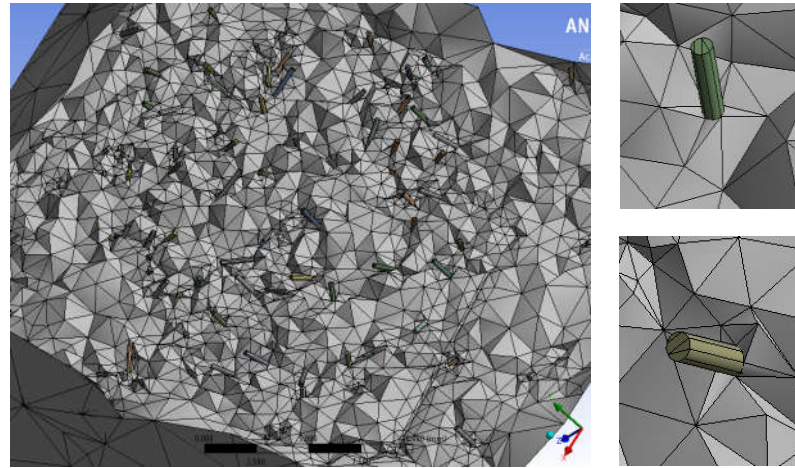


Figure 8-13 General and detailed UHPFRC mesh view.

Table 8-3 Linear material properties used in multiscale modelling.

	Young's modulus (MPa)	Poisson ratio
UHPC	47000	0.2
Fibre	200000	0.3

A compressive strength test was modelled on this 25 mm cube. Figure 8-14 shows the deformation along the Y-axis. This model uses displacement control and the maximum displacement is 0.01 mm.

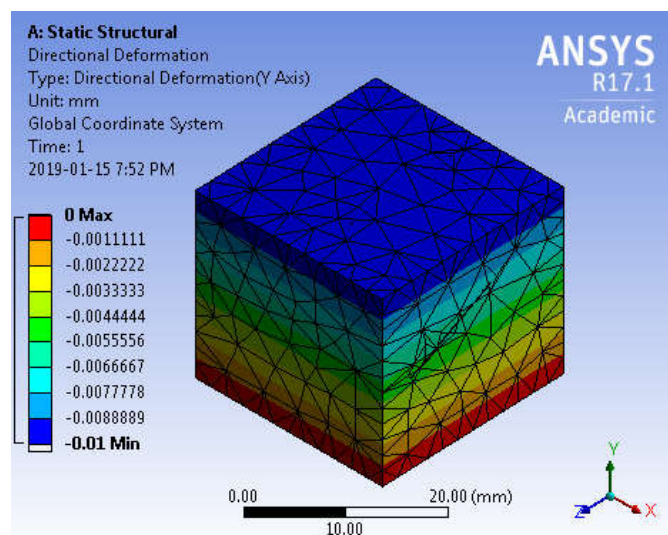


Figure 8-14 Deformation along loading axis (Y-axis) (unit: mm).

Figure 8-15 shows the compressive stress in the concrete matrix. An increase of stress with time can be seen in the picture. Due to the additional fibres, the concrete elements near the fibres are always in a higher stress state (see the enlarged picture in Figure 8-15).

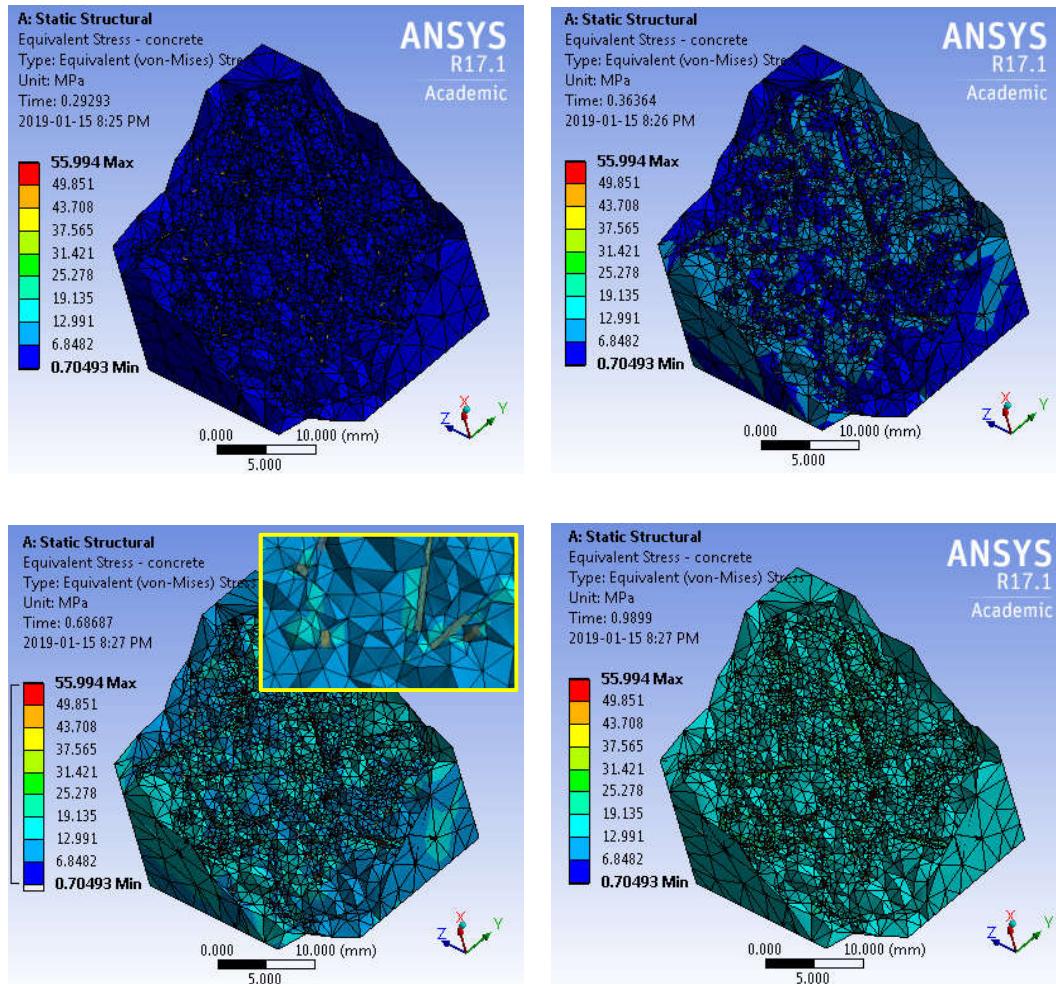


Figure 8-15 Equivalent stress of concrete matrix under different displacement (unit: MPa).

However, only linear modelling was finished in this research, since the following points led to the non-convergence of the model:

1. The complexity of non-linear material properties (e.g., William-Warnke five parameters model, Drucker-Prager model, William-Warnke with BISO model);
2. The contact behaviour between fibres and concrete matrix;
3. The massive amount of fibres give massive amount of nodes and element, especially the distorted concrete elements and contact elements.

Therefore, this method was not further investigated.

8.4 OpenSees FEM Simulation Method

Since multiscale modelling is not applicable, the Open System for Earthquake Engineering Simulation (OpenSees) was used instead. OpenSees is a software framework designed for simulating the seismic response of structural and geotechnical systems. This programme was officially published in 1999, and has been widely used in many universities and institutions in the US, for example, the Pacific Earthquake Engineering Research Center. It can also be applied in steel reinforced concrete structures and bridges. A precise non-linear numerical solution has been proved.

Owing to the sufficient fibre reinforcement, the peak flexural strength is determined by the distribution of fibres. In the literature, researchers had given the relationship between peak uniaxial tensile strength and peak flexural strength. However, this equation is based on the capacity of concrete matrix.

In this research, the three-point bending test was modelled. In OpenSees programme, the input parameters include five parameters from uniaxial compressive test (ϵ_{c1} , ϵ_{c2} , ϵ_{c3} , σ_{c1} , σ_{c2}) and eight parameters from uniaxial tensile test (ϵ_{t1} , ϵ_{t2} , ϵ_{t3} , ϵ_{t4} , σ_{t1} , σ_{t2} , σ_{t3}), which are shown in Figure 8-16.

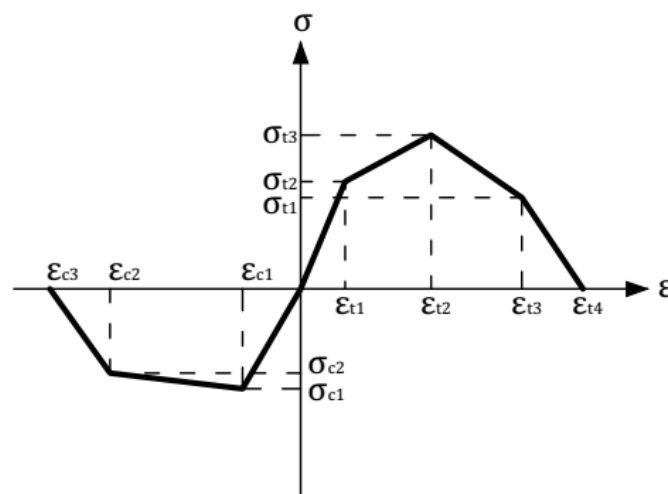


Figure 8-16 Input stress-strain diagram in OpenSees programme.

The data from compressive test results was adopted as the input parameter of compressive part. Since the concrete can hardly reach compressive failure during the three-point bending test, the most critical part is the uniaxial tensile region. ε_{t1} and σ_{t1} refers to the first crack tensile strain and stress.

The specimen completely cracks until no fibre is bridging the crack. According to the French guideline [26], this strain limit point ε_{lim} is defined as:

$$l_c = \frac{2}{3}h \quad \text{Equation 8-6}$$

$$\varepsilon_{lim} = \varepsilon_{t4} = \varepsilon_{el} + \frac{l_f}{4l_c} \quad \text{Equation 8-7}$$

where ε_{el} is the elastic strain limit, l_f is the fibre length, and the characteristic length l_c is related to the specimen height. The simulation is mainly focusing on finding the relationship between the peak flexural strength and uniaxial tensile strength. Therefore, σ_{t2} is the key input parameter.

Here the peak uniaxial tensile strength value for 2% vol. 50° fibre orientation angle is taken as 7.34 MPa, which is also the uniaxial tensile strength for UHPC, since the fibres orientation angle below 50° are not sufficient to generate strain hardening behaviour.

According to previous section, the peak uniaxial tensile strength has a linear relationship with $V_f \cdot \cos(\varphi)$. Therefore, the input uniaxial tensile strength σ_{t2} for a beam specimen with fibre volume content V_f and fibre orientation angle φ can be calculated as:

$$\sigma_{t2} = \frac{f_{t0} \cdot \cos\varphi \cdot V_f}{c} \quad \text{Equation 8-8}$$

where

- f_{t0} first crack tensile strength of concrete matrix (in this simulation $f_{t0} = 7.34$ MPa);
- c fibre efficiency coefficient (in this simulation $c = 2\% \times \cos 50^\circ$).

The fibre efficiency coefficient is determined by the contact behaviour between the concrete and fibre. It means that, the frictional strength produced by 2% vol. UHPFRC

with an orientation angle of 50° is the boundary for strain softening and strain hardening behaviour.

Using the fibre volume content data and fibre orientation angle data from Table 8-2, the peak tensile strength can be calculated using Equation 8-8. By taking the peak uniaxial tensile strength into the OpenSees programme, the peak flexural strength can be simulated. The correlation between the experimental and simulated peak flexural tensile strength can be seen in Figure 8-17. Some factors may cause the shifts of the data points:

1. Data from magnetic probe test is not accurate enough;
2. Concrete may have some local defect caused by air voids or fibre balling;
3. Since pull-out test was not conducted, 2% vol. 50° fibre orientation angle is taken as 7.34 MPa, but it might not be accurate enough.

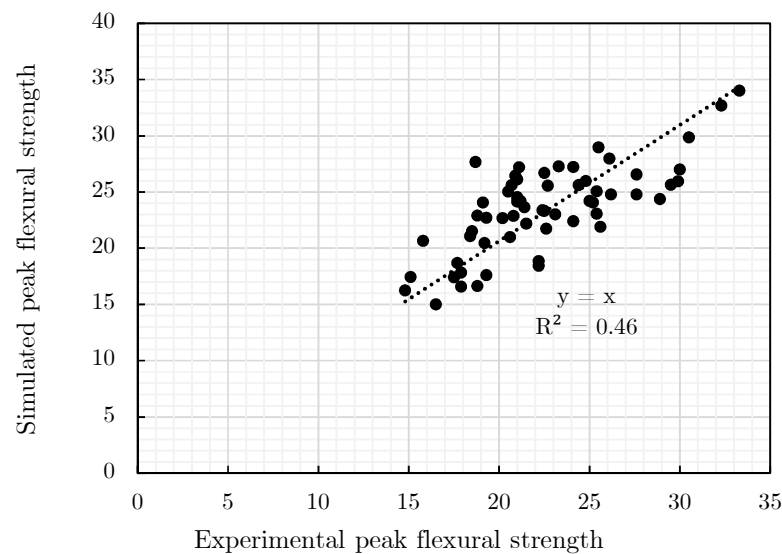


Figure 8-17 Correlation between experimental and simulated peak flexural strength (unit: MPa).

Figure 8-18 shows a comparison between the experimental and OpenSees simulated curves. The deflection data of experimental curve is scaled based on the linear part, since the deflection data was not obtained from load gauge but from the movement of the loading roller. The peak flexural strength is 21.5 MPa, which only has a 0.1 MPa difference compared to the experimental result (22.6 MPa).

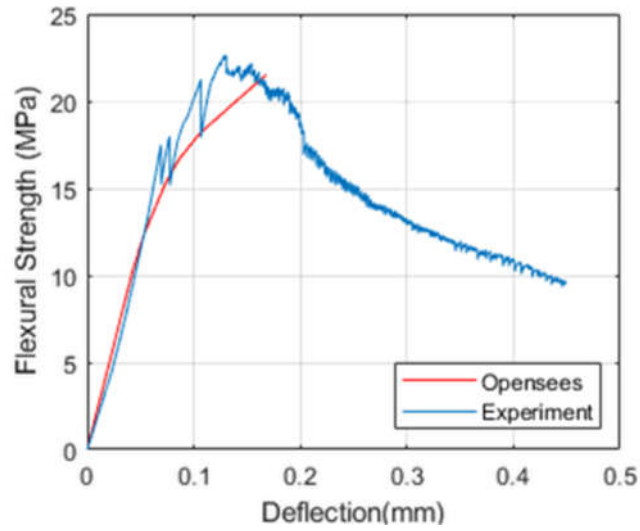


Figure 8-18 Comparison of stress-deflection curve of 2%-20-s1 experimental and OpenSees simulated results.

From the simulation, a relationship between the output peak uniaxial tensile strength f_t and the input peak flexural strength f_f can be given as:

$$f_f = 2.66f_t - 0.1 \quad [\text{unit: MPa}] \quad \text{Equation 8-9}$$

CHAPTER 9 CONCLUSIONS AND FUTURE WORKS

Refer to the objectives stated in Chapter 1.3, some significant findings in this research are listed. Apart from conclusions obtained from fibre distribution test and mechanical test, some suggestions for manufacturers are also recommended. The limitations of this research are also stated. Based on the limitations, some recommendations and suggestions are given for future research.

9.1 Conclusions

In this research, the objectives stated in Section 1.3 are successfully completed. The results for this research can be concluded as:

1. A cylindrical permanent magnetic test was invented. This test can distinguish the fibre volume content distribution between 0.5%, 1%, and 2% vol. However, the repeatability of this test was not ideal. Moreover, the fibre orientation cannot be tested. Thus, this method was not used in later research;
2. The effective depth of the C-shape magnetic probe was investigated. Test results shows that the attenuation of magnetic permeability has an exponential relationship with increase of testing depth. The efficiency drops below 10% after 24 mm. This result is further proved by using image analysis method. Equations have been given based on the attenuation factor, to alter the relative magnetic permeability value, and to correlate this value with fibre volume content;
3. The vibration during concrete casting can cause the segregation of steel fibres. For self-compacted UHPFRC without vibration, no fibre segregation phenomenon can be observed. The segregation ratio for 2% and 3% vol. UHPFRC specimens are 1.225 and 1.209;
4. The distribution of fibre orientation angle follows a normal distribution. The fibre orientation angles between 40-50° accounts for 29% of the total. Since the fibre orientation angle is also affected by other factors like mould boundary and casting

procedure, this fibre orientation angle distribution is only applied for slab casting with concrete poured from the specimen's centre;

5. The compressive strength has a huge increase of 47 MPa when adding 1% vol. steel fibres. The post-cracking performance changes from brittle to ductile because fibres restraint the concrete matrix from exploding;
6. The peak uniaxial tensile strength and peak flexural strength not only depends on the material properties of concrete matrix, but also the fibre volume content and fibre orientation angle. After the concrete cracks, if the fibre amount is low or the fibre orientation angle is large, there is no strain hardening performance. Therefore, the peak strength is still related to the tensile property of the concrete matrix. If the fibre amount is high or with a small fibre orientation angle, strain hardening behaviour occurs. The peak uniaxial tensile strength has a linear relationship with the $\cos(\varphi)$ value or the fibre volume content;
7. The experimental result was further simulated and correlated using the OpenSees software. A linear relationship can be found between peak uniaxial tensile strength and peak flexural strength;
8. Both economically and mechanically thinking, it is not recommended to over-dose the fibres because it may cause non-uniform fibre distribution and early concrete cracking. The improvement of tensile behaviour can be achieved by adjusting the orientation angle rather than simply increasing the fibre volume content.

9.2 Future Works

Generally, both the fibre distribution test results and mechanical test results have some variances. Some recommendations for future works can be concluded as:

1. The testing depth of the magnetic probe is limited. If this method is going to be used in industry for quality control purpose, a deeper effective depth is required. A magnetic with bigger ferrite core and more wrapped coils could be considered;

2. To improve the quality of the cutting surface, a better concrete cutter can be considered. In this case, not only the fibre amount but also the orientation of fibres can be determined;
3. A more accurate extensometer is needed for uniaxial tensile test because strain gauges are not reliable after the concrete cracks;
4. Non-ferromagnetic mould can be considered for uniaxial tensile test, so the magnetic probe can be applied without the influence of steel moulds;
5. Single fibre pull out tests can be considered to obtain the static frictional force and sliding frictional force under different circumstances. The fibre orientation angle and fibre coating material are both important factors to be investigated.

REFERENCES

- [1] M. P. Pearson, “Stonehenge: Exploring The Greatest Stone Age Mystery,” *Current Archaeology*, pp. 20-27, 2012.
- [2] W. S. Chung, “Self-Sensing of Flexural Strain and Damage in Carbon Fibre Polymer-Matrix Composite by Electrical Resistance Measurement,” *Carbon*, vol. 44, no. 13, pp. 2739-2751, 2006.
- [3] MOHURD, “GB50010-2010 Code for Design of Concrete Structures,” MOHURD, 2015.
- [4] C. Shi and Y. L. Mo, *High-Performance Construction Materials Science and Applications*, Danvers: World Scientific, 2008.
- [5] ACI Committee 239, “Ultra-High Performance Concrete: An Emerging Technology Report,” American Concrete Institute, 2018.
- [6] N. Raj, S. G. Patil and B. Bhattacharjee, “Concrete Mix Design by Packing Density Method,” *Journal of Mechanical and Civil Engineering*, vol. 11, no. 2, pp. 34-46, 2014.
- [7] E. Fehling, M. Schmidt, J. Walraven, T. Leutbecher and S. Fröhlich, *Ultra-High Performance Concrete UHPC: Fundamentals, Design, Examples*, Berlin: Wilhelm Ernst & Sohn, 2011.
- [8] SINTEF Building and Infrastructure, “Ultra High Performance Fibre Reinforced Concrete (UHPC) – State of The Art,” COIN Project report, 2012.
- [9] J. Scheydt and H. Müller, “Microstructure of Ultra High Performance Concrete (UHPC) and Its Impact on Durability,” in *Ultra High Performance Concrete and Nanotechnology in Construction, 3rd International Symposium on Ultra High Performance Concrete and Nanotechnology for High Performance Construction Materials*, Kassel, 2012.
- [10] D. Heinz, L. Urbonas and T. Gerlicher, “Effect of Heat Treatment Method on The Properties of UHPC,” in *Ultra High Performance Concrete and Nanotechnology in Construction*, 2012.

- [11] A. M. Brandt, "Fibre Reinforced Cement-based (FRC) Composites after over 40 Years of Development in Building and Civil Engineering," *Composite Structures*, vol. 83, no. 13, pp. 3-9, 2008.
- [12] J. Romualdi and G. Baston, "Mechanics of Crack Arrest in Concrete," *Journal of the Engineering Mechanics Division*, vol. 89, pp. 147-168, 1963.
- [13] J. P. Romualdi and J. A. Mandel, "Tensile Strength of Concrete Affected by Uniformly Distributed and Closely Spaced Short Lengths of Wire Reinforcement," *ACI Structural Journal*, vol. 61, pp. 27-37, 1964.
- [14] National Precast Concrete Association, "Ultra High Performance Concrete (UHPC) Guide to Manufacturing Architectural Precast UHPC Elements," National Precast Concrete Association, Carmel, 2013.
- [15] R. Bornemann and S. Faber, "UHPC with Steel- and Non-corroding High-Strength Polymer Fibres under Static and Cyclic Loading," in *Ultra High Performance Concrete (UHPC), Intl. Symp. on Ultra High Performance Concrete*, Kassel, 2004.
- [16] T. Kanstad, "Forslag til Retningslinjer for Dimensjonering, Utførelse Ogkontroll av Fiberarmerte Betongkonstruksjoner," COIN Project report 29, SINTEF Building and Infrastructure, 2011.
- [17] I. Markovic, "High-Performance Hybrid-Fibre Concrete - Development and Utilisation. Dissertation Delft University of Technology, DPU Science," Delft University Press, Delft, 2006.
- [18] DIN EN 14889-1:2006-11, "Fibres for Concrete - Part 1 :Steel Fibres - Definitions Specifications and Conformity," German Version EN 14889-1:2006, 2006.
- [19] A. M. Tahwia, "Performance of Ultra-High Performance Fiber Reinforced Concrete at High Temperatures," *International Journal of Engineering and Innovative Technology*, vol. 6, no. 10, 2017.
- [20] P. Rossi, "Ultra-High-Performance Fiber-Reinforced Concretes," *Concrete International*, vol. 23, no. 12, pp. 46-52, 2001.
- [21] A. Benture and S. Mindess, *Fibre Reinforced Cementitious Composites*, Routledge, 2006.
- [22] P. C. Aitcin and P. Richard, "The Pedestrian/Bikeway Bridge of Sherbrooke," in *Proceedings of 4th International Symposium on Utilization of High-Strength/High-Performance Concrete*, Paris, 1996.

- [23] P. Y. Blais and M. Couture, "Precast, Prestressed Pedestrian Bridge - World's First Reactive Powder Concrete Structure," *PCI Journal*, vol. 44, no. 5, pp. 60-71, 1999.
- [24] M. Rebentrost and G. Wight, "Experience and Applications of Ultra-High Performance Concrete in Asia," in *2nd International Symposium on Ultra-High Performance Concrete, Structural Material & Engineering Series*, Kassel, 2008.
- [25] T. Kono, T. Ichinomiya and T. Ohno, "Influence of Placing Methods on Structural Performance of Slab with Ultra High Strength Fiber Reinforced Concrete - Tokyo International Airport Runway D," in *8th International Symposium on Utilization of High-Strength and High Performance Concrete*, Tokyo, 2008.
- [26] Association Française de Génie Civil (AFGC), "Documents Scientifiques et Techniques: Bétons Fibrés à Ultra-Hautes Performances (Recommandations Provisoires)," Association Française de Génie Civil (AFGC), 2013.
- [27] E. Fehling, M. Schmidt, T. Teichmann, K. Bunje, R. Bornemann and B. Middendorf, "Entwicklung, Dauerhaftigkeit and Berechnung Ultra-Hochfester Bestone (UHPC) [Development, Durability and Design of UHPC]. dfg Research Report fe-497/1-1, Structural Materials & Engineering Series," Kassel University Press, Kassel, 2005.
- [28] M. Schmidt, K. Bunje and F. Dehn, "Sachstandsbericht Ultraochfester Beston [UHPC - State of The Art Report]," Beuth Verlag GmbH, Berlin, 2008.
- [29] N. Tue and F. Dehn, "Compostie Elements Made of Steel Tubes and Ultrahigh Strength Concrete as Motor of Innovation," Leipzig University, Final Report to Bilginger Berger AG, 2004.
- [30] A. M. Hassan, S. W. Jones and G. H. Mahmud, "Experimental Test Methods to Determine The Uniaxial Tensile and Compressive Behaviour of Ultra High Performance Fibre Reinforced Concrete (UHPRFC)," *Construction and Building Materials*, vol. 37, pp. 874-882, 2012.
- [31] T. Leutbecher, "Rissbildung und Zugtragverhalten von mit Stabstahl und Fasern bewehrtem Ultrahochfesten Beton (UHPC) [Crack Formation and Tensile Load-Bearing Behaviour of UHPC Reinforced with Steel Bars and Fibres]. Dissertation," Kassel University Press GmbH, Kassel, 2008.
- [32] A. Abrishambaf, M. Pimentel and S. Nunes, "Influence of fibre orientation on the tensile behaviour of ultra-high performance fibre reinforced cementitious composites," *Cement and Concrete Research*, vol. 96, pp. 28-40, 2017.

- [33] V. Li and C. Leung, “Steady-State and Multiple Cracking of Short Random Fiber Composites,” *Journal of Engineering Mechanics*, vol. 188, no. 11, pp. 2246-2264, 1992.
- [34] T. Pfyl, “Tragverhalten von Stahlfaserbeton [Structural Behaviour of Steel Fibre-Reinforced Concrete. Dissertation,” ETH No. 15005, Zurich, 2003.
- [35] J. Jungwirth, “Zum Zugtragverhalten von Zugbeanspruchten Bauteilen aus Ultra-Hochleistungs-Faserbeton [on The Tensile Loadbearing Behaviour of Fibre-reinforced UHPC Components in Tension]. Dissertation Thesis,” École Polytechnique Fédérale de Lausanne (EPFL), 2006.
- [36] Eurocode, “Eurocode 2: Design of Concrete Structures - Part 1-1 : General Rules and Rules for Buildings,” Eurocode, 2004.
- [37] FIB, CEB-FIP Model Code 90, London: Thomas Telford Ltd, 1993.
- [38] K. H. Reineck and S. Greiner, “Tests on Ultra-High Performance Fibre Reinforced Concrete for Designing Hot-Water Tanks and UHPFRC-Shells,” in *Ultra High Performance Concrete (UHPC), International Symposium on Ultra High Performance Concrete*, Kassel, 2004.
- [39] MSC Software, “Digimat Documentation Manual Handbook,” MSC Software Company, Belgium, 2014.
- [40] İ. Şanal and N. Özyurt Zihnioglu, “To What Extent Does The Fiber Orientation Affect Mechanical Performance?,” *Construction and Building Material*, pp. 671-681, 2013.
- [41] J. Aveston and A. Kelly, “Theory of Multiple Fracture of Fibrous Composites,” *Journal of Materials Science*, pp. 352-362, 1973.
- [42] D. Dupont and L. Vandewalle, “Distribution of Steel Fibres in Rectangular Sections,” *Cement and Concrete Composites*, pp. 391-398, 2005.
- [43] K. Kobayashi, *Fiber Reinforced Concrete*, Tokyo: Ohm-Sha, 1981.
- [44] S. T. Kang, B. Y. Lee, J. K. Kim and Y. Y. Kim, “The Effect of Fibre Distribution Characteristics on the Flexural Strength of Steel Fibre-Reinforced Ultra High Strength Concrete,” *Construction and Building Materials*, pp. 2450-2457, 2011.
- [45] V. C. Li, “Tailoring ECC for Special Attributes: A Review,” *International Journal of Concrete Structures and Materials*, vol. 6, no. 3, pp. 135-144, 2012.

- [46] D.-Y. Yoo, S.-T. Kang and Y.-S. Yoon, “Effect of Fiber Length and Placement Method on Flexural Behavior, Tension-Softening Curve, and Fiber Distribution Characteristics of UHPFRC,” *Construction and Building Materials Journal*, vol. 64, pp. 67-81, 2014.
- [47] D. Koker De and G. van Zijl, “Extrusion of Engineered Cement-Based Composite Material,” in *Proceedings 6th RILEM symposium on FRC*, Varenna, 2004.
- [48] Ganzhou Daye Metallic Fibres Co..Ltd, “Ganzhou Daye Fibre Dispersion Machine,” Ganzhou Daye Metallic Fibres Co..Ltd, [Online]. Available: <http://www.gzdymf.com/index.php/pro/show/id/125>. [Accessed 09 01 2019].
- [49] G. B. Jeffery, “The Motion of Ellipsoidal Particles Immersed in A Viscous Fluid,” 1922, pp. 161-179.
- [50] M. A. Bibbo, S. M. Dhin and R. C. Armstrong, “Shear Flow Properties of Semiconcentrated Fiber Suspensions,” *Journal of Rheology*, vol. 29, no. 6, p. 905–929, 1985.
- [51] B. Boulekbache, M. Hamrat, M. Chemrouk and S. Amziane, “Influence de la Rheologie des Bétons Renforcés de Fibres Métalliques sur Leurs Propriétés Mécaniques,” *European journal of environmental and civil engineering*, vol. 26, no. 13, pp. 473-488, 2009.
- [52] N. Ozyurt, T. O. Mason and S. P. Shah, “Non-Destructive Monitoring of Fiber Orientation Using AC-IS: An Industrial-Scale Application,” *Cement and Concrete Research*, vol. 36, no. 9, pp. 1653-1660, 2006.
- [53] A. Blanco, P. Pujadas, A. de la Fuente, S. Cavalaro and A. Aguado, “Assessment of The Fibre Orientation Factor in SFRC Slabs,” *Composites: Part B*, vol. 68, pp. 343-354, 2014.
- [54] S. Barnett, J.-F. Lataste, T. Parry, S. Millard and M. Soutsos, “Assessment of Fibre Orientation in Ultra High Performance Fibre Reinforced Concrete and Its Effect on Flexural Strength,” *Materials & Structures*, vol. 43, no. 7, p. 1009–1023, 2010.
- [55] S. Grünewald, “Performance-based Design of Self-Compacting Fibre Reinforced Concrete,” Doctoral Thesis, Delft University of Technology, Delft, 2004.
- [56] B. Boulekbache, M. Hamrat, M. Chemrouk and S. Amziane, “Flowability of Fibre Reinforced Concrete and Its Effect on the Mechanical Properties of The Material,” *Construction and Buildings Materials*, vol. 24, no. 9, pp. 1664-1671, 2010.

- [57] W. Meng and K. H. Khayat, "Improving Flexural Performance of Ultra-high-performance Concrete Rheology Control of Suspending Mortar," *Composites Part B*, vol. 117, pp. 26-34, 2017.
- [58] R. Kameswara, "Effectiveness of Random Fibres in Composites," *Cement and Concrete Research*, vol. 9, no. 6, pp. 685-693, 1979.
- [59] L. Martinie and N. Roussel, "Simple Tools for Fiber Orientation Prediction in Industrial Practice," *Cement and Concrete Research*, vol. 41, no. 10, pp. 993-1000, 2011.
- [60] O. Švec, G. Žirgulis, J. E. Bolander and H. Stang, "Influence of Formwork Surface on The Orientation of Steel Fibres within Self-compacting Concrete and on The Mechanical Properties of Cast Structural Elements," *Cement & Concrete Composites*, vol. 50, pp. 60-72, 2014.
- [61] J. Edington and D. J. Hannant, "Steel Fibre Reinforced Concrete. The effect on Fibre Orientation of Compaction by Vibration," *Materials and Structures*, vol. 41, no. 2, pp. 41-44, 1972.
- [62] R. Gettu, D. R. Gardner, H. Saldívar and B. E. Barragán, "Study of The Distribution and Orientation of Fibres in SFRC Specimens," *Materials and Structures*, vol. 38, no. 1, pp. 31-37, 2005.
- [63] F. Laranjeira, A. Agurado, C. Molins, S. Grünewald, J. Walraven and S. Cavalaro, "Framework to Predict The Orientation of Fibers in FRC: A Novel Philosophy," *Cement & Concrete Research*, vol. 42, no. 6, pp. 752-768, 2012.
- [64] P. Soroushian and C. Lee, "Distribution and Orientation of Fibers in Steel Fiber Reinforced Concrete," *ACI Material Journal*, vol. 87, no. 5, pp. 433-439, 1990.
- [65] A. Kooiman, "Modelling Steel Fibre Reinforced Concrete for Structural Design," PhD Thesis, University of Ghent, Belgium, 2000.
- [66] E. Yang, M. Sahmaran, Y. Yang and V. Li, "Rheological Control in The Production of Engineered Cementitious Composites," *ACI Material Journal*, vol. 106, no. 4, pp. 357-366, 2009.
- [67] J. Zhou, S. Qian, G. Ye, O. Copuroglu, K. v. Breugel and V. C. Li, "Improved Fiber Distribution and Mechanical Properties of Engineered Cementitious Composites by Adjusting The Mixing Sequence," *Cement and Concrete Composites*, vol. 34, no. 3, pp. 342-348, 2012.

- [68] L. Vandewalle, G. Heirman and F. Rickstal, "Fibre Orientation in Self-Compacting Fibre Reinforced Concrete," in *Proceedings of 7th International RILEM Symposium on Fibre Reinforced Concrete*, Chennai, India, 2008.
- [69] J. Liu, C. Li, J. Liu, G. Cui and Z. Yang, "Study on 3D Spatial Distribution of Steel Fibers in Fiber Reinforced Cementitious Composites through Micro-CT Technique," *Construction & Building Materials*, vol. 48, no. 19, pp. 656-661, 2013.
- [70] X. Sun, J. Lasecki, D. Zeng, Y. Gan, X. Su and T. Jie, "Measurement and Quantitative Analysis of Fiber Orientation Distribution in Long Fiber Reinforced Part by Injection Molding," *Polymer Testing*, vol. 42, pp. 168-174, 2015.
- [71] B. Felekolu, K. Tosun-Felekolu and E. Gödek, "A Novel Method for The Determination of Polymeric Micro-Fiber Distribution of Cementitious Composites Exhibiting Multiple Cracking Behavior under Tensile Loading," *Construction & Building Material*, vol. 86, pp. 85-94, 2015.
- [72] N. Sebaibi, M. Benzerzour and N. E. Abriak, "Influence of The Distribution and Orientation of Fibres in A Reinforced Concrete with Waste Fibres and Powders," *Construction & Building Materials*, vol. 65, pp. 254-263, 2014.
- [73] R. Deeb, B. L. Karihaloo and S. Kulasegaram, "Reorientation of Short Steel Fibres during The Flow of Self-Compacting Concrete Mix and Determination of The Fibre Orientation Factor," *Cement & Concrete Research*, vol. 56, pp. 112-120, 2014.
- [74] J. Xia and K. Mackie, "Axisymmetric Fiber Orientation Distribution of Short Straight Fiber in Fiber-Reinforced Concrete," *ACI Material Journal*, vol. 111, no. 2, pp. 112-120, 2014.
- [75] D. G. Asheley, "Measurement of Glass Content in Fibre/Cement Composites by X-ray Fluorescence Analysis," *Ndt International*, vol. 12, no. 2, pp. 56-60, 1979.
- [76] A. C. Bordelon and J. R. Roesler, "Spatial Distribution of Synthetic Fibers in Concrete with X-ray Computed Tomography," *Cement & Concrete Composites*, vol. 53, pp. 35-43, 2014.
- [77] T. Ponikiewski, J. Goaszewski, M. Rudzki and M. Bugdol, "Determination of Steel Fibres Distribution in Self-Compacting Concrete Beams Using X-Ray Computed Tomography," *Archives of Civil & Mechanical Engineering*, vol. 15, no. 2, pp. 558-568, 2015.

- [78] A. Peled, J. M. Torrents, T. O. Mason, S. P. Shah and E. J. Garboczi, "Electrical Impedance Spectra to Monitor Damage during Tensile Loading of Cement Composites," *ACI Materials Journal*, vol. 98, no. 4, pp. 313-322, 2001.
- [79] B. J. Christensen, T. Coverdale, R. Olson, S. J. Ford, E. J. Garboczi, H. M. Jennings and T. O. Mason, "Impedance Spectroscopy of Hydrating Cement-Based Materials: Measurement, Interpretation, and Application," *Journal of the American Ceramic Society*, vol. 77, no. 11, pp. 2789-2804, 1994.
- [80] L. Y. Woo, S. Wansom, N. Ozyurt, B. Mu and S. P. Shah, "Characterizing Fiber Dispersion in Cement Composites Using AC-Impedance Spectroscopy," *Cement and Concrete Composites*, vol. 27, no. 6, pp. 627-636, 2005.
- [81] J. M. Torrents, T. O. Mason, A. Peled, S. P. Shah and E. J. Garboczi, "Analysis of The Impedance Spectra of Short Conductive Fiber-Reinforced Composites," *Journal of Material Science*, vol. 36, no. 16, pp. 4003-4012, 2001.
- [82] M. A. Campo, L. Y. Woo, T. O. Mason and E. J. Garboczi, "Frequency-Dependent Electrical Mixing Law Behavior in Spherical Particle Composites," *Journal of Electroceramics*, vol. 9, no. 1, pp. 49-56, 2002.
- [83] S. Cavalaro, L. R. J. Torrents and A. Aguado, "Improved Assessment of Fibre Content and Orientation with Inductive Method in SFRC," *Material Structures*, vol. 48, p. 2859, 2014.
- [84] J. Torrents, A. Blanco, P. Pujadas, A. Aguado, P. Juan and M. Sánchez, "Inductive Method for Assessing The Amount and Orientation of Steel Fibre in Concrete," *Materials and Structures (RILEM)*, vol. 45, no. 10, pp. 1577-1592, 2012.
- [85] S. Van Damme, A. Franchois, D. De Zutter and L. Taerwe, "Nondestructive Determination of The Steel Fiber Content in Concrete Slabs with An Open-ended Coaxial Probe," *IEEE Transactions on Geoscience & Remote Sensing*, vol. 42, no. 11, pp. 2511-2521, 2004.
- [86] J. M. Torrents, P. Juan-García, O. Patau and A. Aguado, "Surveillance of Steel Fibre Reinforced Concrete Slabs Measured with An Open-Ended Coaxial Probe," *XIX Imeko World Congress Fundamental & Applied Metrology Proceedings*, pp. 2282-2284, 2009.
- [87] M. Faifer, R. Ottoboni and S. Toscani, "A Compensated Magnetic Probe for Steel Fiber Reinforced Concrete Monitoring," *Proceedings of IEEE Sensors*, pp. 698-703, 2010.

- [88] S. Nunes, M. Pimentel and A. Carvalho, “Non-Destructive Assessment of Fibre Content and Orientation in UHPFRC Layers Based on A Magnetic Method,” *Cement and Concrete Composites*, vol. 72, pp. 66-79, 2016.
- [89] MOHURD, “Code for Concrete Admixture Application,” China Architecture & Building Press, Beijing, 2013.
- [90] Y. Wang, “Calculation of Magnetic Force of Permanent Magnet Devices,” *Journal of Magnetic Materials and Devices*, vol. 38, no. 5, pp. 49-60, 2007.
- [91] MOHURD, “GB/T50081-2002 Standard for Test Method of Mechanical Properties on Ordinary Concrete,” MOHURD, Beijing, 2002.
- [92] SIA 2052-2016, “Recommendation: Ultra-High Performance Fibre Reinforced Cement Based Composites (UHPFRC),” Switzerland, 2016.
- [93] A. M. Neville, *Properties of Concrete*, Essex: Pearson, 1995.
- [94] The Concrete Society, “Technical Report 34 Concrete Industrial Groud Floors A Guide to Design and Construction,” The Concrete Society, Surrey, 2015.

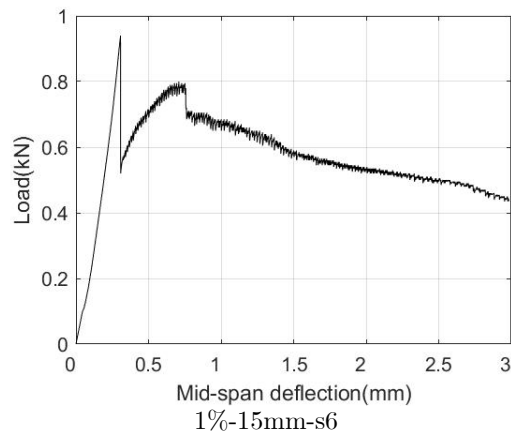
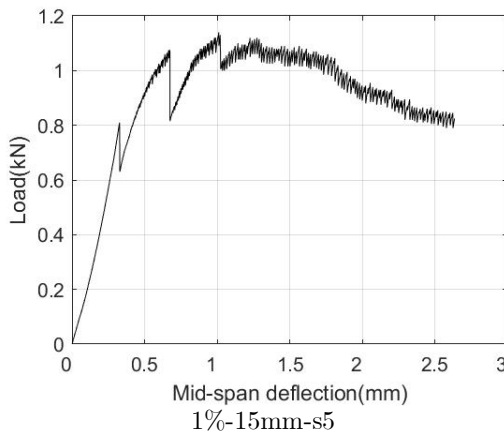
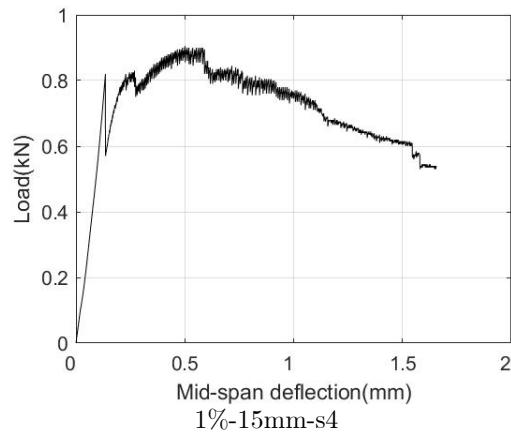
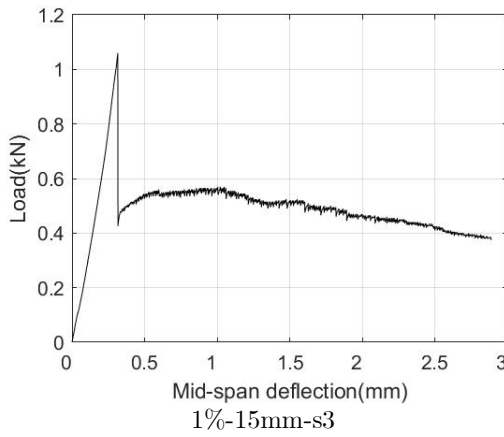
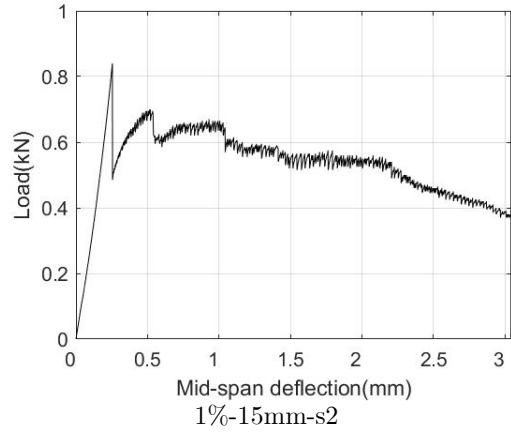
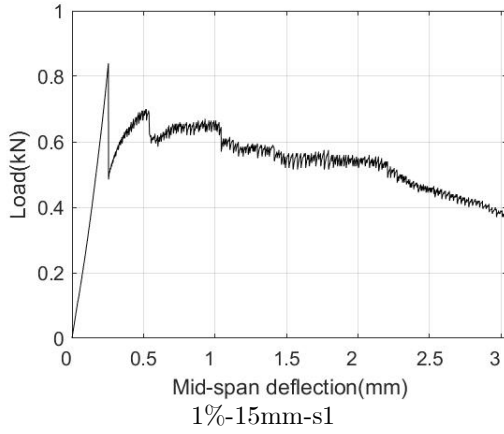
APPENDICES

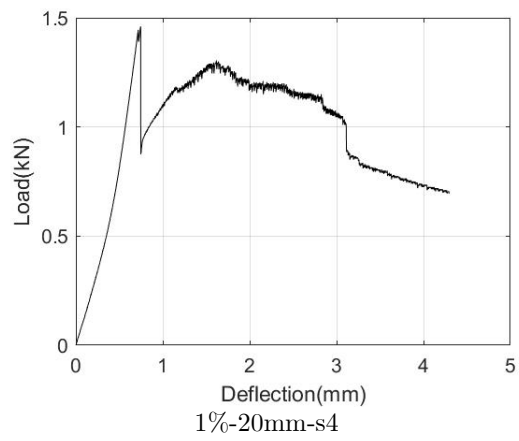
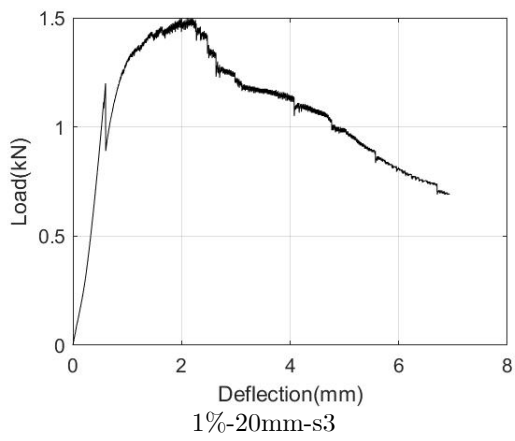
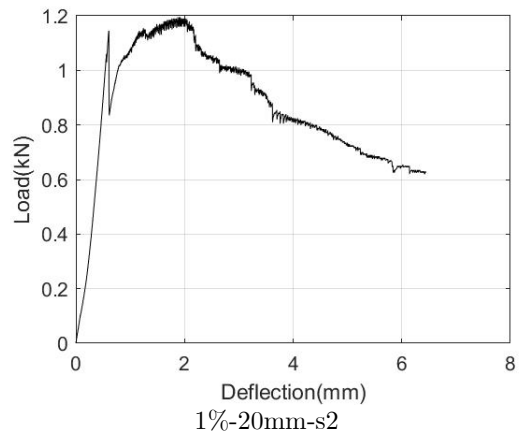
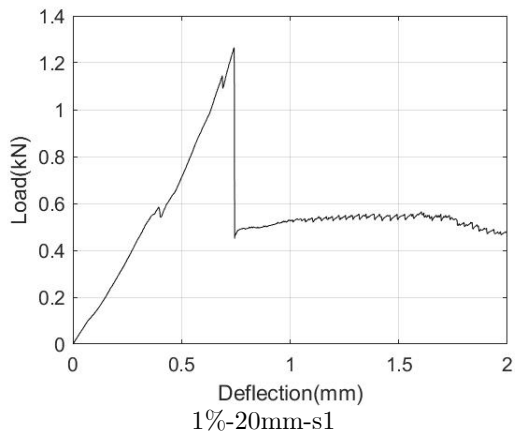
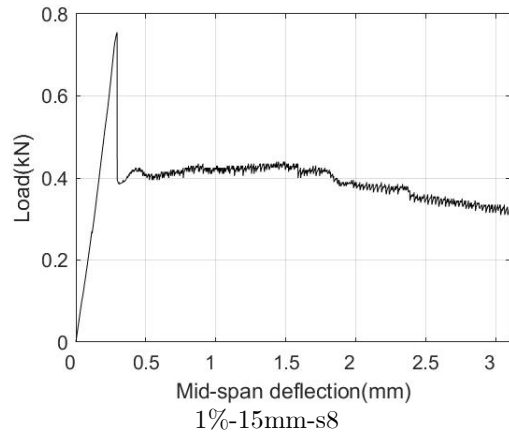
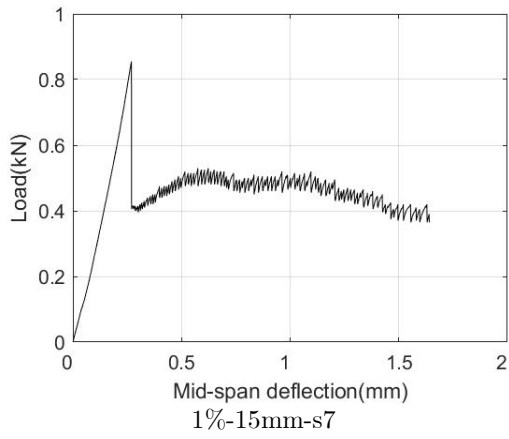
Appendix 1 Total Specimen List

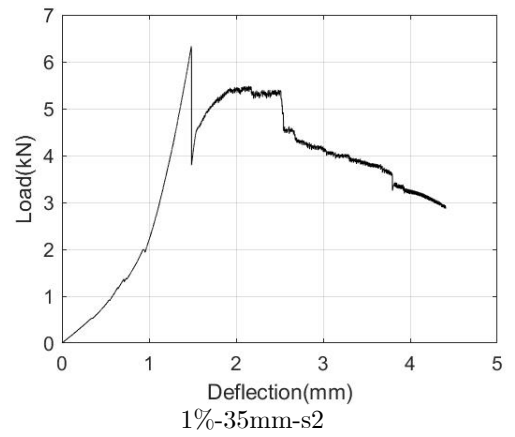
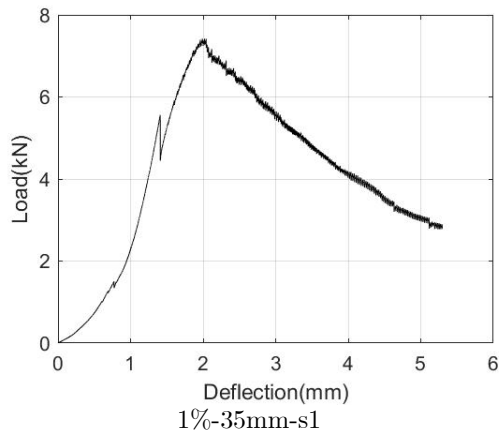
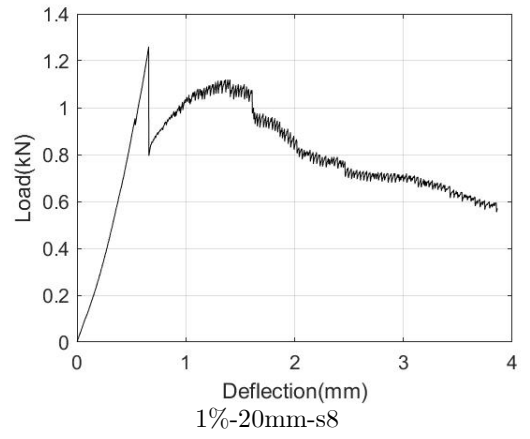
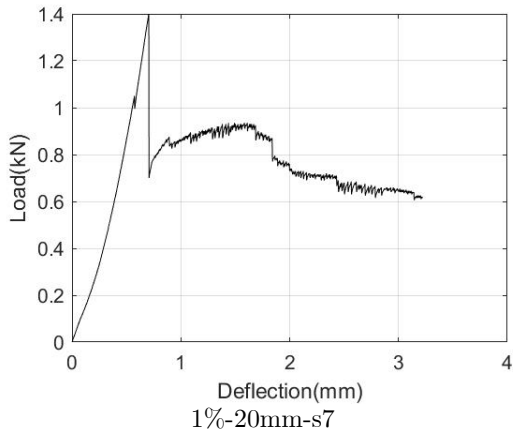
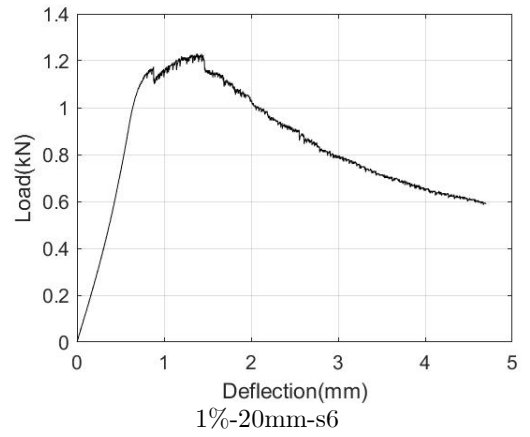
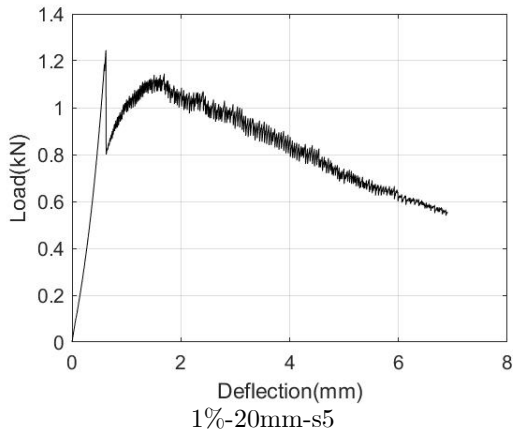
Mix design method	Fibre volume content	Shape	Size(mm)	Vibration	Treatment	Amount	Casting purpose
SD	0.5%	Slab	160×160×10	No	90°C water curing, 48hrs	1	Permanent magnet test
SD	1%	Slab	160×160×10	No	90°C water curing, 48hrs	1	Permanent magnet test
SD	2%	Slab	160×160×10	No	90°C water curing, 48hrs	1	Permanent magnet test
SD	2%	Cylinder	D100, H200	No	90°C water curing, 48hrs	6	Compressive test
SD	2%	Cube	100×100×100	No	90°C water curing, 48hrs	6	Compressive test
SD	2%	Beam	75×75×450	Yes	90°C water curing, 48hrs	6	Inductive test, bending test
SD	2%	Beam	75×75×450	No	90°C water curing, 48hrs	6	Inductive test, bending test
SD	3%	Cylinder	D100, H200	No	90°C water curing, 48hrs	6	Compressive test
SD	3%	Cube	100×100×100	No	90°C water curing, 48hrs	6	Compressive test
SD	3%	Beam	75×75×450	Yes	90°C water curing, 48hrs	6	Inductive test, bending test
SD	3%	Beam	75×75×450	No	90°C water curing, 48hrs	6	Inductive test, bending test
Pre-mix	0	Cube	100×100×100	No	90°C steam curing, 48hrs	6	Compressive test
Pre-mix	0	Slab	500×500×15	No	90°C steam curing, 48hrs	1	Bending test
Pre-mix	0	Slab	500×500×20	No	90°C steam curing, 48hrs	1	Bending test
Pre-mix	0	Slab	500×500×35	No	90°C steam curing, 48hrs	1	Bending test
Pre-mix	0	Slab	500×500×50	No	90°C steam curing, 48hrs	1	Bending test
Pre-mix	1%	Cube	100×100×100	No	90°C steam curing, 48hrs	6	Compressive test
Pre-mix	1%	Dog bone	380×150×50	No	90°C steam curing, 48hrs	3	Inductive test, direct tensile test

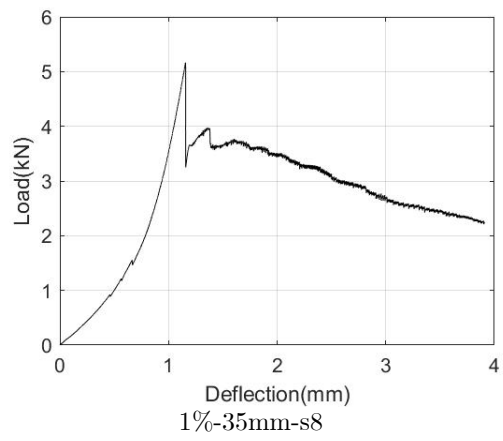
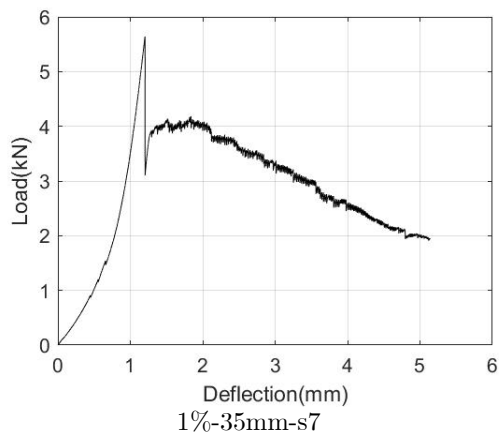
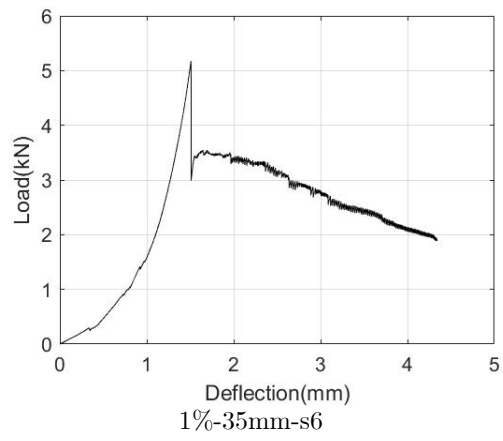
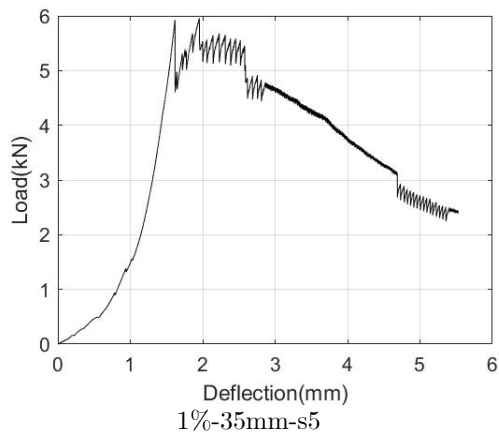
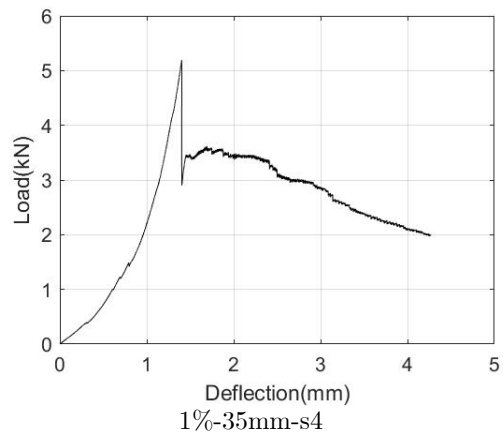
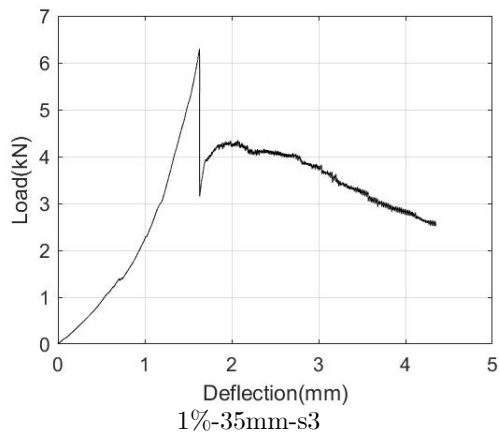
Pre-mix	1%	Beam	100×100×400	No	90°C steam curing, 48hrs	4	Inductive test, bending test
Pre-mix	1%	Slab	500×500×15	No	90°C steam curing, 48hrs	1	Inductive test, bending test
Pre-mix	1%	Slab	500×500×20	No	90°C steam curing, 48hrs	1	Inductive test, bending test
Pre-mix	1%	Slab	500×500×35	No	90°C steam curing, 48hrs	1	Inductive test, bending test
Pre-mix	1%	Slab	500×500×50	No	90°C steam curing, 48hrs	1	Inductive test, bending test
Pre-mix	2%	Cube	100×100×100	No	90°C steam curing, 48hrs	6	Compressive test
Pre-mix	2%	Dog bone	380×150×50	No	90°C steam curing, 48hrs	6	Inductive test, direct tensile test
Pre-mix	2%	Beam	100×100×400	No	90°C steam curing, 48hrs	4	Inductive test, bending test
Pre-mix	2%	Slab	500×500×15	No	90°C steam curing, 48hrs	1	Inductive test, bending test
Pre-mix	2%	Slab	500×500×20	No	90°C steam curing, 48hrs	1	Inductive test, bending test
Pre-mix	2%	Slab	500×500×35	No	90°C steam curing, 48hrs	1	Inductive test, bending test
Pre-mix	2%	Slab	500×500×50	No	90°C steam curing, 48hrs	1	Inductive test, bending test
Pre-mix	2.5%	Cube	100×100×100	No	90°C steam curing, 48hrs	6	Compressive test
Pre-mix	2.5%	Beam	100×100×400	No	90°C steam curing, 48hrs	4	Inductive test, bending test
Pre-mix	2.5%	Slab	500×500×15	No	90°C steam curing, 48hrs	1	Inductive test, bending test
Pre-mix	2.5%	Slab	500×500×20	No	90°C steam curing, 48hrs	1	Inductive test, bending test
Pre-mix	2.5%	Slab	500×500×35	No	90°C steam curing, 48hrs	1	Inductive test, bending test
Pre-mix	2.5%	Slab	500×500×50	No	90°C steam curing, 48hrs	1	Inductive test, bending test
Pre-mix	5%	Cube	100×100×100	No	90°C steam curing, 48hrs	6	Compressive test
Pre-mix	5%	Dog bone	380×150×50	No	90°C steam curing, 48hrs	3	Inductive test, direct tensile test
Pre-mix	5%	Beam	100×100×400	No	90°C steam curing, 48hrs	4	Inductive test, bending test

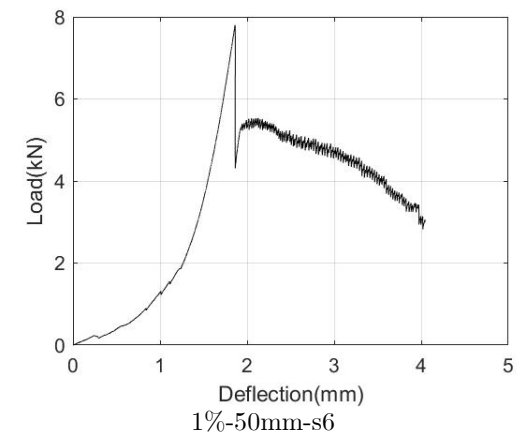
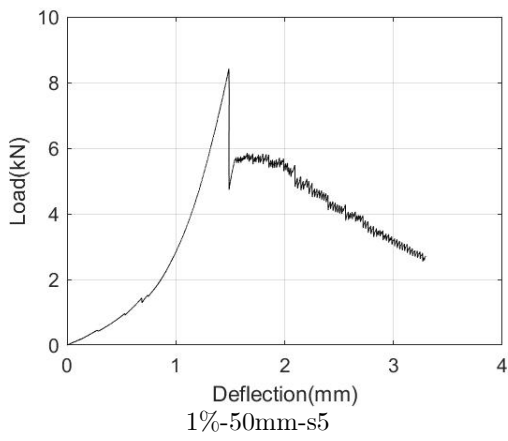
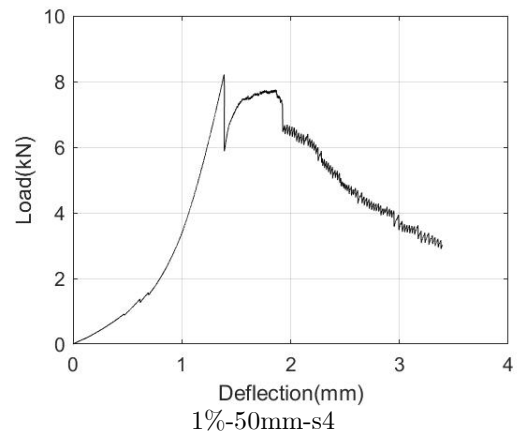
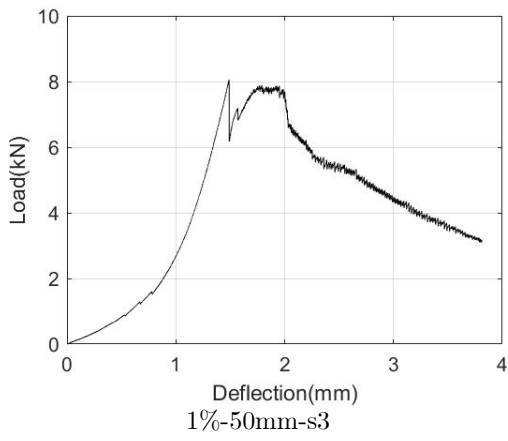
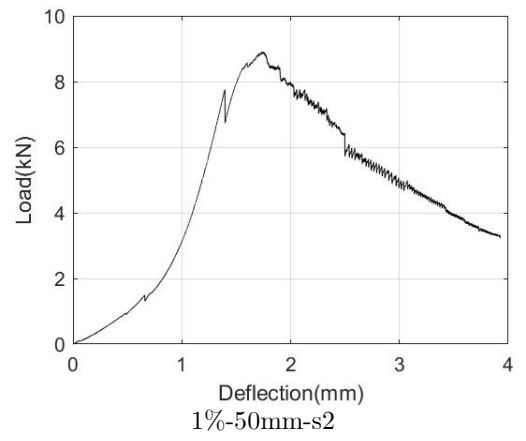
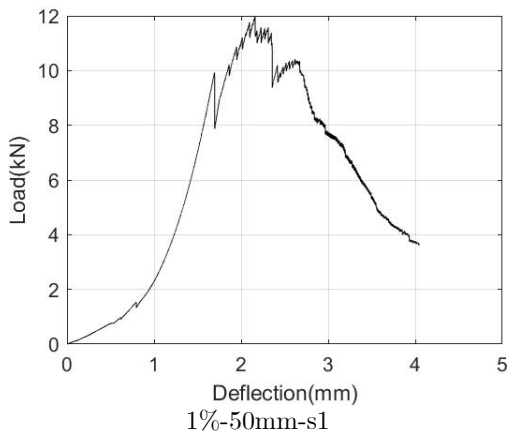
Appendix 2 Load-deflection curve for 50×200×H beams

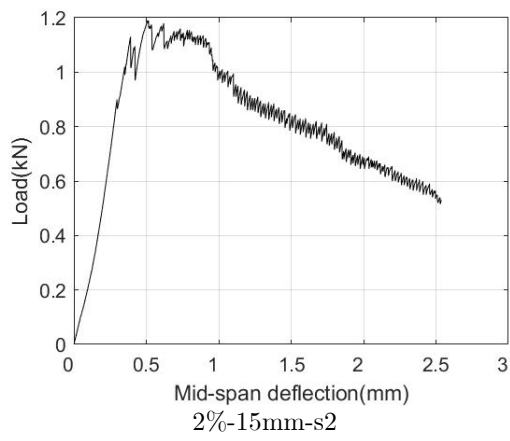
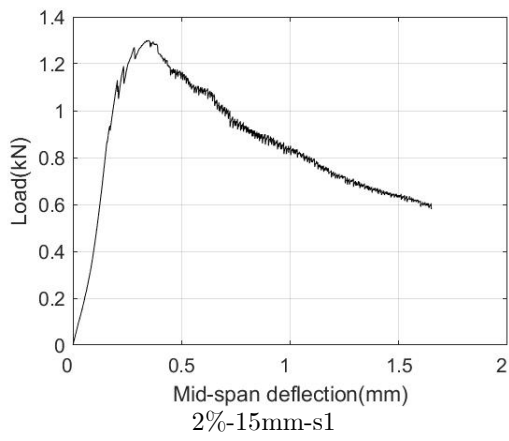
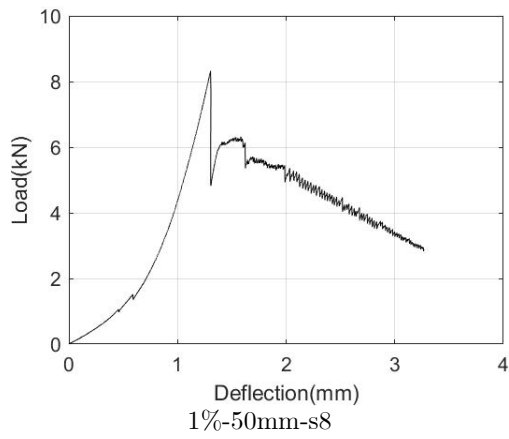
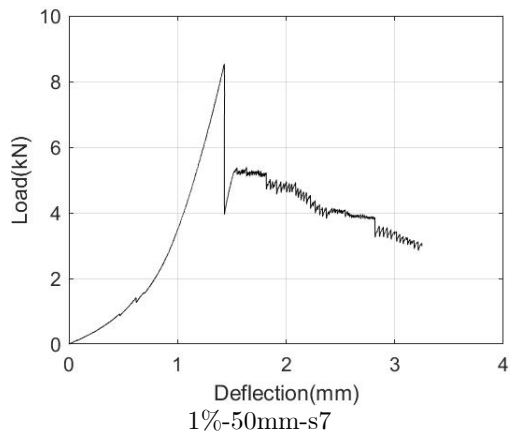




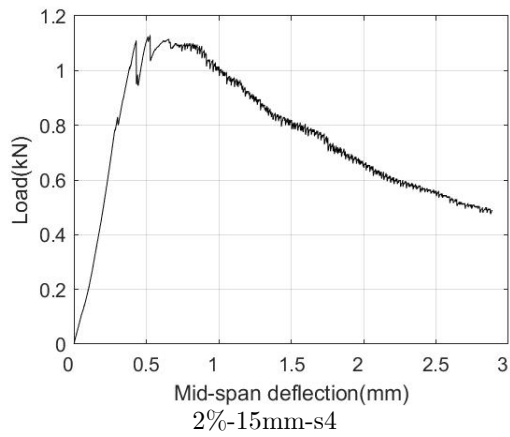


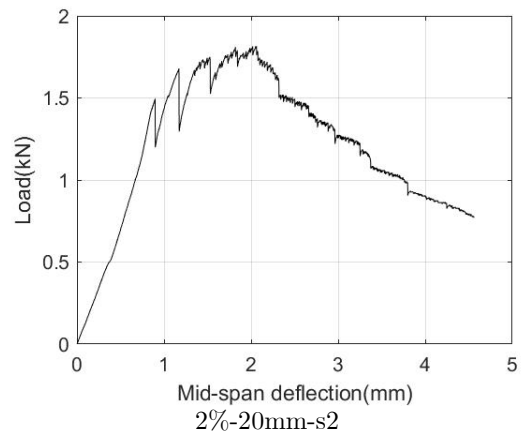
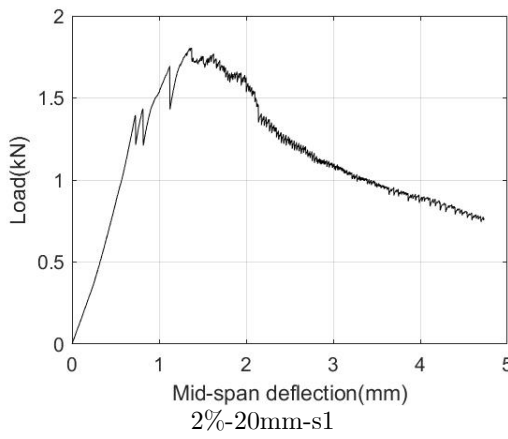
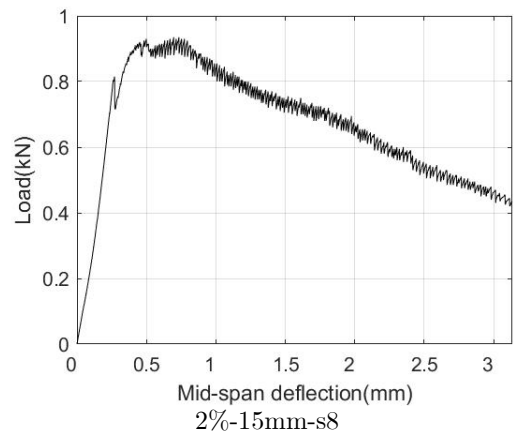
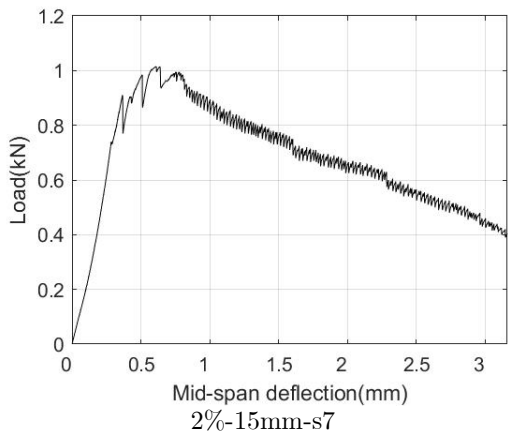
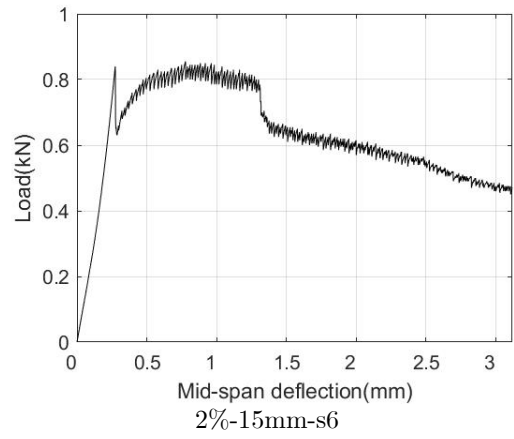
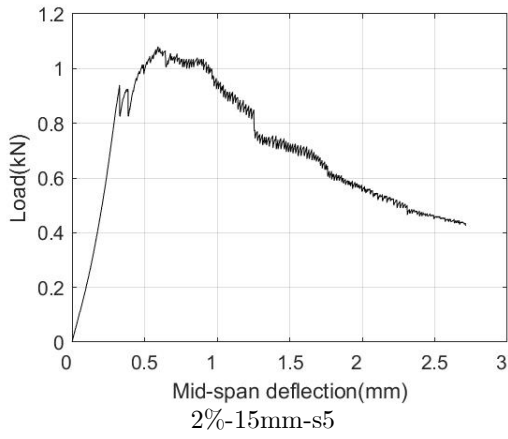


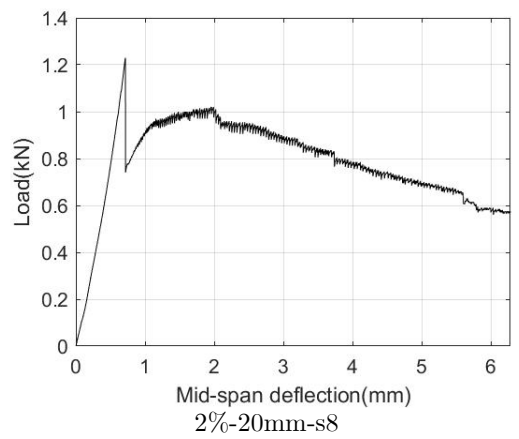
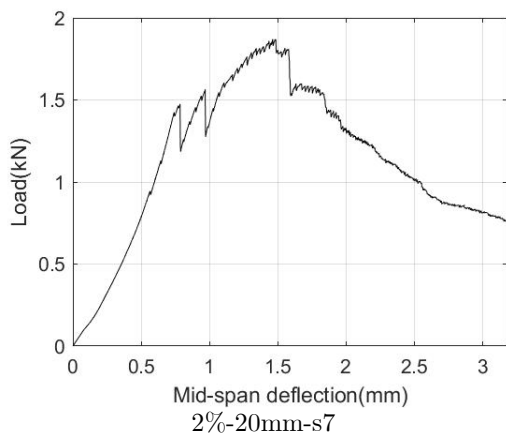
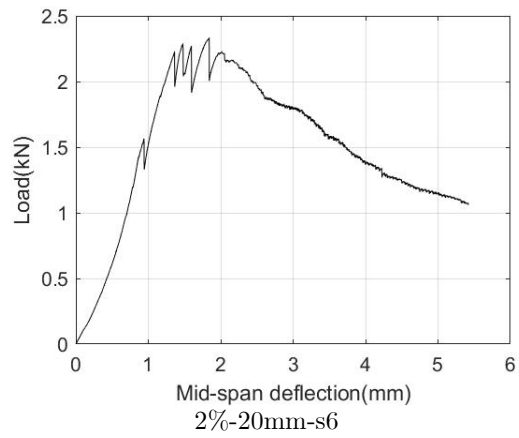
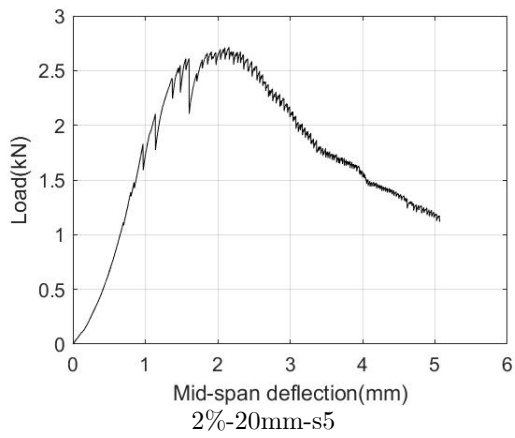
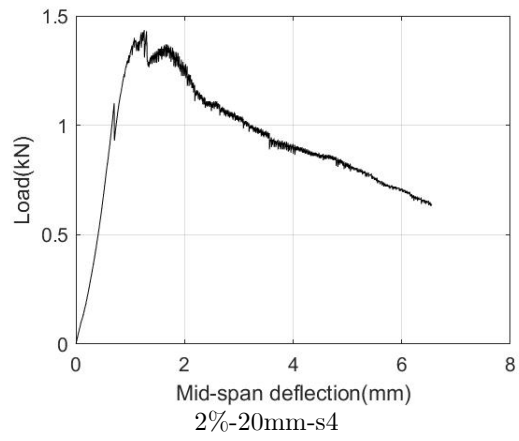
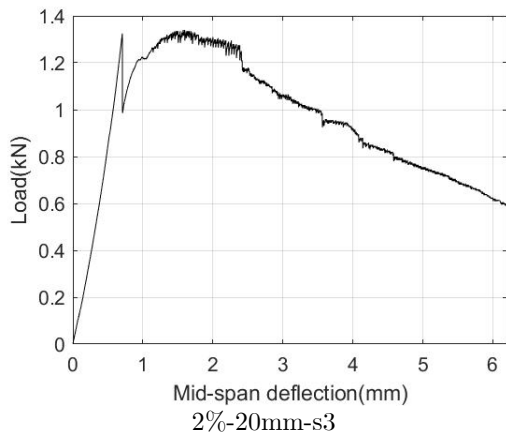


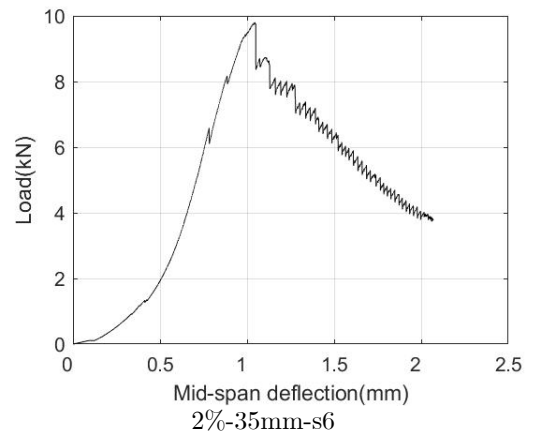
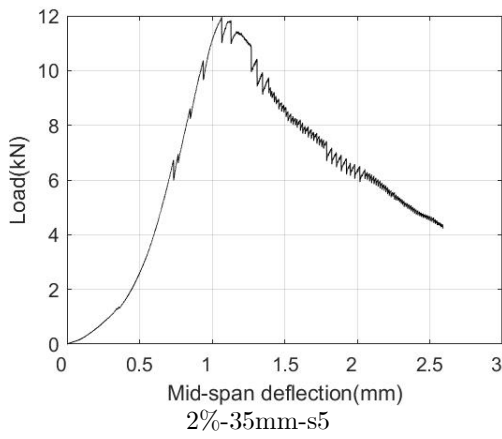
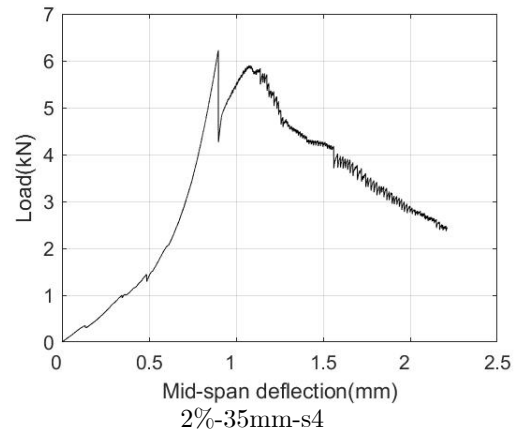
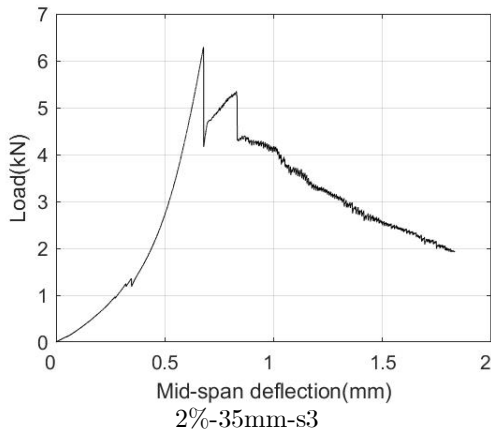
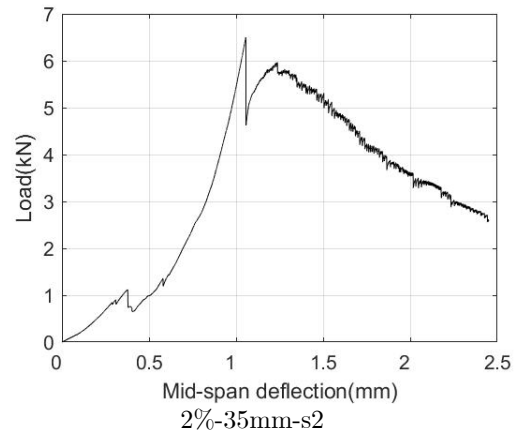
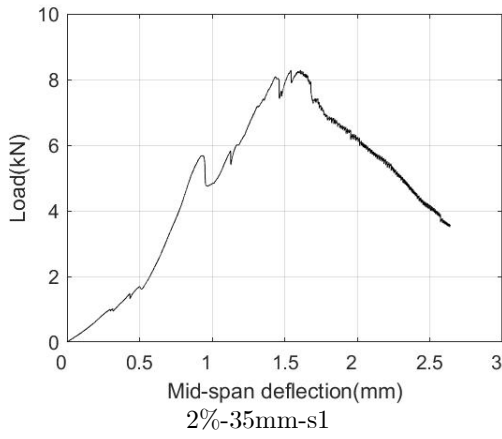


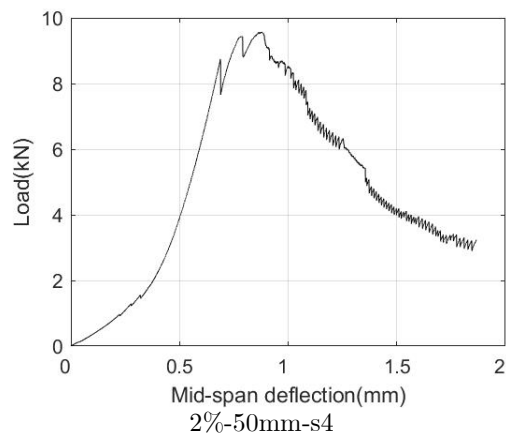
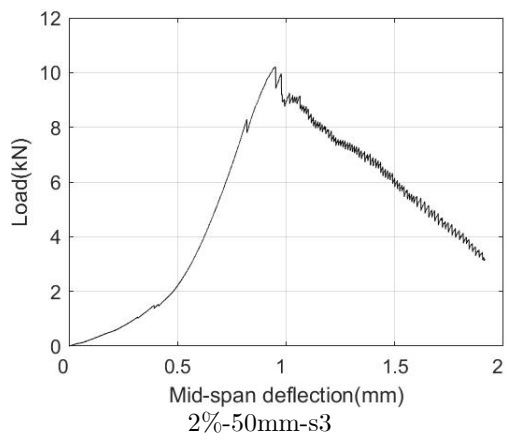
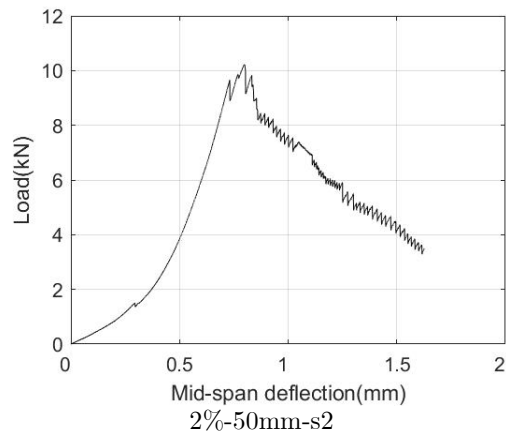
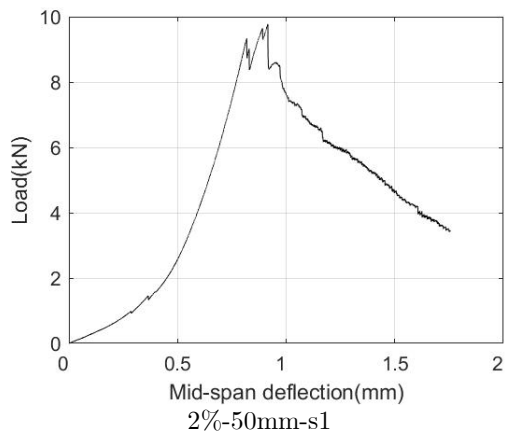
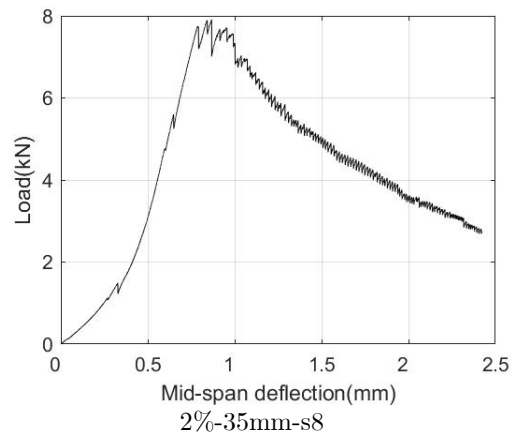
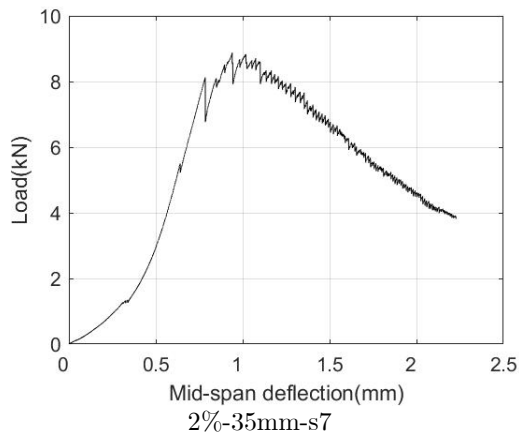
2%-15mm-s3

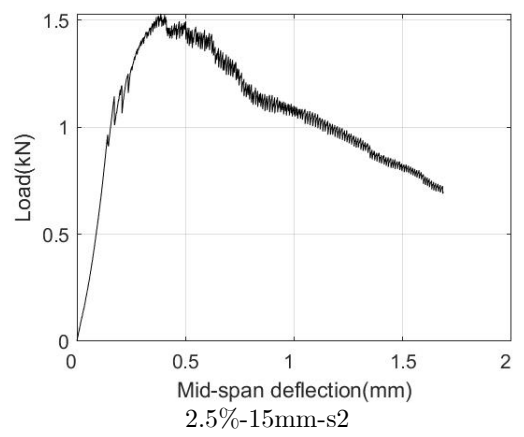
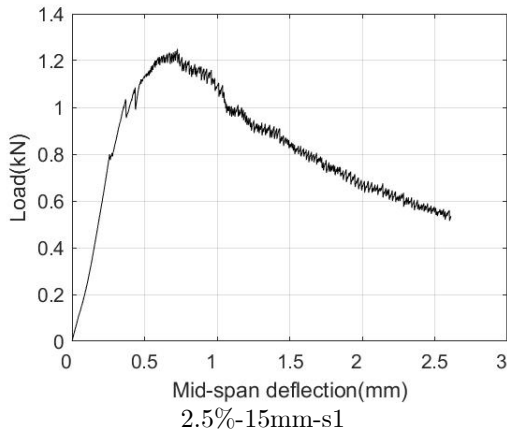
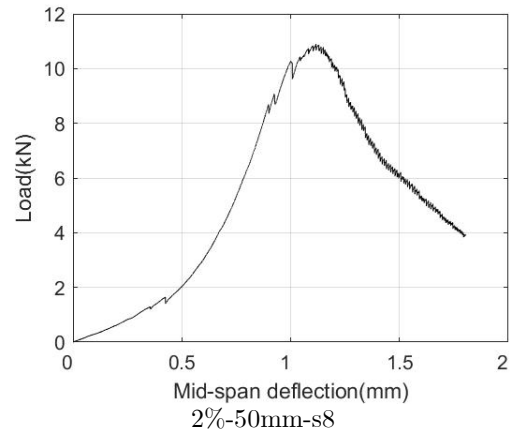
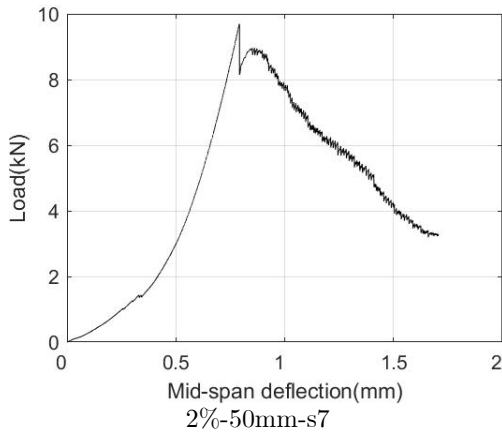
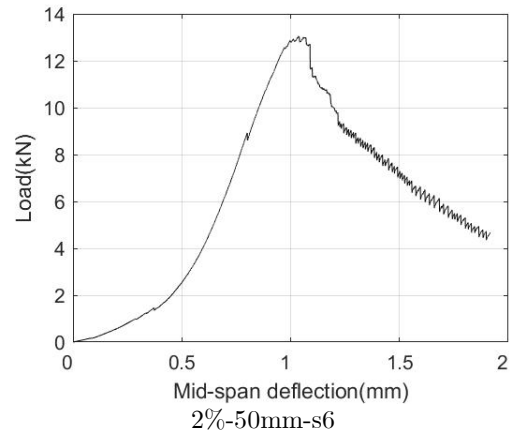
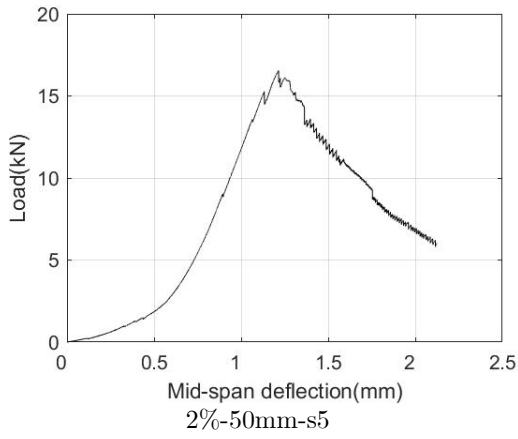


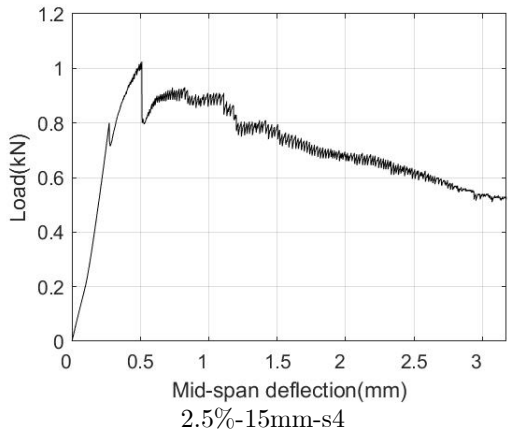












2.5%-15mm-s3

